

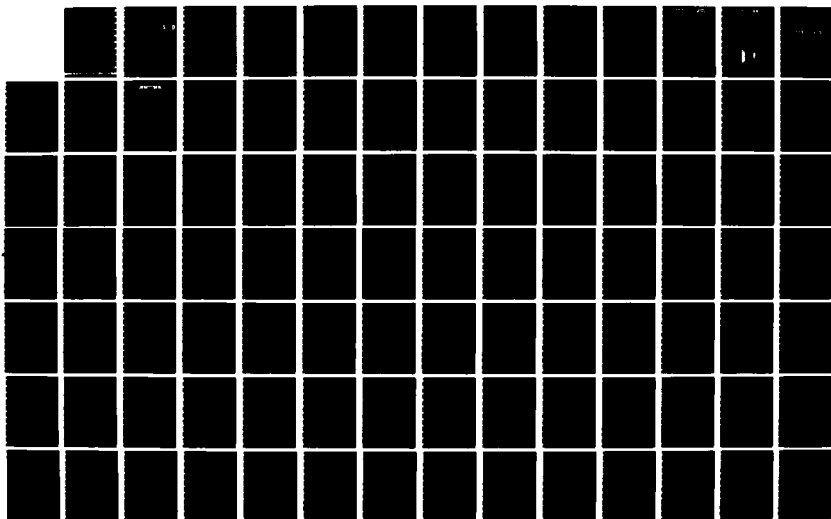
AD-A174 621

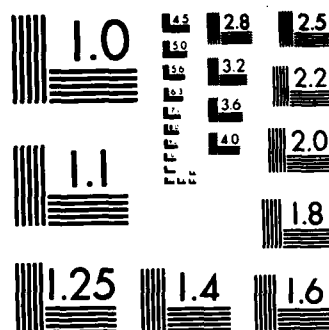
DESIGN AND FABRICATION OF SUBMICRON MAGNETIC BUBBLE  
DEVICE TECHNOLOGY (U) CARNEGIE-MELLON UNIV PITTSBURGH  
PA DEPT OF ELECTRICAL AND COM M H KRYDER ET AL  
31 OCT 86 AFOSR-TR-86-1075 AFOSR-84-0341 F/G 14/3

1/2

UNCLASSIFIED

NL





MICROCOPY RESOLUTION TEST CHART  
NATIONAL BUREAU OF STANDARDS-1963-A

AD-A174 621

AFOSR-TR. 86-1075

NE-Witt  
AFOSR-84-0341  
(2)

## Design and Fabrication of Submicron Magnetic Bubble Device Technology

M. H. Kryder, M. Alex, C. L. Bauer, R. O. Campbell,  
D. W. Greve, A. M. Guzman, S.-C. Jo, P.H.L. Rasky and M. Ramesh,  
J-F. Silvain and J. Wullert

Magnetics Technology Center  
Carnegie Mellon University

### 2<sup>nd</sup> Annual Scientific Report Executive Summary

DTIC  
ELECTE  
NOV 26 1986  
S D

During the period September 30, 1984 to September 29, 1986 work was carried out at Carnegie Mellon University under AFOSR grant number 84-0341 on the design and fabrication of submicron magnetic bubble device technology. Two results from the research have been classified as major accomplishments. Our successful fabrication of silicon MOSFETS on magnetic bubble garnet substrates was selected by Science Digest (December, 1985) to be one of the "Top 100 Innovations" in 1985 and has the potential of leading to much faster access time data storage devices. Our development of magnetic garnet materials with isotropic magnetostriction has furthermore resulted in dramatic improvements in the operating margins of ion implanted contiguous disk bubble devices utilizing  $0.5\mu\text{m}$  diameter bubbles. These new materials make possible chip capacities as large as 64 megabits.

In addition to the above two major accomplishments, we also made significant progress in a number of other areas.

In studies of the effects of ion implantation on garnet we used electron microscopy to study how high dose implantation leads to damage in the single crystal garnet and how photolithography and ion implantation conditions affect the strain contours at pattern edges in ion implanted bubble devices. From this work we now understand the limitations which the ion implantation process places on the bit density of ion implanted bubble devices, and have been able to develop processes which make it possible to make devices utilizing  $0.5\mu\text{m}$  diameter bubble domains.

In studies of ion implanted device design, we obtained overlapping bias field margins of about 9% for all functions on a chip with 50 Oe drive field applied. Minor improvements to the gate design used for transferring data into the minor loops would improve this to more than 10%. These margins are comparable to those of much lower density devices in production today.

**DISTRIBUTION STATEMENT A**

Approved for public release  
Distribution Unlimited

86 11 26 051

DTIC FILE COPY

Unclassified

SECURITY CLASSIFICATION OF THIS PAGE

## REPORT DOCUMENTATION PAGE

1a. REPORT SECURITY CLASSIFICATION Unclassified		1b. RESTRICTIVE MARKINGS													
2a. SECURITY CLASSIFICATION AUTHORITY		3. DISTRIBUTION/AVAILABILITY OF REPORT  Unlimited													
2b. DECLASSIFICATION/DOWNGRADING SCHEDULE															
4. PERFORMING ORGANIZATION REPORT NUMBER(S)  1		5. MONITORING ORGANIZATION REPORT NUMBER(S)  AFOSR-TR. 86-1075													
6a. NAME OF PERFORMING ORGANIZATION Electrical & Computer Engrg. Carnegie Mellon University	6b. OFFICE SYMBOL (If applicable)	7a. NAME OF MONITORING ORGANIZATION  Air Force Office of Scientific Research													
6c. ADDRESS (City, State and ZIP Code)  Pittsburgh, PA 15213		7b. ADDRESS (City, State and ZIP Code)  Bolling Air Force Base Washington, DC 20332													
8a. NAME OF FUNDING/SPONSORING ORGANIZATION AFOSR/NE	8b. OFFICE SYMBOL (If applicable) NE	9. PROCUREMENT INSTRUMENT IDENTIFICATION NUMBER  AFOSR-84-0341													
8c. ADDRESS (City, State and ZIP Code)  Bolling Air Force Base Washington, D.C. 20332		10. SOURCE OF FUNDING NOS. <table border="1"><thead><tr><th>PROGRAM ELEMENT NO.</th><th>PROJECT NO.</th><th>TASK NO.</th><th>WORK UNIT NO.</th></tr></thead><tbody><tr><td>2305-C1 61103F</td><td>2305</td><td>C1</td><td></td></tr></tbody></table>		PROGRAM ELEMENT NO.	PROJECT NO.	TASK NO.	WORK UNIT NO.	2305-C1 61103F	2305	C1					
PROGRAM ELEMENT NO.	PROJECT NO.	TASK NO.	WORK UNIT NO.												
2305-C1 61103F	2305	C1													
11. TITLE (Include Security Classification) (Unclassified) Design & Fabrication for Submicron Magnetic Bubble Device Technology		12. PERSONAL AUTHOR(S) M.H. Kryder, M. Alex, C.L. Bauer, R.O. Campbell, D.W. Greve, A. Guzman, S. Jo, P.H.L. Rasky, M. Ramesh, J.F. Silvain, J. Wullert													
13. ANNUAL Scientific 9/30/85 to 9/29/86		14. DATE OF REPORT (Yr., Mo., Day) Oct. 31, 1986													
15. SUPPLEMENTARY NOTATION		15. PAGE COUNT 66													
17. COSATI CODES <table border="1"><thead><tr><th>FIELD</th><th>GROUP</th><th>SUB. GR.</th></tr></thead><tbody><tr><td></td><td></td><td></td></tr><tr><td></td><td></td><td></td></tr><tr><td></td><td></td><td></td></tr></tbody></table>		FIELD	GROUP	SUB. GR.										18. SUBJECT TERMS (Continue on reverse if necessary and identify by block number) Bubble Memory, Ion Implantation, Garnet, Silicon-on-Insulator, Silicon-on-Garnet	
FIELD	GROUP	SUB. GR.													
19. ABSTRACT (Continue on reverse if necessary and identify by block number) <p>Work was carried out on high density (16 to 64 Mbit/cm<sup>2</sup>) magnetic bubble device technology. Highlights of the research include the successful fabrication of silicon MOSFETS on bubble garnet substrates and the development of ion implanted bubble devices utilizing 0.5μm bubbles in garnets with isotropic magnetostriction. In addition, studies of the effects of ion implantation on garnet lead to improved fabrication techniques for the 0.5μm devices. Chips utilizing 1μm bubbles were demonstrated to have about 9% bias field margins at 50 Oe drive, and a numerical model was developed to model current accessed ion implanted devices.</p>															
20. DISTRIBUTION/AVAILABILITY OF ABSTRACT  UNCLASSIFIED/UNLIMITED <input checked="" type="checkbox"/> SAME AS RPT. <input type="checkbox"/> DTIC USERS <input type="checkbox"/>		21. ABSTRACT SECURITY CLASSIFICATION  Unclassified													
22a. NAME OF RESPONSIBLE INDIVIDUAL  Dr. Gerald Witt		22b. TELEPHONE NUMBER (Include Area Code) 202-767-4931	22c. OFFICE SYMBOL  NE												

In studies of current-access ion implanted technology we developed numerical modeling tools which can be used for the development of new higher data rate current-accessed devices. Comparisons of the model with experimental data indicate a good fit. If these devices are successful, the data rate of bubble devices could be increased by an order of magnitude.

Detailed descriptions of the above research are contained in the attached reports, many of which have appeared as journal publications.



Accession For	
NTIS CRA&I	<input checked="" type="checkbox"/>
DTIC TAB	<input type="checkbox"/>
Unannounced	<input type="checkbox"/>
Justification	
By	
Distribution /	
Availability Codes	
Dist	Avail and/or Special
A-1	

# Integrated Silicon on Garnet Device Structures

P.H.L. Rasky, D.W. Greve, and M.H. Kryder

Department of Electrical and Computer Engineering, Carnegie Mellon

## ABSTRACT

Silicon MOSFETs have been fabricated on magnetic bubble substrates. These devices are separated from the bubble film by one or more spacer layers. If a single  $\text{SiO}_2$  spacer is used, high gate leakage occurs;  $I_G$  is usually greater than  $1\mu\text{A}$  at  $V_{GS}=1\text{V}$  for  $V_{DS}=0\text{V}$ . When a double spacer of  $\text{SiO}_2$  and  $\text{Si}_3\text{N}_4$  is used, the gate leakage current is low; typically,  $I_G < 100\text{pA}$  at  $V_{GS}=4\text{V}$  for  $V_{DS}=0\text{V}$ . We have found that the present silicon on garnet fabrication process does alter the room temperature magnetic properties of the bubble substrate. The saturation magnetization drops by 20% for  $1\mu\text{m}$  material, and by 14% for  $0.5\mu\text{m}$  material. However, it may be possible to reverse these changes by a suitable post-process anneal. Oxygen anneals near the growth temperature of the bubble film have been effective thus far. Silicon magnetodiodes have been fabricated on silicon substrates with sensitivities of  $2.1 \times 10^{-4} \mu\text{A}/\text{Gauss}$  per  $\mu\text{m}$  of diode width at  $V_{\text{diode}}=30.0\text{V}$ . This represents the first step toward our goal of fabricating integrated silicon on garnet magnetic field sensors.

## INTRODUCTION

Magnetic bubble memories/systems are of current interest for a number of reasons. They are inherently non-volatile and radiation hard, two particularly important features when equipment, such as satellites, must operate for long periods of time in harsh electromagnetic environments. Unfortunately, large bubble systems have long data access times - it takes tens of milliseconds for querying subsystems to get the information they seek. Shorter access times are clearly desirable, and our research indicates that it may be possible to significantly reduce the access time by utilizing integrated bubble/semiconductor devices.

Conceptually our solution is simple: use many small (high sensitivity) magnetic bubble sensors instead of one very large (low sensitivity) detector and multiplex the output data before it's taken off chip. The multiplexing can be done with MOSFETs, and the detection can be done with high sensitivity silicon magnetodiodes. The number of sensors used could be 1000 or larger.

Figures 1 and 2 show a magnetodiode sensor integrated with an ion-implanted propagation pattern. In this design, magnetic bubbles move along the propagation pattern in response to a rotating in-plane magnetic field until they reach the hairpin stretcher. The hairpin stretcher is then activated by applying a large current pulse (100-200mA), causing the effective bias field in the ion-implanted channel to be lowered. The bubble therefore expands into the channel, and part of its flux is intercepted by the silicon magnetodiode. This flux will deflect electrons and holes to one of the interfaces. Which interface they are deflected to will depend on the field's orientation ( $\mathbf{F} = q\mathbf{V} \times \mathbf{B}$ ). When these current carriers arrive at an interface, they will recombine at a rate dependent on the surface recombination velocity ( $S$ ) of the interface. In general, each interface has a different  $S$  and one therefore expects the density of free electrons and holes in the base region ( $n$ -Si) to change. A change in electron - hole density implies a change in conductivity and consequently a change in diode current for a fixed voltage across the diode. Figure 3 illustrates how this effect can be utilized in practice. For the  $B > 0$  case, some electrons (and holes) that would recombine at the high  $S$  interface (the bottom interface) are deflected toward the low  $S$  interface (the top interface), and the diode current increases since more electrons and holes are available to participate in the conduction process.

#### DEVICE CHARACTERISTICS: MAGNETODIODES

Silicon magnetodiodes have been fabricated on silicon substrates, and the structure of these diodes is shown in Fig. 4(A). The current - voltage characteristics of our devices were similar to those of other researchers [1]. Figure 4(B) shows the diode current (for a fixed voltage of +30 volts) when the in-plane  $B$  field is swept between + and - 16kG. From this data, it follows that the diode has a sensitivity of  $2.1\text{E-}4 \mu\text{A/Gauss}$  per  $\mu\text{m}$  of diode width. Furthermore, the qualitative behavior of the diode current agrees with that expected from the simple theory introduced in the preceding section. When  $+B$  is applied (see Fig. 4(C)), the Lorentz force deflects electrons and holes to the top interface and the diode current increases. When  $-B$  is applied,  $q\mathbf{V} \times \mathbf{B}$  deflects electrons and holes to the bottom interface and the diode current decreases.

#### DEVICE CHARACTERISTICS: MOSFETS

In this section, we report on the device characteristics of silicon on garnet MOSFETs. We will show that devices fabricated on garnet wafers with  $\text{SiO}_2 + \text{Si}_3\text{N}_4$  spacer layers are of higher quality than those fabricated on substrates coated with only  $\text{SiO}_2$ .

Figure 5 shows the final cross section for a silicon on garnet FET. In this case, the single  $\text{SiO}_2$  spacer was deposited by RF sputtering and is  $1\mu\text{m}$  thick. On top of the oxide spacer, a  $0.5 - 0.75\mu\text{m}$  LPCVD polysilicon film was deposited at  $625^\circ\text{C}$  and  $0.4$  torr. The poly Si was capped with  $1\mu\text{m}$  of sputtered silicon dioxide, recrystallized with an Argon laser, and patterned into  $25 \times 100\mu\text{m}$  islands. The islands were doped via ion-implantation and a  $0.1\mu\text{m}$  gate oxide was grown in wet oxygen at  $850^\circ\text{C}$ . After opening contact windows, aluminum was deposited and patterned to form the source, drain, and gate electrodes.

Current - voltage characteristics for MOSFETs fabricated on  $\text{SiO}_2$  coated bubble substrates fall into two basic categories: (1), devices with gate current less than the drain current (Fig. 6(A)), and (2), devices with gate current greater than the drain current (Fig. 7(A)). The corresponding low and high gate leakage models are given in Fig. 6(B) and 7(B). In the later case, the gate leakage current is so high that formation of an inversion layer is not possible. This is not the case for the first model, and one may verify the correctness of these models by using simple circuit analysis. From the model of Fig. 6(B), we find  $I_D < 0$  for  $V_{DS} < [R_S/(R_S + R_{OX})]V_{GS}$  and  $I_D > 0$  for  $V_{DS} > [R_S/(R_S + R_{OX})]V_{GS}$ . By inspection, we find  $I_D = 0$  when  $V_{GS} = V_{DS}$  for the model of Fig. 7(B). These non-ideal characteristics can be attributed to contamination of the silicon island and gate oxide [2].

Next, MOSFETs with the structure shown in Fig. 8 were fabricated. In this case, both the  $\text{SiO}_2$  and  $\text{Si}_3\text{N}_4$  spacers were deposited by LPCVD. The oxide was deposited at  $860^\circ\text{C}$  by reacting  $\text{SiH}_4$  and  $\text{N}_2\text{O}$ . The  $\text{Si}_3\text{N}_4$  was deposited at  $800^\circ\text{C}$  by reacting  $\text{SiH}_4$  and  $\text{NH}_3$ . LPCVD was selected since this technique is known to produce high quality layers.

Figure 9 shows a I-V characteristic for a device with the structure shown in Fig. 8 - note the absence of negative drain current for small positive  $V_{DS}$  for all  $V_{GS}$  (cf. with Fig. 6(A)). The improvement over the single oxide spacer case can be made even more clear by comparing the  $I_G$  vs.  $V_{GS}$  plots for devices fabricated on  $\text{SiO}_2$  and  $\text{SiO}_2 + \text{Si}_3\text{N}_4$  spacers - see Fig. 10 and 11. At  $V_{GS} = 3.0\text{ V}$ , the device fabricated on the double spacer layer ( $\text{SiO}_2 + \text{Si}_3\text{N}_4$ ) has a gate leakage current six orders of magnitude lower than the device fabricated on the single  $\text{SiO}_2$  spacer layer. The breakdown



characteristic for the double spacer layer device is also substantially sharper than for the single spacer layer device. We have also found that a thinner ( $0.24\ \mu\text{m}$ )  $\text{Si}_3\text{N}_4$  spacer is just as effective in reducing contamination, and hence gate leakage, as is the thick ( $0.85\ \mu\text{m}$ ) nitride spacer.

### STABILITY OF MAGNETIC BUBBLE FILMS: ANNEALING

The data presented thus far indicates that fabrication of silicon on garnet devices is possible, but the issue of what the requisite high temperature processing does to the magnetic properties of the bubble film still must be addressed. Table 1 lists measured values for the saturation magnetization  $4\pi M_s$  and zero field strip width  $W_0$  after each of the processing steps (with the exception of the gate oxidation step) used to fabricate the structure shown in Fig. 8 for 1 and  $0.5\ \mu\text{m}$  bubble material. The properties for both types of material do change, but these changes are not catastrophic. Also note that the changes in  $4\pi M_s$  and  $W_0$  are less, on a percentage basis, for the  $0.5\ \mu\text{m}$  diameter bubble material. This is a clear advantage as one scales to smaller diameter bubble materials. If one selects the bubble material and subsequent processing conditions carefully, the post-processing values of  $4\pi M_s$  and  $W_0$  can be identical with the as grown values. Data presented in [2] verify that this is the case for a simple silicon on garnet process, and at this point we will reproduce some of that data. Figure 12(A) shows the relevant structure;  $4\pi M_s$  for the as grown bubble film is 695 G. After this structure is laser annealed (after the silicon is recrystallized),  $4\pi M_s$  is found to be  $\sim 774$  G. If the material is next post-laser annealed, in oxygen at  $850^\circ\text{C}$ , it is found that the room temperature  $4\pi M_s$ , after the anneal, will be close to the as grown value (see Fig. 12(B)). Consult [2] and [3] for additional data on the annealing of magnetic bubble films.

### SUMMARY

To date, we have demonstrated that it is possible to fabricate semiconductor devices on magnetic bubble substrates. Some problems still exist, but they appear solvable and research on system issues is now merited. Annealing studies indicate the common bubble film compositions are reasonably tolerant of the high temperature processing required to fabricate silicon on garnet devices. The demonstration of silicon magnetodiodes on silicon substrates is particularly important since one can now consider combining bubble detection devices with post-processing electronics on a single substrate.

## FUTURE WORK

The next major goal of our research is to fabricate the structure (or those similar to it) shown in Fig. 1 on magnetic bubble substrates, and to use this type of sensor to detect magnetic bubbles. Additional annealing studies, directed at demonstrating and understanding bubble propagation in magnetic films subjected to the silicon on garnet process, will be conducted. Indeed, this future work is very important and necessary if we are to realize a magnetodiode that senses the fringing magnetic field of a magnetic bubble.

## REFERENCES

- [1] A. Mohaghegh, S. Cristoloveanu, and J. De Pontcharra, IEEE Transactions on Electron Devices, ED-28, NO. 3, March 1981.
- [2] P.H.L. Rasky, MS. project report, Carnegie-Mellon University, 1984 (unpublished).
- [3] P.H.L Rasky, D.W. Greve, M.H. Kryder and S. Dutta, J. Appl. Phys. 57, 4077, (1985).

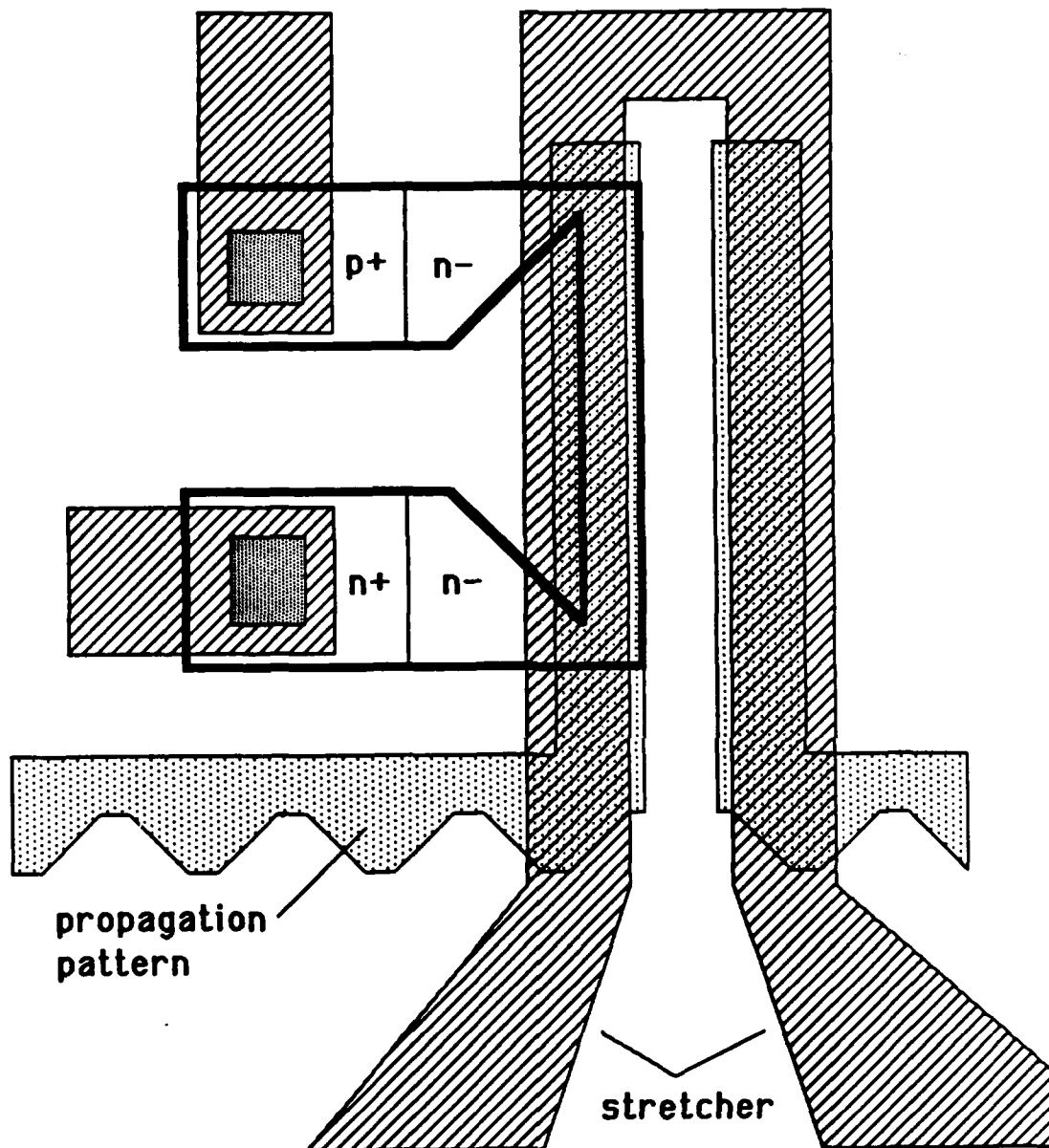


Figure 1: Silicon magnetodiode integrated with an ion-implanted bubble propagation pattern.

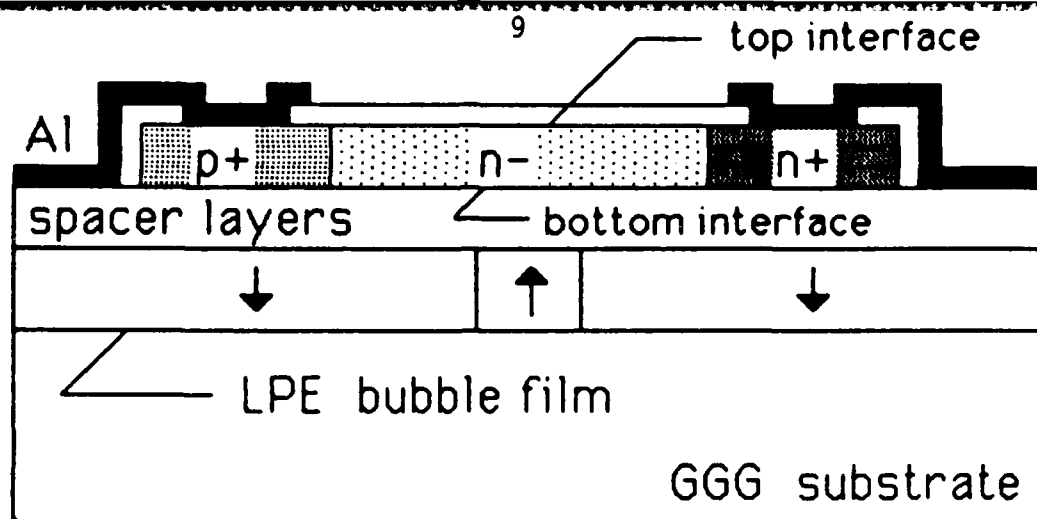
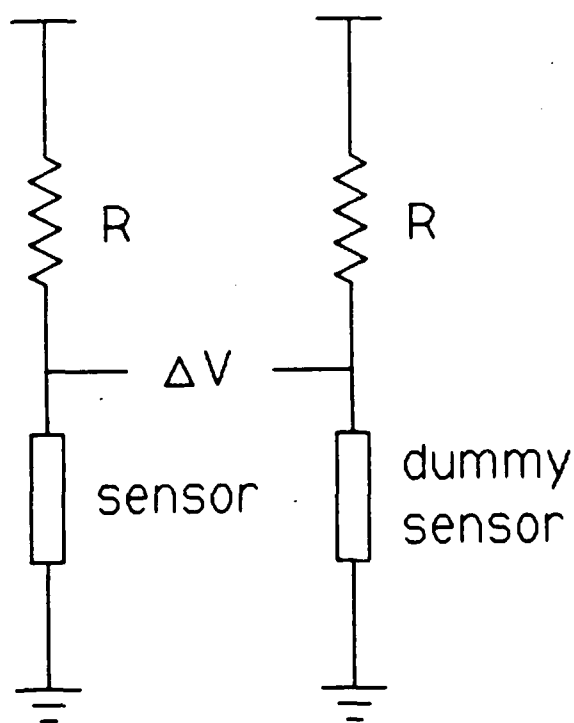
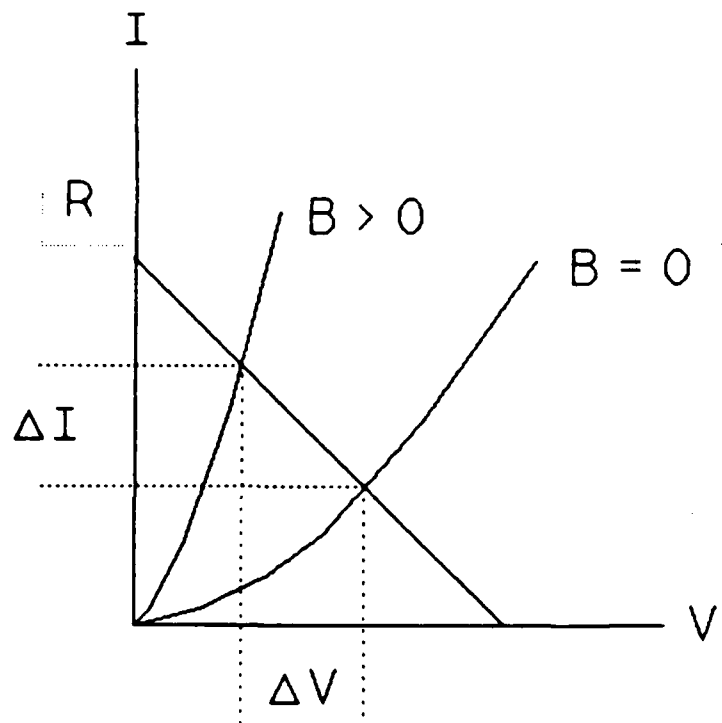


Figure 2: Cross section of a silicon on garnet magnetodiode.

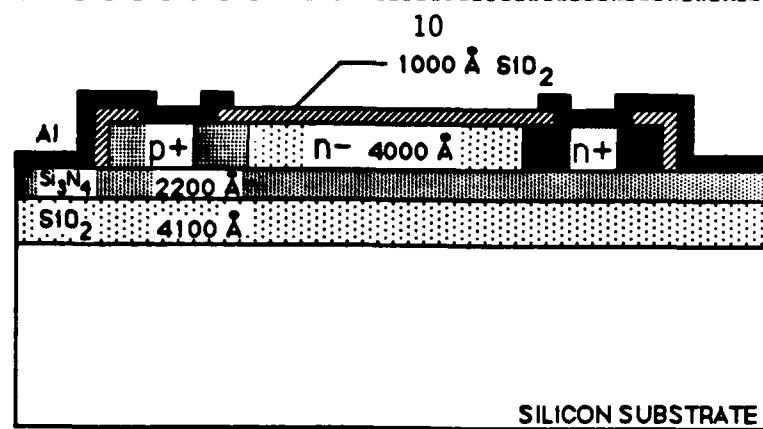


(A)

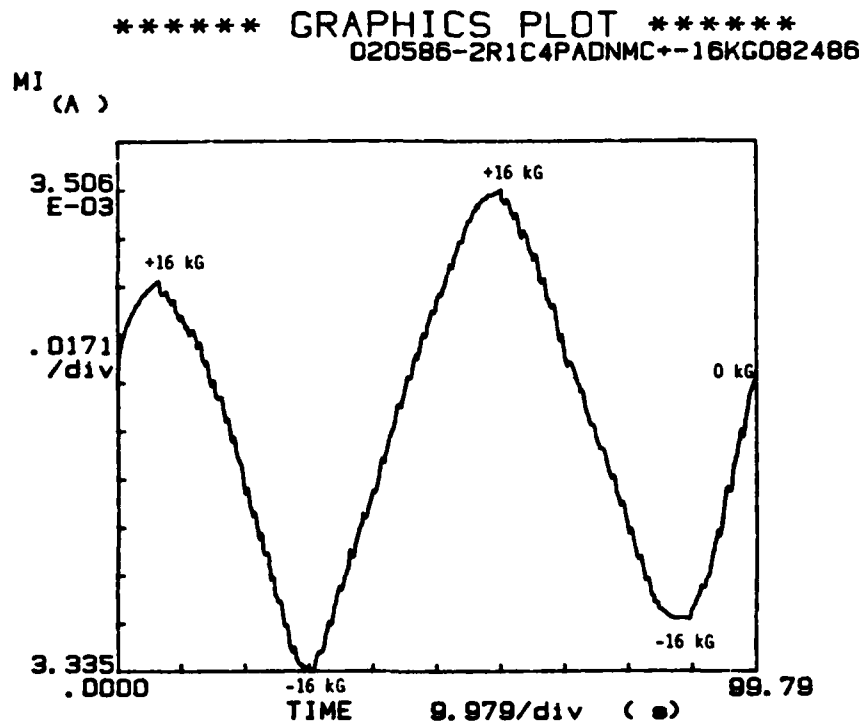


(B)

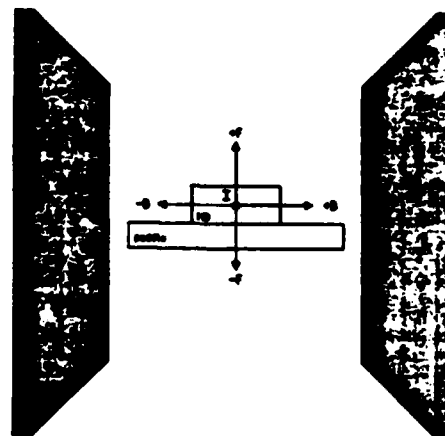
Figure 3: (A) Magnetodiode differential detection circuit.  $\Delta V = 0$  when no bubble is present (logic 0) and  $\Delta V < 0$  or  $\Delta V > 0$  when a bubble is present (logic 1). The sensor and dummy sensor have identical structures. Only the sensor diode is near enough to the bubble to be affected by its in-plane magnetic field. (B) load line analysis for one half of the circuit shown in (A).



(A)



(B)



(C)

Figure 4:

(A) Cross section of a silicon magnetodiode with a silicon substrate. The diode is 25  $\mu$ m wide.

(B) Diode forward current  $I_D$  with an applied in-plane magnetic field; the field was swept between + and - 16kG.

(C) Orientation of magnetodiode during measurements.

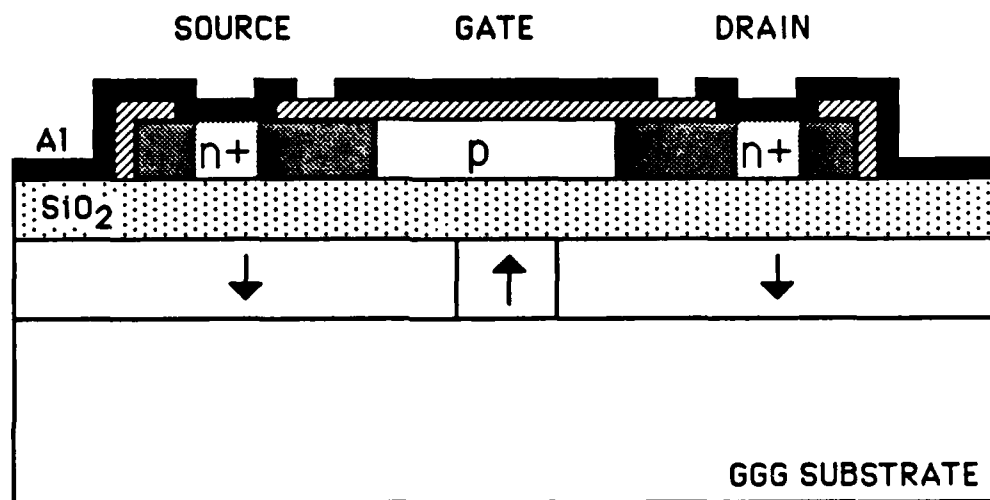
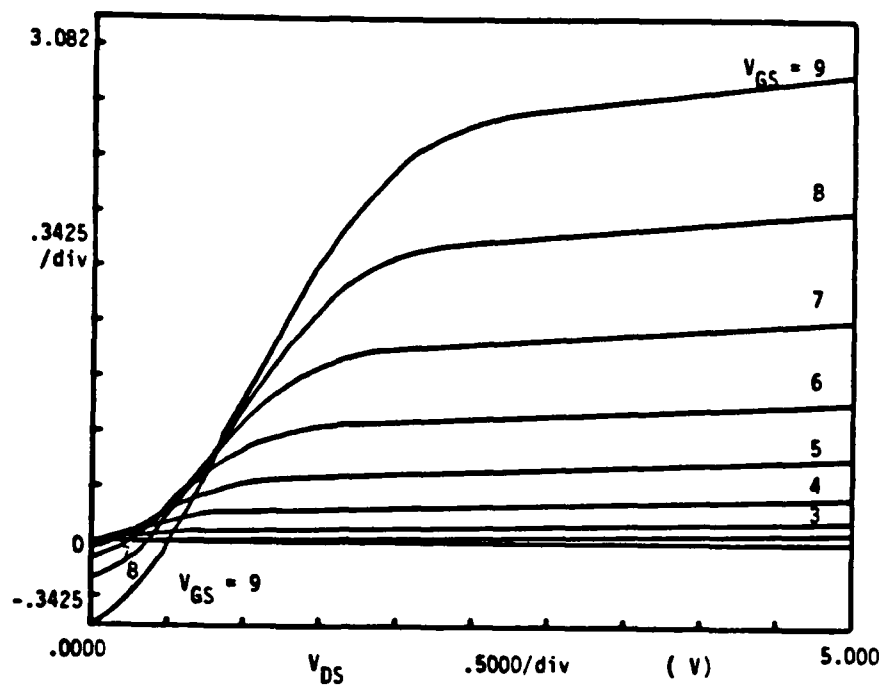
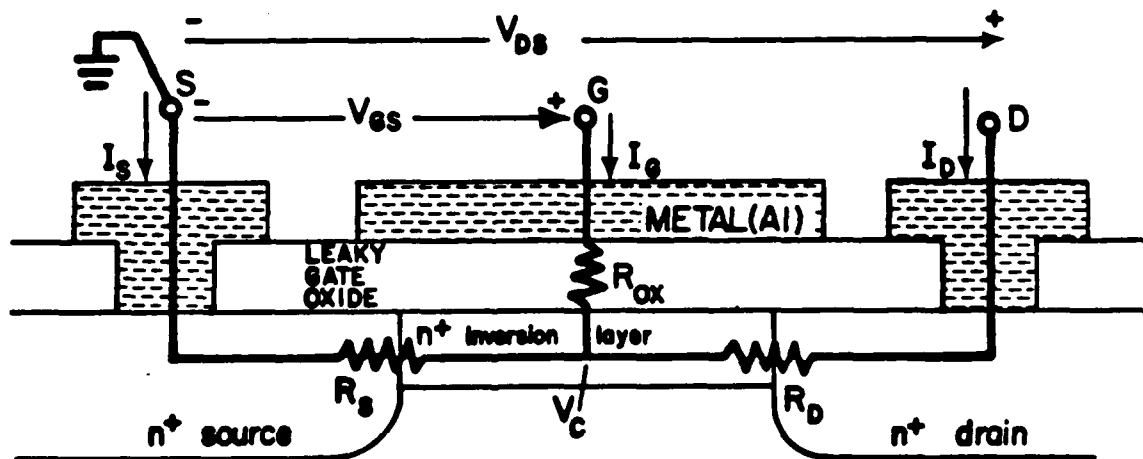


Figure 5:

Cross section of a silicon on garnet MOSFET with a sputtered oxide spacer.



(A)

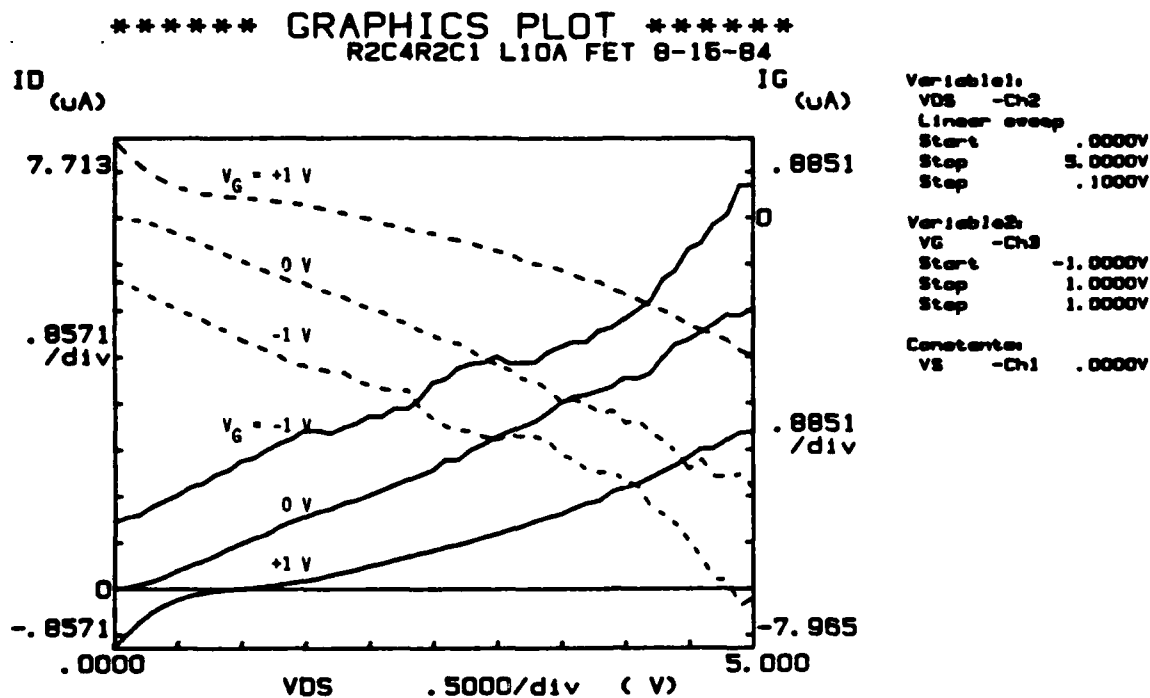


(B)

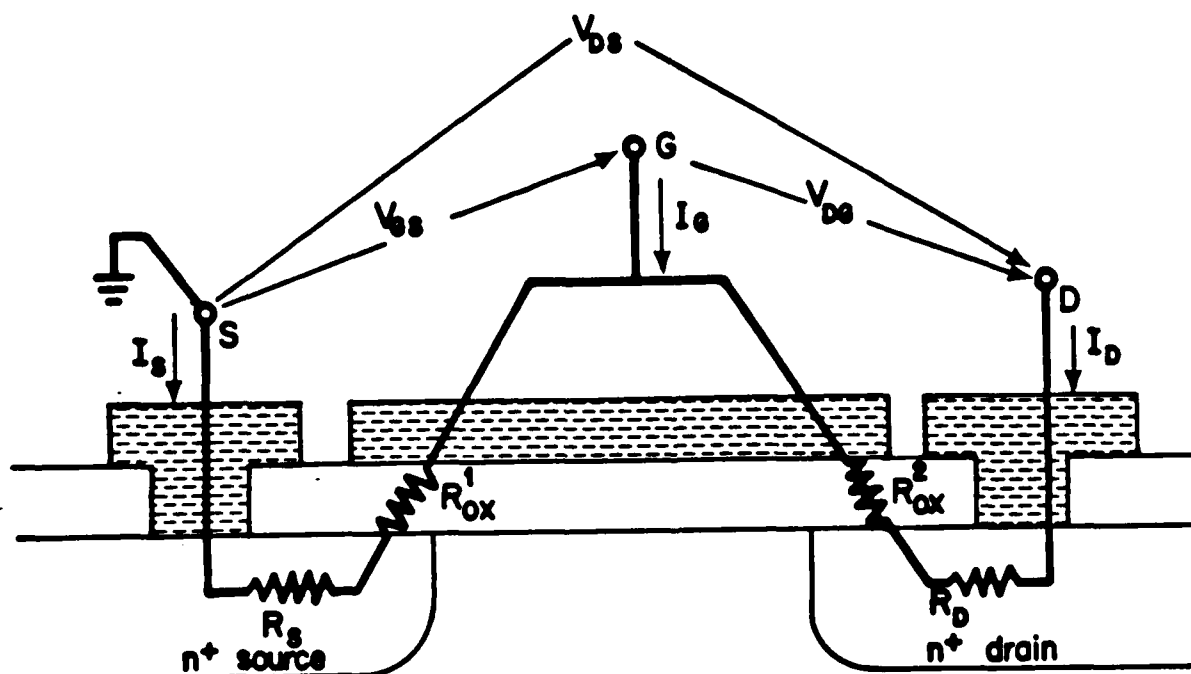
Figure 6:

(A) Drain characteristics for a silicon on garnet MOSFET adequately modeled by the the circuit shown in part (B) of this figure. The composition of the bubble film is  $(Y_{1.00}Sm_{0.39}Tm_{0.92}Ca_{0.69})\{Ge_{0.70}Fe_{4.30}\}O_{12}$ . The channel length/width ratio of the MOSFET is  $25\mu m/25\mu m$ .

(B) Device model for a MOSFET with non-zero, non-catastrophic gate leakage current.



(A)



(B)

Figure 7:

(A) Drain characteristics for a MOSFET adequately modeled by the circuit shown in part (B) of this figure. Dashed curves are plots of  $I_G$  vs.  $V_{DS}$ . The composition of the bubble film is  $(Y_{1.00}Sm_{0.39}Tm_{0.92}Ca_{0.69})\{Ge_{0.70}Fe_{4.30}\}O_{12}$ . The channel length/width ratio of the MOSFET is  $25\mu m/25\mu m$ .

(B) Device model for a MOSFET with non-zero, catastrophic gate leakage current.



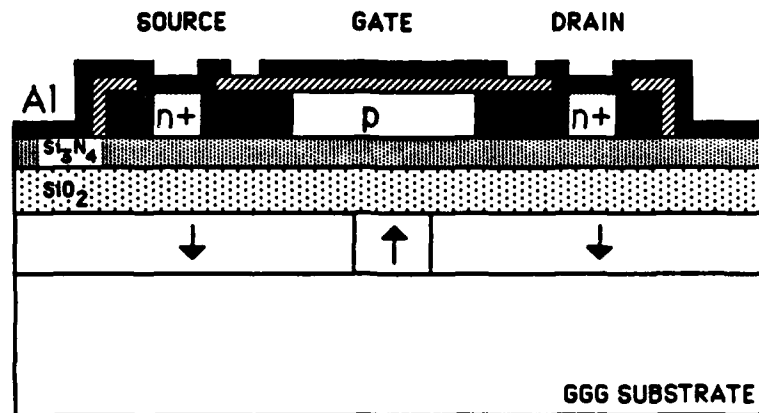


Figure 8: Cross section of a silicon on garnet MOSFET with a double layer spacer.

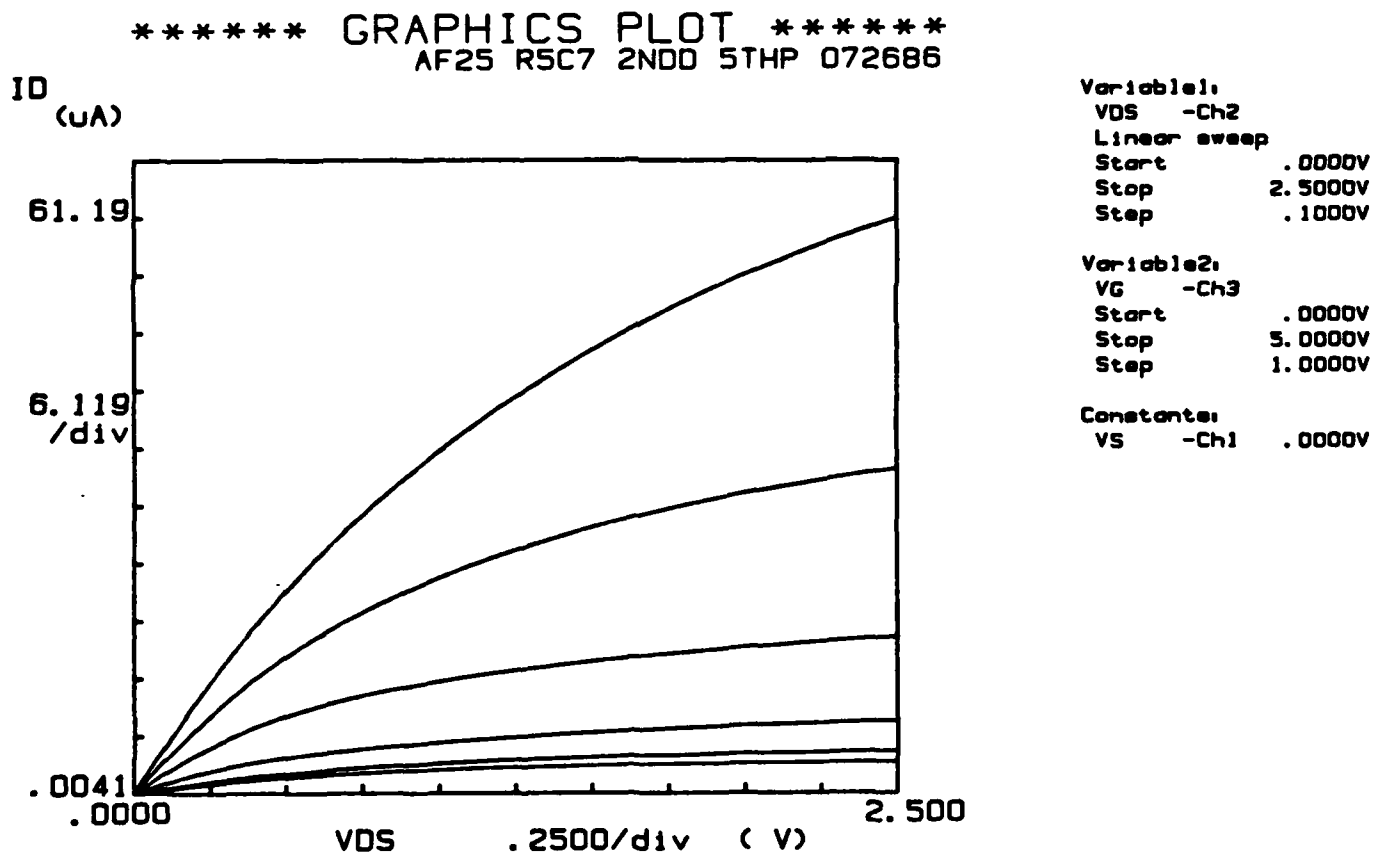


Figure 9: Drain characteristics for a device with the structure shown in Fig. 8. The  $\text{SiO}_2$  spacer layer is  $0.41 \mu\text{m}$  thick and the  $\text{Si}_3\text{N}_4$  film is  $0.85 \mu\text{m}$  thick. The composition of the magnetic bubble layer is  $\text{Sm}_x\text{Tm}_y\text{Lu}_{3-(x+y)}(\text{Fe}_{5-z}\text{Ga}_z)\text{O}_{12}$ . The channel length/width ratio of the MOSFET is  $17\mu\text{m}/35\mu\text{m}$ .

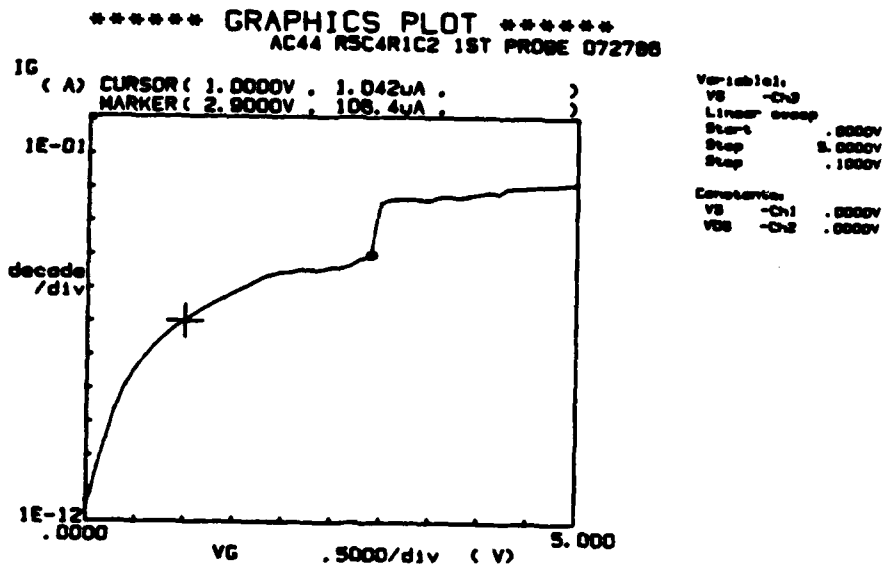


Figure 10:

A plot of the gate leakage current  $I_G$  vs. the gate voltage  $V_G$  with the drain and source at ground potential ( $V_{DS}=0V$ ). The structure of the device is like that of Fig. 5. A sputtered  $\text{SiO}_2$  layer served as the spacer and was  $\sim 1\mu\text{m}$  thick. The composition of the magnetic bubble layer is  $(\text{Sm}_{1.2}\text{Lu}_{1.7}\text{Tm}_{0.1})\{\text{Fe}_{5-z}\text{Ga}_z\}\text{O}_{12}$ . The channel length/width ratio of the MOSFET is  $12.5\mu\text{m}/25\mu\text{m}$ .

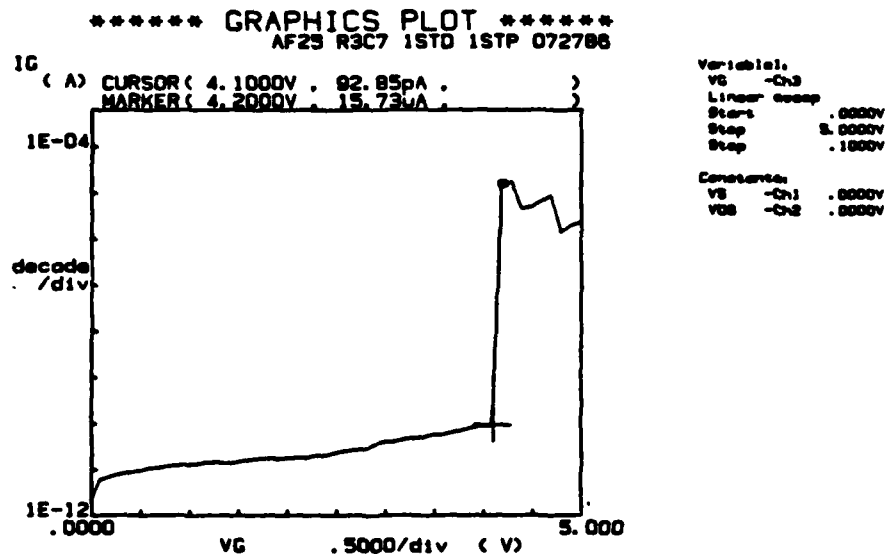
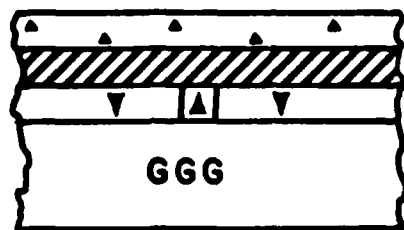


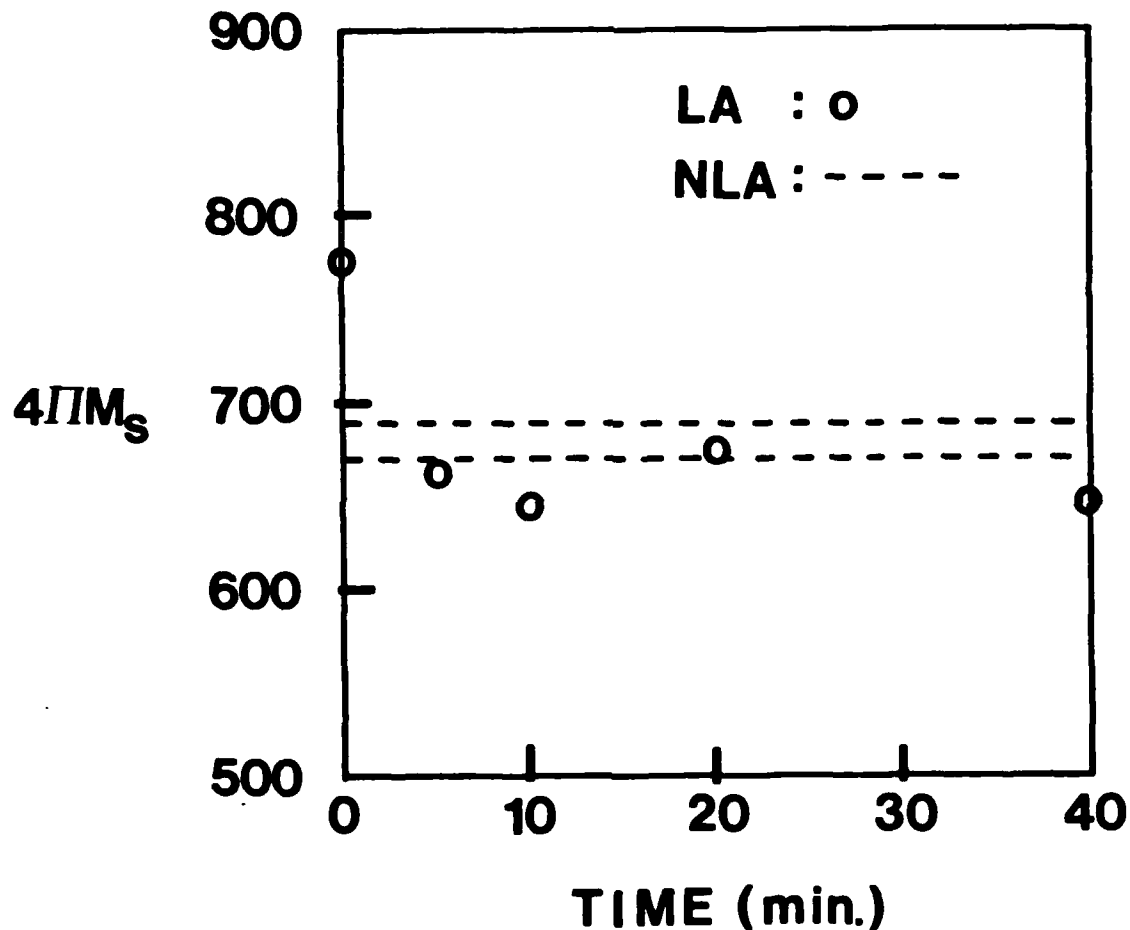
Figure 11:

A plot of the gate leakage current  $I_G$  vs. the gate voltage  $V_G$  with the drain and source at ground potential ( $V_{DS}=0V$ ). The structure of the device is like that of Fig. 8. The  $\text{SiO}_2$  spacer layer is  $0.41\mu\text{m}$  thick and the  $\text{Si}_3\text{N}_4$  film is  $0.85\mu\text{m}$  thick. The composition of the magnetic bubble layer is  $\text{Sm}_x\text{Tm}_y\text{Lu}_{3-(x+y)}(\text{Fe}_{5-z}\text{Ga}_z)\text{O}_{12}$ . The channel length/width ratio of the MOSFET is  $17\mu\text{m}/35\mu\text{m}$ .



LPCVD Poly-Si  $\sim 0.75 \mu\text{m}$   
 SPUTTERED  $\text{SiO}_2 \sim 1 \mu\text{m}$  (Spacer Layer)  
 BUBBLE LAYER  
 SUBSTRATE

(A)



(B)

Figure 12:

(A) Silicon on garnet cross section for a simple process.

(B)  $4\pi M_s$  after  $850^\circ\text{C}$  oxygen post-laser anneals. The post-laser anneals were 5 to 40 min. in length. The data point at 0 min. is for a sample that did not receive a post-laser anneal. The composition of the magnetic bubble layer is  $(\text{Sm}_{0.3}\text{Gd}_{0.4}\text{Tm}_{0.73}\text{Y}_{1.57})\{\text{Fe}_{4.6}\text{Ga}_{0.4}\}\text{O}_{12}$ .

	$4\pi M_s$		$W_0 = \frac{P_0}{2}$		
	1 $\mu\text{m}$	0.5 $\mu\text{m}$	1 $\mu\text{m}$	0.5 $\mu\text{m}$	
As Grown	738	1366	1.43	0.69	23°C
0.41 $\mu\text{m}$ LPCVD $\text{SiO}_2$	573	1270	1.79	0.68	64 min. 860°C
0.24 $\mu\text{m}$ LPCVD $\text{Si}_3\text{N}_4$	593	1262	1.87	0.67	11 min. 800°C
0.55 $\mu\text{m}$ LPCVD Poly-Si	531	1214	1.87	0.64	50 min. 625°C
After Laser Anneal	591	1171	1.15	0.59	350-1412°C

Table 1: The saturation magnetization  $4\pi M_s$  and the zero field strip width  $W_0$  at room temperature after typical silicon on garnet process steps. The composition of the magnetic bubble layer is  $\text{Sm}_x\text{Tm}_y\text{Lu}_{3-(x+y)}(\text{Fe}_{5-z}\text{Ga}_z)\text{O}_{12}$ .

# Contiguous Disk Ion Implanted Magnetic Bubble Memory Devices

Soonchul Jo and M.H.Kryder

## Introduction

Ion implanted magnetic bubble devices<sup>1</sup> offer an order of magnitude increase in memory density over conventional permalloy devices for a given minimum lithographic feature. This becomes an increasingly important advantage over the permalloy devices as the memory cell size shrinks. In fact, some of the down sized 4 megabit commercial devices are expected to employ ion implanted bubble storage loops (minor loops) instead of permalloy ones and most concerned agree that ion implanted minor loops should be used for the next generation (16 megabit) devices due to the smaller lithographic minimum feature required for the permalloy devices.

In ion implanted devices, charged walls are utilized to move bubbles along the propagation tracks, which are defined by ion implantation. Figure 1 shows a unit cell of such a track.

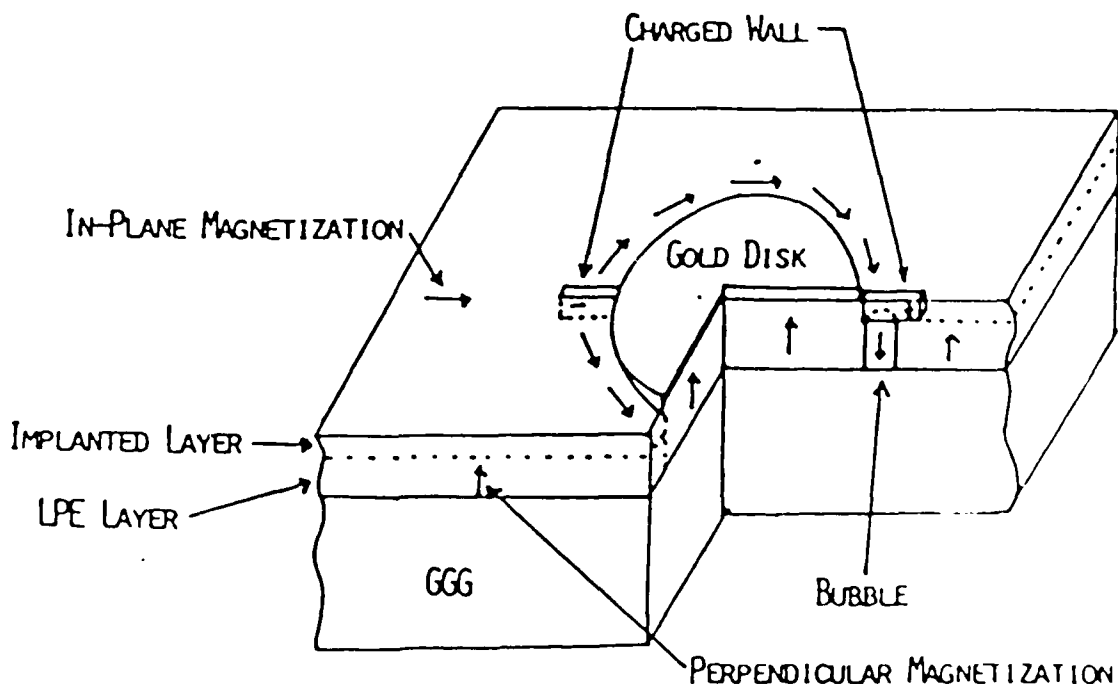


Figure 1: Perspective View of an Ion Implanted Bubble Propagation Cell

Charged walls are formed at the edges of the propagation tracks and can be moved around by applying a rotating in-plane magnetic field. Bubbles are attracted to the charged walls and follow the movement of them. But this movement of charged walls is not smooth and uniform around the track, instead it shows three fold symmetric behavior, which reflects the three fold symmetry of the garnet crystal. This causes a major difficulty in device design because it results in much worse propagation margins in tracks oriented

in some direction ("bad" track) than others <sup>2,3</sup>("good" or "super" tracks). The mechanisms of the charged wall formation and the three fold symmetric behavior were not well understood until recently Hidaka and Matsutera<sup>4</sup> and, independently Backerra et al.<sup>5</sup> pointed out that partial stress relaxation at the boundary of the unimplanted and implanted regions is necessary to form charged walls. Subsequent studies by Kryder and Saunders<sup>6</sup> and, independently Hubert<sup>7</sup> show that partial stress relaxation at the boundary is primarily responsible not only for the formation of the charged walls, but also for the three fold symmetry behavior of the charged walls around the ion implanted patterns. They also pointed out that the three fold symmetry behavior of charged walls can be virtually eliminated by properly choosing magnetostriction coefficients ( $\lambda_{100}$  and  $\lambda_{111}$ ) of the magnetic layers. Their theory predicts that if  $\lambda_{100}$  is approximately equal to  $\lambda_{111}$ , the three fold magnetostrictive anisotropy will almost disappear, and bubbles will propagate smoothly along the tracks regardless of their orientations, resulting in isotropic propagation.

The temperature dependence of magnetic bubble propagation is of great practical interest because it essentially determines the operating temperature range of the magnetic bubble memory devices. It has been reported that the operating temperature range of ion implanted devices depends on the garnet film characteristics and the ion implantation conditions. Mizuo and Urai<sup>8</sup> demonstrated that hydrogen implantation allows much higher operating temperature limits than the helium implantation for the same garnet films. Fratello et al.<sup>9</sup> and Arbaugh and Fairholme<sup>10</sup> showed that bismuth substituted garnet films gave wide operating temperature range.

Our objectives of research have been two fold; firstly, design and fabrication of good working ion implanted propagation track devices for 0.5  $\mu\text{m}$  bubbles (which can be used for 16 megabit memory devices) and secondly, experimental investigation of the influence of the three fold magnetostrictive anisotropy due to stress relaxation on device performance using aforementioned propagation track devices. During the past year, propagation tracks of various shapes and different orientations for 0.5  $\mu\text{m}$  bubbles were fabricated and tested. Some of the results was published in the September issue of the IEEE Transactions of Magnetics<sup>11</sup> and others will be presented in the upcoming Magnetism and Magnetic materials Conference in Baltimore<sup>12</sup>. In this report, we describe an experimental study of propagation of 0.5  $\mu\text{m}$  bubbles in (111) garnets having nearly isotropic magnetostriction. The effects of pattern geometry, ion implantation conditions, propagation direction and ambient temperature variation are all considered.

## Experimental

Propagation tracks with various cell shapes and different orientations were fabricated on 0.5  $\mu\text{m}$  bubble garnet films with small  $\delta\lambda(=\lambda_{100}-\lambda_{111})$ . Garnet films used for the device fabrication are bismuth and dysprosium substituted iron garnets grown by liquid phase epitaxy. The characteristics of one of the films (CA 71) studied are shown in Table 1. The other film (CA 72) studied has slightly different film

characteristics than CA 71, the main difference being somewhat higher effective uniaxial anisotropy (by 250 Oe).

**Table 1:** Garnet Film Characteristics (CA 71)

Composition	$\{\text{Bi}_{0.4}\text{Dy}_{0.7}\text{Sm}_{0.2}\text{Lu}_{1.5}\text{Y}_{0.2}\}[\text{FeGa}]_5(\text{O})_{12}$
Thickness $t$	$0.65\mu\text{m}$
Collapse field $H_0$	580 Oe
Material length $l$	$0.054\mu\text{m}$
Magnetization $4\pi M$	960 G
Uniaxial anisotropy $H_k$	1850 Oe
Quality factor $Q$	1.9
Bubble diameter $d$	$0.5\mu\text{m}$
Magnetostriction coeff. $\lambda_{111}$	$-3.1 \times 10^{-6}$
$\lambda_{100}$	$-2.1 \times 10^{-6}$

Ion implantation masks for propagation patterns were formed by electroplating gold through a photolithographic mask. Firstly, 80 nm of  $\text{SiO}_2$  and the plating base (Mo and Au) were sputtered on the film. Then, photoresist patterns were delineated using 500 nm thick AZ 4070 resist and a Karl Suss contact aligner with a mid U.V. (310 nm) light source. Then, 350 nm of gold was electroplated using Selrex Corporations' BDT 510 gold bath. Current density used was  $3\text{ mA/cm}^2$ . After the electroplating, deuterium was doubly implanted to define the propagation tracks. Implantation energies and dosages were varied to find optimum conditions for bubble propagation. Implantation energies and dosages which give approximately 230 nm of implantation depth and relatively uniform implant with in plane  $Q$  of -2.5, gave good propagation margins for most of the  $2.5\mu\text{m}$  period patterns. The ion implantation conditions are listed in Table 2.

**Table 2:** Ion Implantation Conditions

	Ion species	Energy	Dosage
1st implantation	Deuterium	46 Kev	$7.5 \times 10^{15}/\text{cm}^2$
2nd implantation	Deuterium	26 Kev	$5 \times 10^{15}/\text{cm}^2$

Finally, the gold implantation masks together with the plating base were stripped with Au etchant and aluminum was evaporated to be used as the reflection layer for the observation of bubbles by a polarized light microscope. High Faraday rotation due to Bi substitution in the garnet film and the Al mirror gave excellent visibility so that bubbles were easily observed up to collapse.

The devices were tested by measuring quasi-static (1 Hz) bias margins for "good" and "bad" tracks. Data patterns were randomly generated by slowly raising the bias field from the bubble stripe out state. Propagation around the corners was included in the bias margin measurements and the number of cycles of propagation varied from a few tens to 250. The propagation pattern shapes studied in this paper are illustrated in Figure 1.

Temperature variation of the propagation tracks was achieved by changing the ambient temperature of the device. The device chip was placed at the center of a double donut shaped bias magnet and the magnet was sealed. Then, temperature controlled air or dry nitrogen was blown in to maintain the desired temperature. The temperature was monitored by a thermocouple placed near the device. Enough time was allowed for the chip to reach a temperature equilibrium before any measurement was made. The accuracy of the temperature controller was  $\pm 1^\circ\text{C}$  throughout the temperature range tested.

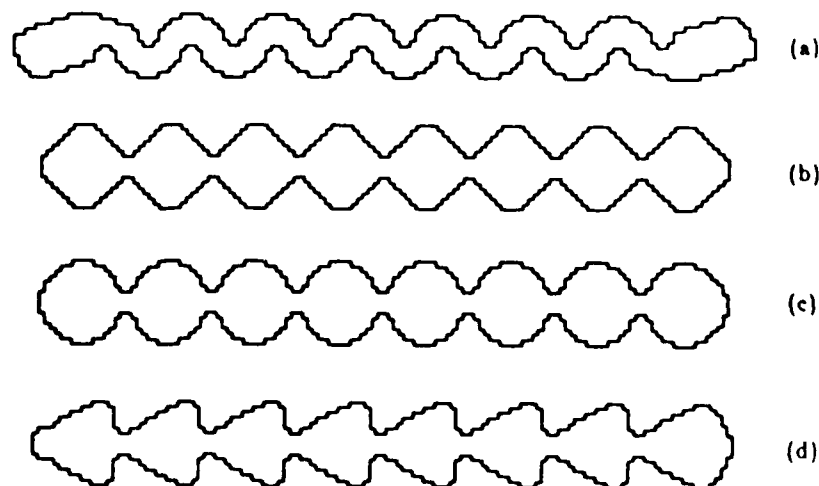


Figure 2: Bubble Propagation Shapes  
(a) Snake (b) Diamond (c) Circle (d) Triangle

## Results and Discussion

Quasi-static bias margins of "good" and "bad"  $2.5\ \mu\text{m}$  period tracks for diamond, circle, triangle and snake shaped bubble propagation patterns were measured. Figures 3,4 and 5 show results obtained from film CA71. "Good" and "bad" track margins for diamond shaped patterns are shown in Figure 3, which show almost identical bias margins for "good" and "bad" tracks with the minimum in plane drive field of 30 Oe and the margin width of 80 Oe (15% of the mid bias). This is a dramatic improvement of "bad" track margins over those typically seen in ion implanted devices with conventional garnet films<sup>2</sup>.

Bias margins for other cell shapes show slightly higher minimum drive fields for "bad" tracks, but similar margin widths for both tracks except the snake shape. Overlapping bias margins of "good" and



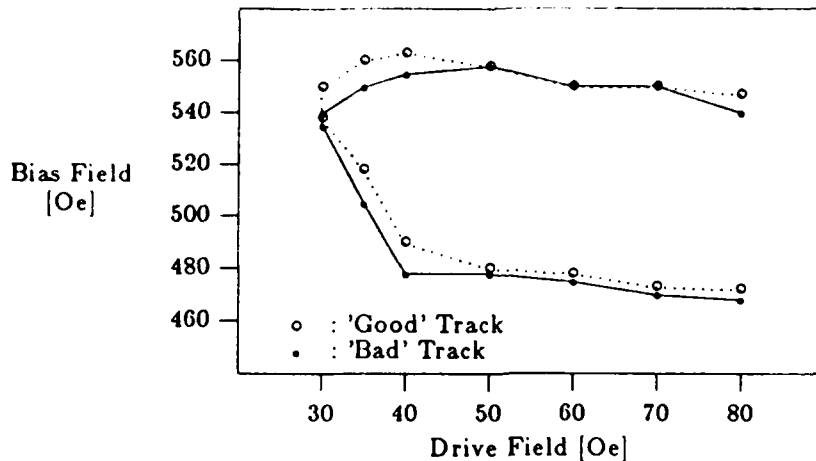


Figure 3: Margins for 2.5  $\mu\text{m}$  period Diamond Shaped propagation pattern Film CA 71

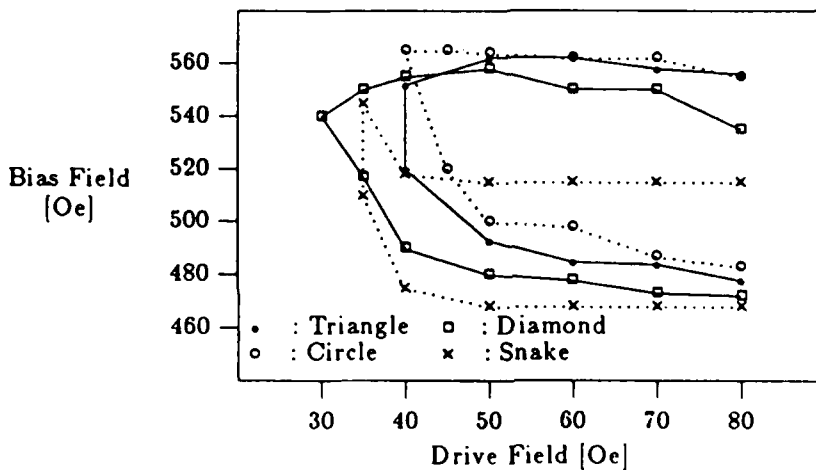


Figure 4: Overlapping Margins for 2.5  $\mu\text{m}$  Period Diamond, Triangle, Circle and Snake Patterns Film CA71

"bad" tracks for diamond, triangle, circle and snake shaped propagation tracks are shown in Figure 4. The best overlapping margins are obtained from the diamond shape and the worst from the snake. The reason that the snake patterns have the worst overlapping bias margins is mainly due to the skidding of bubbles along the bad tracks (propagation of more than one period of the track during one cycle of the in-plane drive field) at high bias fields. On the other hand, the snake patterns show the best "good" track margin (25 Oe minimum drive and 15% margin width). The "good" and "bad" track bias margins for snake patterns are plotted in Figure 5.

Figures 6 and 7 illustrate bias margin measurements obtained from snake patterns on film CA 72. CA 72 has slightly different film characteristics than CA71, the main difference being somewhat higher effective uniaxial anisotropy (by 250 Oe). Ion implantation conditions were the same as CA 71, which

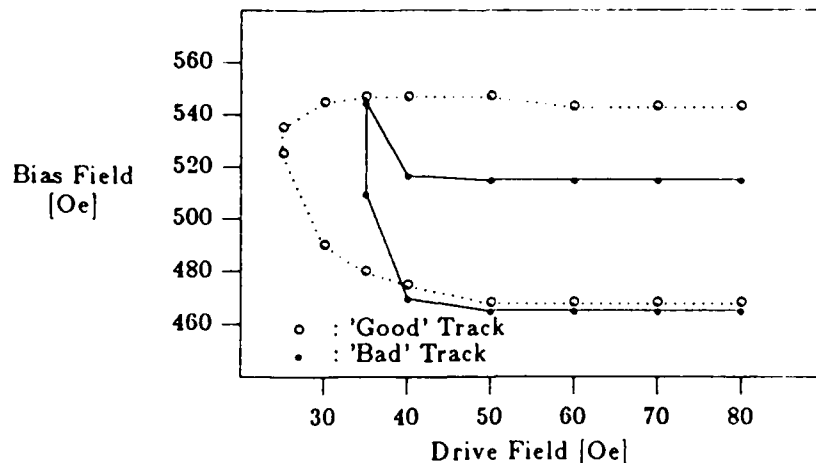
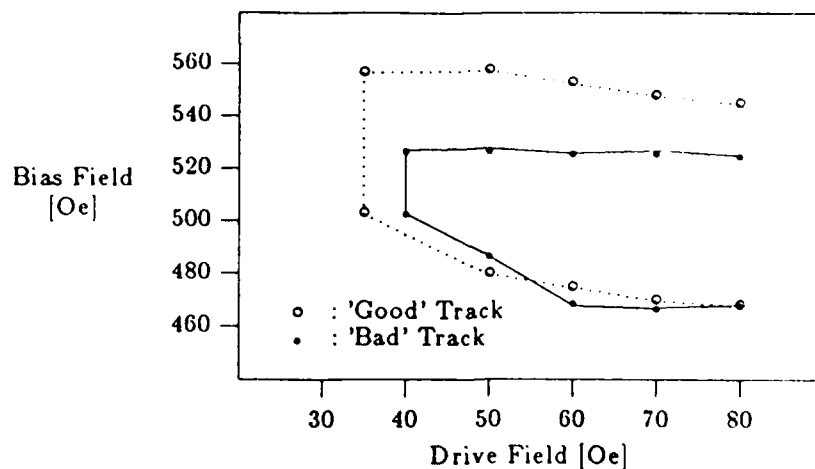


Figure 5: Margins for 2.5  $\mu\text{m}$  Period Snake Shaped Patterns  
Film CA71

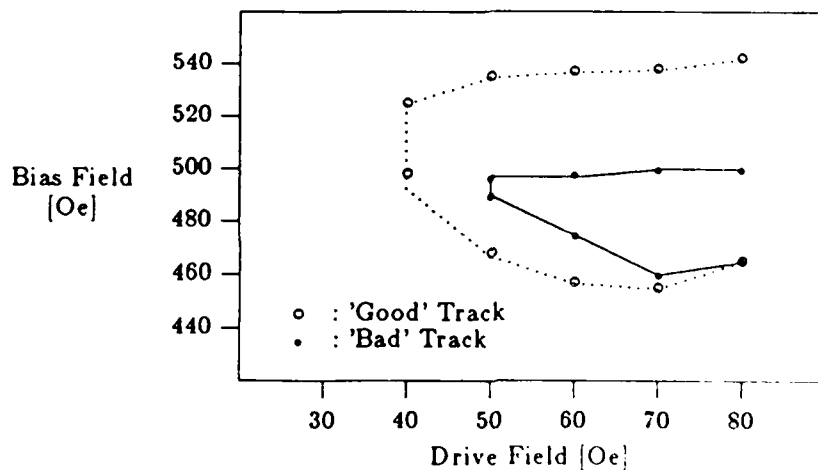
were shown in Table 1. "Good" and "bad" track margins for 2  $\mu\text{m}$  period snake patterns are shown in Fig. 6. Figure 6 (a) shows the results obtained from the patterns with the cusp depth to track period ratio of 0.44, while Figure 6 (b) shows margins from the patterns with the cusp depth to track period ratio of 0.38. It is clear from the margin plots that a slight change of cusp dimension ( $1/8 \mu\text{m}$ ) could significantly affect the bias margins, especially for the "bad" tracks. It seems from these plots and previous margin plots of film CA 71 that sharper cusp definition (for example, snake patterns with deeper cusps and diamond patterns) help prevent bubbles from skidding along "bad" tracks. As Lin et al.<sup>1</sup> pointed out, wider and smoother cusps yield better margins as demonstrated in "good" snake patterns. But, at the same time such cusps seem to promote the skidding failure mode in "bad" tracks.

Figure 7 shows bias margins for 2.5  $\mu\text{m}$  period snake patterns made with film CA 72. They have the same cusp shape as the patterns whose margins are shown in Figure 5 (CA 71). CA 71 and CA 72 were ion implanted with the same conditions and at the same time as noted earlier. The main difference in the films was that CA 72 had somewhat higher effective anisotropy than CA 71 (by 250 Oe). Thus, this resulted in a slightly lower (magnitude) in-plane  $Q$  for CA 72 than CA 71. The "bad" track margin shows considerable improvement in margin width compared with CA 71, even though the minimum drive field of the good track margin has increased slightly (by 5 Oe). Still, the overlapping bias margin is significantly better than the margin of CA 71, which exhibits a minimum drive of 35 Oe and margin width of 70 Oe (14% of mid bias value).

The failure mechanism of the "bad" tracks in the snake pattern at high bias fields was bubble collapse at low and medium drive and bubble skidding at high drive. This contrasts to the predominant skidding failure mechanism of film CA 71. This shows that with proper ion implantation, we can largely avoid skidding failures at high bias, producing good "bad" track propagation. It is to be noted that the



(a)



(b)

**Figure 6:** Margins for 2  $\mu\text{m}$  Period Snake Patterns with  
 (a) Cusp to Period Ratio of 0.44 (b) Cusp to Period Ratio of 0.38  
 Film CA 72

skidding failure mode is not limited to snake patterns. It was observed in other propagation patterns with different ion implantation conditions.

"Good" and "bad" track bias margins of diamond and circular propagation patterns of sample CA 72 were measured from 0 °C to 130 °C. Figure 8 shows the temperature dependence of the minimum drive fields of diamond and circular propagation patterns as a function of temperature. The curves show a monotonic decrease of the minimum drive as the temperature is increased. The decrease of the minimum drive was previously attributed to the decrease of the cubic magnetocrystalline anisotropy<sup>8</sup>. Since it is

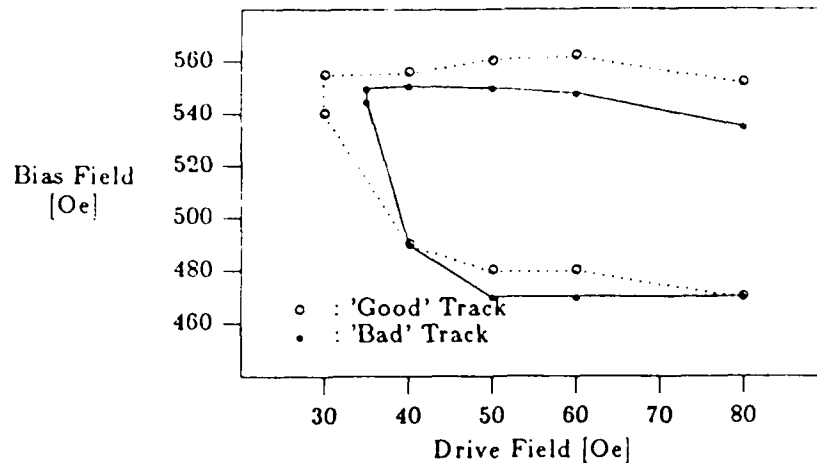
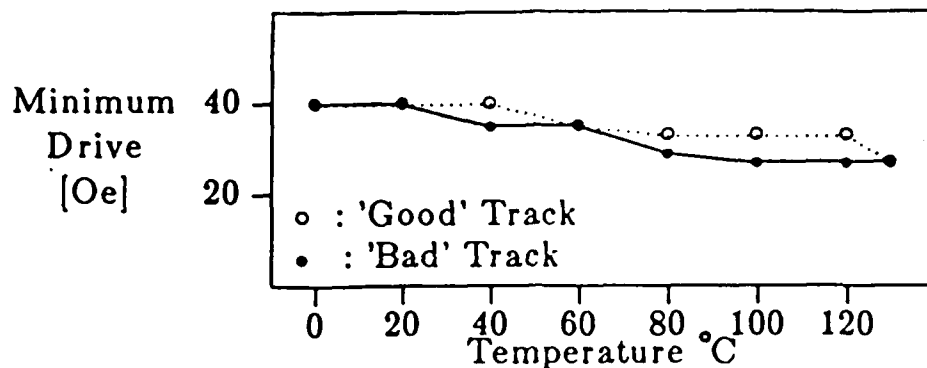


Figure 7: Margins for 2.5  $\mu\text{m}$  Period Snake Patterns  
Film CA 72

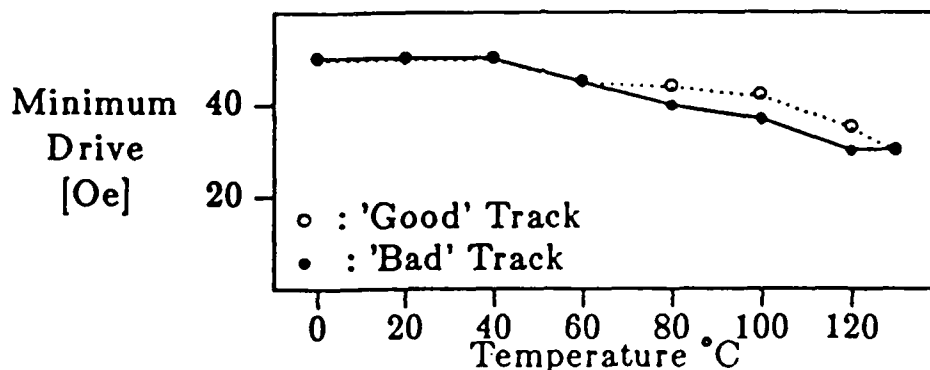
now believed that the dominant source of the three fold anisotropy is the magnetostrictive anisotropy due to partial relaxation of the stress at the boundary of the implanted and unimplanted regions<sup>6,7</sup>, it seems to be more reasonable to assume that the decrease of the minimum drive is mainly due to the decrease of the magnetostriction coefficients and the difference of the two coefficients  $\lambda_{111}$  and  $\lambda_{100}$  which is proportional to the anisotropy energy<sup>6</sup>. The temperature dependence of magnetostriction coefficients of  $\text{Sm}_3\text{Fe}_5\text{O}_{12}$  and  $\text{Dy}_3\text{Fe}_5\text{O}_{12}$  as well as the difference of the two coefficients shows a steady decrease as the temperature increases<sup>13</sup>. Since the magnetostriction coefficients of our garnet film are mainly determined by Dy and Sm, the above explanation seems to be reasonable. Diamond patterns showed lower drive fields for both "good" and "bad" tracks (less than 40 Oe). It is interesting to see that the minimum drive fields for supposedly "bad" tracks are actually lower than "good" tracks for most of the temperature range. This will be explained later on.

Figure 9 shows bubble propagation bias margins at 60 Oe drive field as a function of chip temperature of diamond and circular patterns. The margins shifted downward monotonically as the temperature increased with a coefficient of roughly  $-0.27\%/^{\circ}\text{C}$  (at 50  $^{\circ}\text{C}$ ). Diamond patterns showed the wider overlapping margin of "good" and "bad" tracks (80 Oe or 15% of mid bias value at 40  $^{\circ}\text{C}$ ). Circular patterns showed almost no margin width variation throughout the temperature range tested. At 130  $^{\circ}\text{C}$ , they still showed 55 Oe (14% of mid bias) of overlapping bias margin. Margin degradation at high temperature was due to a decrease of collapse field at high drive field.

It is interesting to note that the collapse field of the "bad" tracks in most of the temperature range is actually slightly higher than that of "good" tracks. The reason why the collapse field of "bad" tracks is higher than that of "good" tracks is as follows. To understand the problem, we observed the charged wall (and bubble) direction as a function of drive field around an unimplanted disk of diameter 4  $\mu\text{m}$  at



(a)



(b)

Figure 8: Temperature dependence of minimum drive field for (a) diamond and (b) circular patterns

low drive field (15 Oe). The crystal orientation of the disk and bubble jumping directions due to charged wall flip motion<sup>14</sup> are shown in Figure 10 (a). The  $[1\bar{1}2]$  direction is designated as  $0^\circ$  of rotation. As is shown in the figure, charged wall (and bubble) jumping occurs at  $20^\circ$ ,  $180^\circ$  and  $290^\circ$ . Figure 10 (b) shows propagation tracks oriented in the "good" direction( $[1\bar{1}2]$ ) and "super" and "bad" direction (perpendicular to "good" direction). Short lines around the tracks indicate in-plane drive field directions where the charged wall flip motion or the bubble jumping occurs. It is to be noted at this point that the most difficult part of the propagation process is to move the bubbles out of the cusps. Suppose that the drive field rotates in a clockwise direction. Bubbles leaving cusps from the bottom side of the "good" tracks are subject to charged wall jumping as they start to move out of the cusps while bubbles on the top side of the tracks do not encounter such adverse conditions as they leave the cusps. Therefore, the failure mode at high bias is bubble collapse at the bottom cusps.

Now consider the "bad" track. Here, bubbles are subject to charged wall jumping after they come out

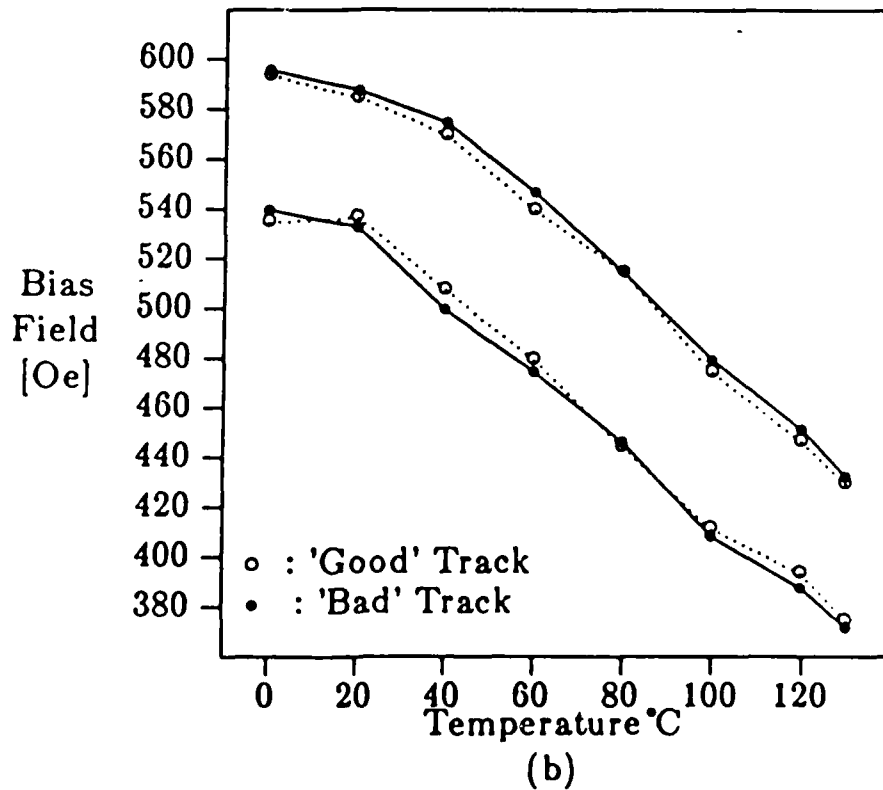
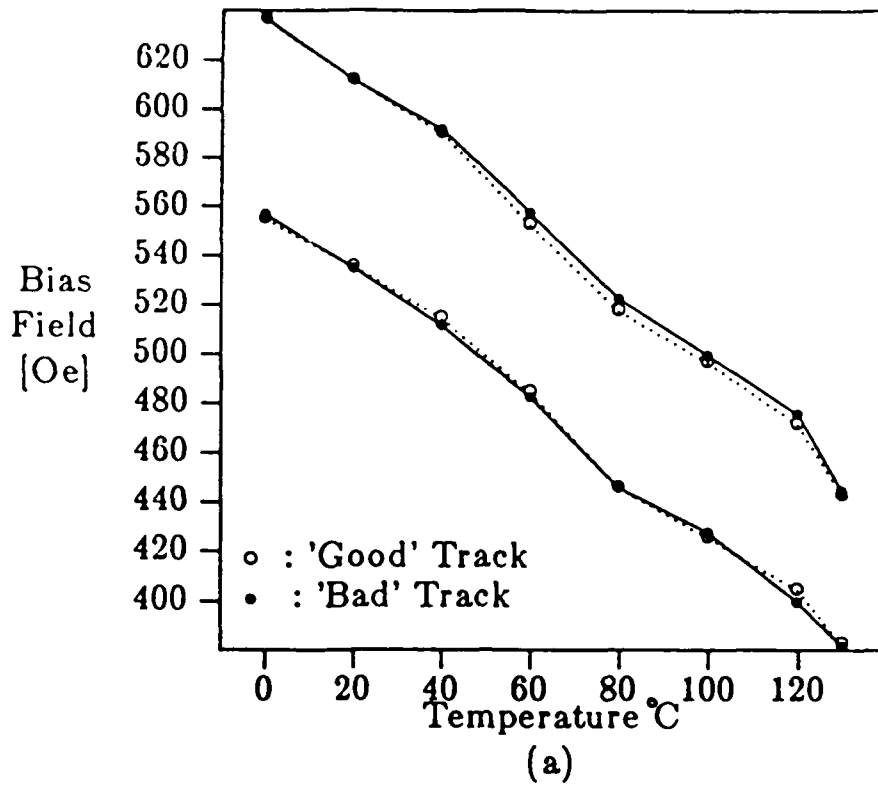
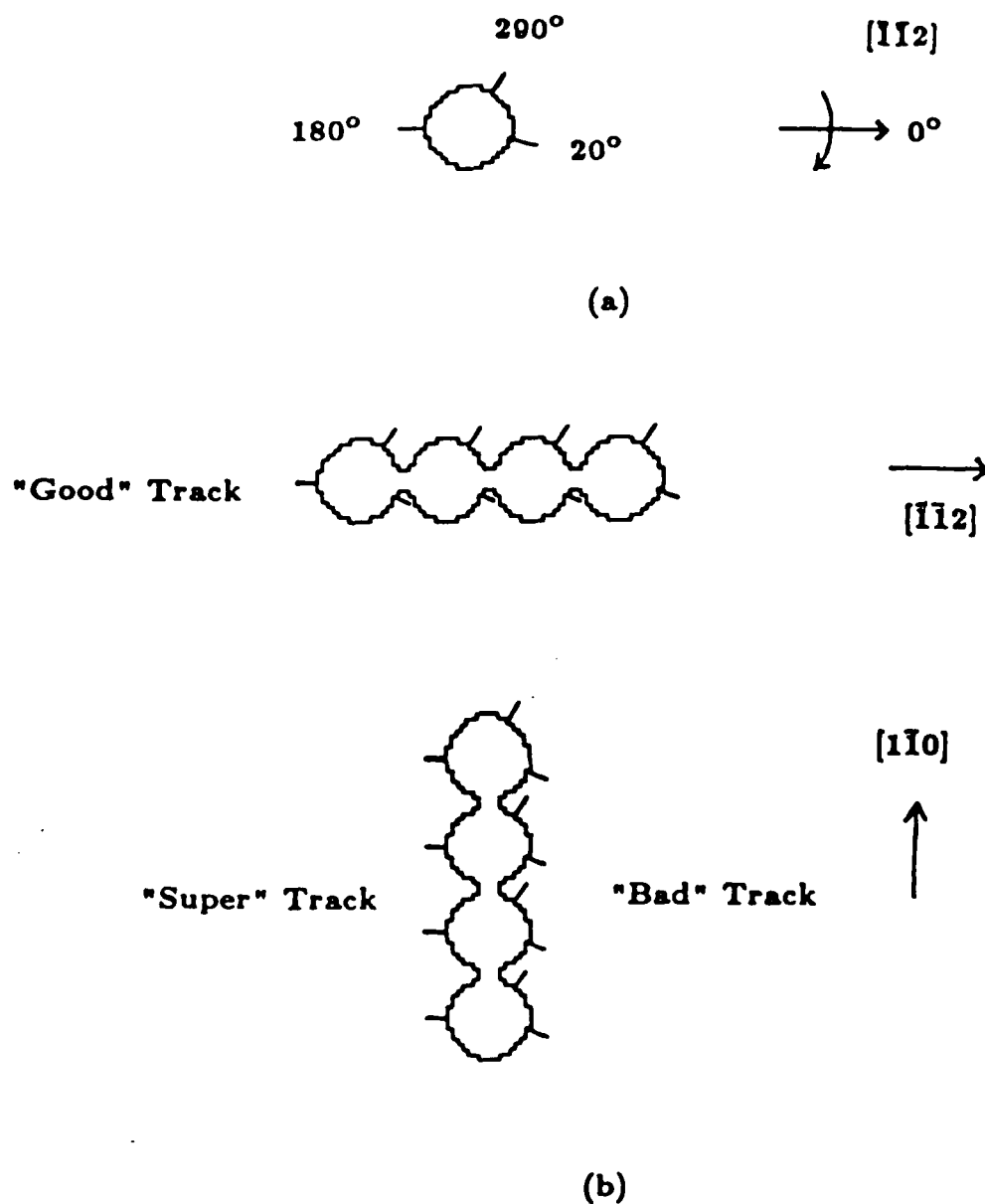


Figure 9: Temperature dependence of bias margin at 60 Oe of drive field for (a) diamond and (b) circular patterns



**Figure 10:** Charged wall flip (and bubble jumping) directions of (a) unimplanted disk and (b) propagation tracks

of the cusps. Therefore bubbles can follow the jumping motion of the charged wall relatively well and thus have higher collapse field. This charged wall behavior difference is believed to be responsible for the slightly higher collapse field of "bad" tracks than "good" tracks. It is to be remembered that the garnet film is nearly isotropic to begin with.

Futher evidence to support this explanation is found by reversing the in-plane field rotation direction.

Now bubbles both on the top side of the "good" track and on the "bad" track encounter charged wall jumping after they get out of the cusps. Therefore, we expect that the bubbles on both tracks will behave similarly. It is to be noted that all the margin plots presented so far were measured using clockwise rotating in-plane fields. Figure 11 shows bias margins of diamond patterns obtained by clockwise (a) and counterclockwise (b) rotating in-plane fields. Figure 11 (b) shows an increase of "good" track collapse field and almost identical bias margins for both "good" and "bad" tracks. This is in agreement with our explanation above.

As was mentioned earlier, the minimum drive field of "bad" tracks are generally lower than that of "good" tracks. By looking at Figures 8 and 9, we find excellent correlation between the minimum drive field and the collapse field of respective "good" and "bad" tracks. When the collapse field of the "bad" track is higher than that of the "good" track, the minimum drive of the "bad" track is lower than that of the "good" track and vice versa. This is easily explained by the previous argument. When the collapse field is higher, it is easier for the bubbles to come out of the cusps, therefore the minimum drive is lower and vice versa.

### Conclusions

Bubble propagation tracks of various cell shapes were fabricated on bismuth substituted  $0.5 \mu\text{m}$  garnet films with small magnetostriction coefficient difference. Bias margin measurements show great improvement of "bad" track margins for all cell shapes tested. Diamond shaped patterns exhibited the best overlapping bias margins. Although snake shaped patterns show the best "good" track margins, their "bad" track margins are most susceptible to a skidding failure mechanism at high bias fields, which could significantly degrade the margins. It was found that "bad" track margins (notably of snake patterns) are very sensitive to ion implantation conditions and pattern cusp shape. Nearly isotropic bubble propagation was achieved for all the track shapes tested by careful adjustment of ion implantation conditions and track cusp shape. The temperature dependence was measured over the temperature range of  $0^\circ\text{C}$  to  $130^\circ\text{C}$ . The results show good overlapping bias margins of "good" and "bad" tracks up to  $120^\circ\text{C}$  (at least 13% of mid bias). The wider overlapping margin width (at least 14% of mid bias) and the lower minimum drive field (at most 40 Oe) over the temperature range tested were obtained from the diamond patterns. Circular patterns showed a consistent margin width (60 Oe) throughout the temperature range. The patterns exhibited slightly higher collapse fields for "bad" tracks than "good" tracks depending on the rotation sense of the drive field. This is explained by the fact that the charged wall flip motion occurred when the bubble was being pulled out of a cusp for the "good" tracks, but after coming out of a cusp for the "bad" tracks.



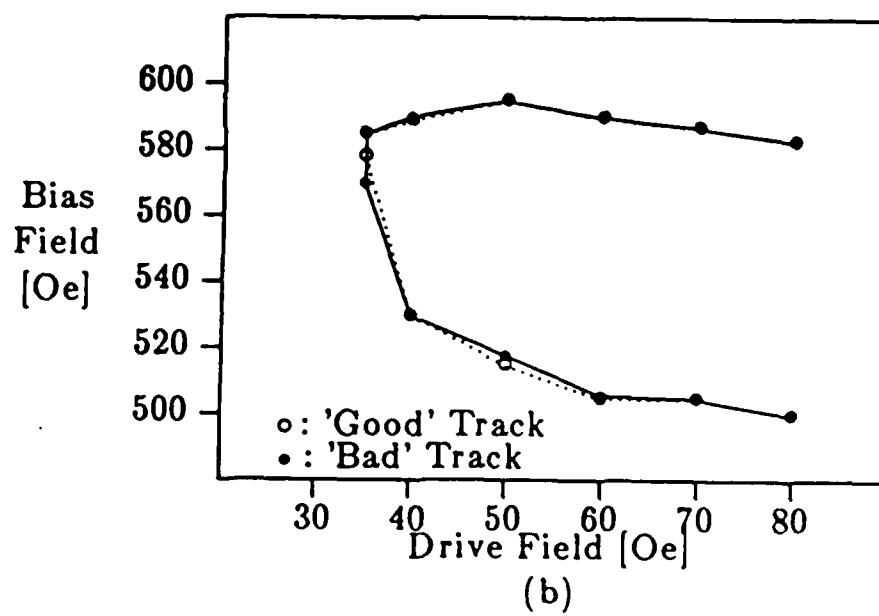
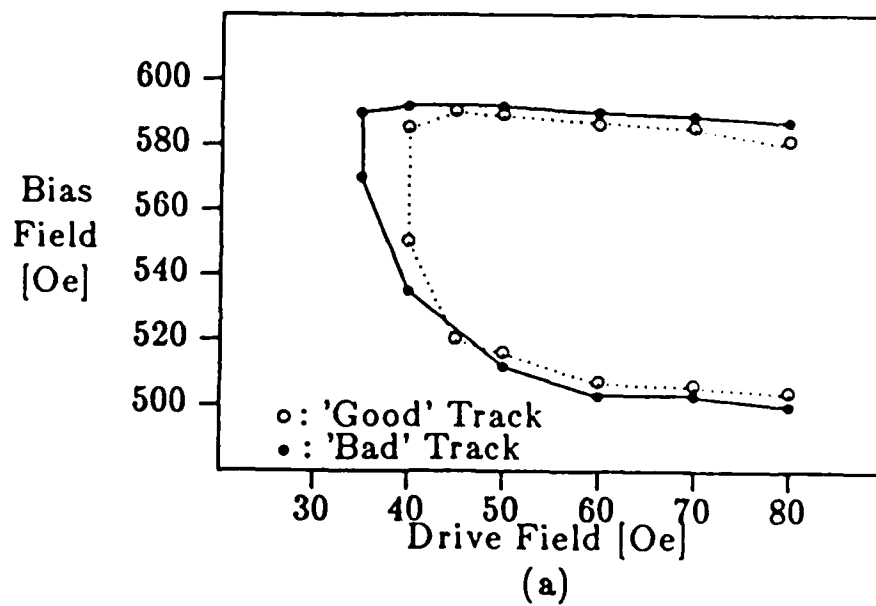


Figure 11: Bias margins of diamond patterns with (a) clockwise and (b) counterclockwise rotating drive field at 40 °C

### Future work

More propagation track devices will be fabricated on garnet films with various combinations of magnetostriction coefficients ( $\lambda_{111}$  and  $\lambda_{100}$ ). By testing these devices, charged wall formation and bubble propagation mechanisms will be studied and related to the three fold magnetostrictive anisotropy.

### References

1. Y.S. Lin, G.S. Almasi and G.E. Keefe, IEEE Tran. Mag., MAG-13, No.6, 1744(1977).
2. Y.S. Lin, G.S. Almasi, D.B. Dove, G.E. Keefe and C.C. Shir, J. Appl. Phys., 50(3), 2258(1979)
3. R. Wolfe and T. J. Nelson, IEEE Tran. Mag., MAG-15, No.5, 1323 (1979).
4. Y. Hidaka and H. Matsutera, Applied Physics Letters, 39 No.1, 116 (1982).
5. S.C.M. Backerra, W. H. De Roode and U. Enz, Phillips J. Res., 36, 112 (1980).
6. M.H. Kryder and D.A. Saunders, IEEE Tran. Mag., MAG-19, No.5, 1817(1983).
7. A. Hubert, J. Magnetism and Magnetic Materials, 31-34, 976(1983).
8. K. Mizuno and H. Urai, IEEE tran. Mag., MAG-21, No.5, 1706(1985)
9. V.J. Fratello, R.D. Pierce and C.D. Brandle, J. Appl. Phys., 57(8), 4043(1985).
10. L.G. Arbaugh Jr. and R.J. Fairholme, IEEE tran. Mag., MAG-22, No.5, 1287(1986)
11. S. Jo and M.H. Kryder, IEEE tran. MAG., MAG-22, No.5, 1278(1986)
12. S. Jo and M.H. Kryder, To be presented at the Magnetism and Magnetic Materials Conference in Baltimore
13. G. Winkler, *Magnetic Garnets*, Friedr. Vieweg & Sohn, 1981.
14. Y.S. Lin, D.B. Dove, S. Schwarzl and C.C. Shir, IEEE Tran. MAG., MAG-14, No.5, 494(1978)

# LPE GROWTH OF MAGNETIC BUBBLE GARNETS.

M. Ramesh, R. O. Campbell and M. H. Kryder.

Department of Electrical and Computer Engineering.

Carnegie Mellon University, Pittsburgh, Pa 15213.

## Section I Introduction

The main thrust of our LPE garnet film growth program is to develop films suitable for fabrication of high density, high performance magnetic bubble devices. In order to achieve the desired high storage densities, it is necessary to go for films which can support sub-micron diameter bubbles. We have been able to develop several such materials that are useful for device work. In particular, we focus our efforts in developing  $0.5 \mu\text{m}$  diameter bubble films, which have ideal material properties.

Most bubble devices fabricated on the films developed in our facility use Ion-Implanted Contiguous Disk patterns on garnets. This has hitherto been complicated by the anisotropy in propagation margins in these films. Devices fabricated on a  $[111]$  garnet film<sup>1,2</sup>, for example, have been shown to exhibit a three-fold symmetry for bubble propagation. Those tracks parallel to  $[11\bar{2}]$  direction were found to have acceptable margins (Referred to as 'good tracks'), whereas for tracks oriented perpendicular to  $[11\bar{2}]$ , very large propagation margins were observed for one side ('super tracks') with anomalously small margins on the other side ('bad tracks'). Although, initially this three-fold anisotropy was attributed to magnetocrystalline anisotropy, later analysis revealed that these effects are primarily caused by stress-induced anisotropy<sup>3</sup>. This led Kryder and Saunders<sup>4</sup> to propose that these anisotropic effects could be eliminated by growing garnet films with negative, equal magnetostriction coefficients,  $\lambda_{111} = \lambda_{100}$ . This is an additional requirement in the development of new high quality bubble materials.

A computer program was developed as a part of the materials research, to model various film compositions from a given set of user-defined needs and to estimate their physical properties. This greatly eased the film design and provided new film compositions, especially for sub-micron bubble diameter films and isotropic magnetostriction films. The computer program has a database of several Rare Earth and Transition Metal elements and the current models to estimate various parameters such as uniaxial anisotropy energy. Films grown using the

computer-aided design technique have been reasonably close to estimated design parameters and have been convenient starting points for eventual fine-tuning. The computer program has also been used to make several other garnet films for other purposes.

The LPE film growth furnace itself has been updated and modernized periodically with the ultimate aim of automating the whole growth operation using microprocessors for better and more uniform films.

This part of the report discusses the computer aided film/melt design, which is the starting point for all our bubble materials research, in Section II. Film growth technique is then described in Section III. This is followed by a section on Film Characterization (Section IV). Section V is on the bubble materials developed in our facility with an emphasis on the 0.5  $\mu\text{m}$ , isotropic magnetostriction materials. Magnetic bubble devices need to perform well over a wide ambient temperature range and some preliminary results of our temperature studies are presented in Section VI. Section VII concludes this discussion with a brief mention of work that is currently in progress, with a look at the projects to be undertaken in future.

## **Section II Computer Aided Film/Melt Design Program**

The computer aided film design system has been developed to quickly produce film compositions that will satisfy many criteria concurrently. By using the properties of the film constituents such as rare-earths, iron and iron dilutants, the program can extrapolate the hypothetical film properties. Lattice mismatch, magnetostriction coefficients, magnetization, damping and growth-induced and stress-induced anisotropies are calculated for any film composition from published data on standard compositions.

The magnetostriction coefficients ( $\lambda_{111}$  and  $\lambda_{100}$ ), magnetization( $4\pi M_s$ ) and the damping constant are calculated using the proportion of each of the rare earths and adjusting for the exchange (A) due to the tetrahedral-octahedral ion pairs. Each rare-earth has associated with it magnetization, damping and magnetostriction coefficients, so that the net value is the sum of the proportion of each constant. This net value is then decreased due to the exchange which is calculated from the iron dilution.

The lattice mismatch is similarly calculated, however the dilution of the iron sites must be carefully considered. Typical iron substituents such as gallium and germanium have been installed in the program by using a quadratic equation describing the lattice reaction to the dilutant incorporation. The quadratic describes the probability of the ions residing at a tetrahedral site [a smaller site resulting in expansive stress] or an octahedral site [a larger site resulting in a compressive stress]. The equations are derived from fitting published data to a plot and digitizing the resulting curve.

The growth-induced anisotropy is calculated using the pair ordering model of large ion-small ion interaction. A constant  $K_{ij}$  is assigned to each pair of rare-earths so that the net growth-induced anisotropy is the sum of each  $K_{ij}$  -rare-earth product. (i.e,  $K_G = K_{ij} X_Y X_{Lu}$  for Y-Lu pair). Anisotropy results from the pair ordering of Samarium and Europium with other rare-earths have correctly estimated published results. Using the lattice mismatch previously calculated, the stress-induced anisotropy is estimated and thus the total uniaxial anisotropy,  $K_u$ , is computed.

The inclusion of Bismuth in the films complicates the estimation of growth-induced anisotropy and the computer program produces mixed results. Bismuth appears not to behave as the pair-ordering model would suggest, but does have a large anisotropy. Bismuth incorporation into films is a sensitive function of growth temperature and additives to melt and thus a great variation of uniaxial anisotropy, more so than has been possible hitherto, is accomplished by just varying the growth parameters of the Bismuth melts.

In order to use the program, the user is required to specify the desired bubble diameter and  $Q$ . From these values, the values of  $A$ ,  $K_u$  and  $4\pi M_s$  can be determined from two standard bubble equations. First, the ratio of  $K_u$  to  $2\pi M_s^2$  is equal to  $Q$ .

$$K_u/2\pi M_s^2 = Q.$$

Secondly, the characteristic length,  $l$ , is directly related to the bubble diameter, the exchange constant  $A$ , the anisotropy constant  $K_u$  and the magnetization,  $4\pi M_s$ .

$$l = (\text{bubble diameter})/9 = 16 \pi (A K_u)^{1/2} / (4\pi M_s)^2.$$

Possible choice of constituents are picked, based on user's special needs (such as isotropic magnetostriction) and all compositions are scanned for possible useful compositions. Only those satisfying all requirements are retained and the ideal one is picked from this list.

The program is also capable of estimating physical properties of a particular film, given a film composition. This is especially useful in determining how the properties would change following melt alterations.

From the film composition, the melt composition is derived using the various segregation ratios that have been experimentally determined and reported in literature.

A typical output from using the computer program is shown in Table I and the best choice for an isotropic magnetostrictive film is shown by an asterik.

### Section III LPE Film Growth Technique

All garnet growth is accomplished by the standard vertical dipping method. The growth takes place in a three zone vertical furnace with the crucible containing the melt in the center of the middle zone. With our new furnace, the three zones are controlled individually by different temperature controllers, so as to enable independent variation of temperature in the different zones. This results in better control of temperature and better temperature profiles. An insulating sliding door assembly on top of the furnace reflects the furnace heat at the top, for efficient heating.

Two types of melt-flux systems are used in our laboratory; PbO-B<sub>2</sub>O<sub>3</sub> system and the new PbO-Bi<sub>2</sub>O<sub>3</sub> system. The melt constituents are weighed, mixed and packed into a platinum crucible. For the Bismuth melts, platinum crucibles with twice the normal wall thickness had to be used to withstand the corrosion due to the melt. The melt is dissolved in the appropriate flux system and the solution is superheated to above saturation temperatures ( $T_{\text{sat}}$ ) and allowed to homogenize for a minimum of 24 hours. It should be noted that in the Bismuth systems, Bi<sub>2</sub>O<sub>3</sub> plays the dual role of flux and film constituent.

The films are grown by decreasing the temperature of the melt to below  $T_{\text{sat}}$ . (typically around  $870^{\circ}\text{C}$ ) and lowering a  $\text{Gd}_3\text{Ga}_5\text{O}_{12}$  (GGG) substrate attached to a platinum substrate holder, rotating at 100 rpm, into the melt. The film will grow as long as the melt temperature is below  $T_{\text{sat}}$ . and the mismatch between the film and the substrate is not too great; typically less than 0.03 Å. The film is grown approximately  $0.2\text{ }\mu\text{m}$  thicker than the bubble diameter, thus for a  $1\text{ }\mu\text{m}$  diameter bubble film, the thickness would be around  $1.2\text{ }\mu\text{m}$ . Typical growth rates (depending on the supercooling and melt additives) are  $0.2\text{ }\mu\text{m}/\text{min}$  to  $1.0\text{ }\mu\text{m}/\text{min}$ , so that the growth times vary from 30 seconds to about 5 minutes. Films with  $0.5\text{ }\mu\text{m}$  bubble diameters, which are required to have a large Bismuth content are usually grown for short times. (around 30 seconds) After the film is grown, the substrate is raised above the melt surface and spun rapidly to get rid of excessive flux drops. Then the substrate holder is dismounted from the furnace and any remaining flux drops are dissolved.

A 40 % acetic acid, 10 % nitric acid and 50 % water solution proved effective for removing the  $\text{PbO-B}_2\text{O}_3$  flux from the substrate and the substrate holder. This flux solution was found to be insufficient when removing the  $\text{PbO-Bi}_2\text{O}_3$  flux used for growing the bismuth doped films. The flux removing solution was systematically altered to 40% acetic, 40% nitric and 20% water which proved to remove all of the remaining flux. During the flux removal procedure, the substrate, while mounted on the substrate holder, is alternately heated with a hot plate to  $90^{\circ}\text{C}$  and submerged in an ultrasonic bath.

Besides growing (111) films for device fabrication, several (100) films were also grown to measure their normal magnetostriction ( $\lambda_{100}$ ). The (100) films turned out to be relatively more difficult to grow due to greater adhesion of flux droplets to their surface.

#### Section IV Film Characterization Technique

The films grown are characterized for possible melt alteration as well as to provide data for device work. Every film grown has its thickness measured, while most have the characteristic length and magnetization measured. Sample films are further characterized for lattice mismatch, damping, gyromagnetic ratio, magnetostriction coefficients and  $H_k$ .

The thickness measurements are made optically from a reflectance trace of the film. Using the

interference of the light reflected from the bottom surface and the top surface of the film, a reflectance trace of the film is made by varying the wavelength of the incident light. This trace is then used with a graph of the index of refraction of the film as a function of the wavelength of light, to determine the thickness. The wavelength dependence of the index of refraction in turn is determined by measuring the thickness of a representative sample of a lot accurately, using the Transmission Electron Microscopy technique. An alternate method was employed in verifying the film thickness measurements in case of thick films (thickness  $> 5 \mu\text{m}$ ) and in deriving their index of refraction as a function of wavelength. A region of the film is etched part of the way (say, about  $2 \mu\text{m}$ ) and a surface profilometer is used to measure the difference in thicknesses between the etched and the unetched areas. This is compared to the corresponding value obtained using reflectometry trace in the etched and the unetched areas. Thus using reflectometry, thickness is measured in a fast, nondestructive manner. Typically, the thickness is measured at several points on the film surface to eliminate systematic errors and also to determine if there are surface imperfections such as mesas on the film.

Both the characteristic length,  $l$  and the magnetization ( $4\pi M_s$ ) are determined optically by domain observation under a polarizing microscope. Measurement of the domain stripe width, together with thickness can be used to determine  $l$ <sup>5</sup>. Magnetization is determined by measuring the perpendicular field that causes the bubbles to collapse and using the ratio of stripe width to film thickness. Published tables relate the ratios of stripe width and film thickness to the ratio of collapse field and magnetization and to the ratio of  $l$  and film thickness<sup>6</sup>.

Using Ferromagnetic Resonance, (FMR) we can calculate the gyromagnetic ratio, gilbert damping parameter, effective internal field (and thus the uniaxial anisotropy field) and the magnetostriction coefficients. The ferromagnetic resonance signals of the sample are found at various microwave frequencies and a graph of resonance frequency vs applied field is plotted. The slope of the curve for applied fields perpendicular to the sample, yields the gyromagnetic ratio. The intercept of the same curve, together with the value of magnetization, gives the uniaxial anisotropy field. The Gilbert damping parameter is related to the linewidth of the resonance signals. Furthermore, by applying a stress on the sample and thereby inducing a magnetostrictive energy, the FMR magnetic field is shifted to a different value. This shift is



related to the magnetostriction coefficients<sup>7</sup>. The resonance shift from the film on the back side of the substrate interferes with that of the epi-side and the backside of the film is therefore etched off prior to the measurement. Stress is applied on the sample mechanically by a vacuum applied on one side of the substrate. Under the present set-up, stress can only be applied normal to the sample and thus, (111) and (100) samples of the same composition are used to determine the respective  $\lambda$  constants. The magnetostriction coefficients are then used to evaluate the isotropicity of the samples.

The lattice mismatch is measured using a double crystal X-ray diffractometer. The X-rays penetrate approximately 4  $\mu\text{m}$  into the garnet, thus going through the film to the substrate. Peaks are observed at the two angles corresponding to the substrate's lattice spacing and the film's lattice spacing. The difference of the angles is measured and used to determine the lattice mismatch. Thickness can also be approximated from the relative intensities of the peaks.

## Section V Materials Development

In this section we review some of the materials developed in our magnetic bubbles facility. This section is intended to be a general overview and thus some materials are omitted from the discussion to keep it brief. Data from typical films discussed are shown in Table II.

Initially two submicron film compositions were developed. The first melt had the composition  $\text{Sm}_{0.65}\text{Gd}_{0.28}\text{Tm}_{1.0}\text{Y}_{0.8}\text{Lu}_{0.27}\text{Fe}_{4.8}\text{Ga}_{.2}$  with an  $l$  value of 0.056  $\mu\text{m}$  for a bubble diameter of 0.504  $\mu\text{m}$ .

The second melt, producing films of  $\text{Sm}_{1.2}\text{Lu}_{1.7}\text{Tm}_{0.1}(\text{FeGa})_5\text{O}_{12}$  was also developed for submicron bubbles. This melt required significant alterations including an addition of gallium and iron to adjust the characteristic length,  $l$ , from 0.08  $\mu\text{m}$  to 0.06  $\mu\text{m}$ . The films were grown with a super cooling of 20 ° C and a  $T_{\text{sat.}}$  of 880 ° C. These films have been shown to successfully demonstrate propagation of 0.5  $\mu\text{m}$  bubbles in 2  $\mu\text{m}$  period contiguous disk devices.

For useful contiguous disk devices, the magnetostriction coefficients must be negative and as large as possible. Most rare-earth ions have  $\lambda_{111}$  less than  $\lambda_{100}$ , so that a balancing ion with  $\lambda_{111}$  greater than  $\lambda_{100}$  must be used. Two such ions that were investigated were dysprosium<sup>8</sup>,

with  $\lambda_{111} = -5.90 \times 10^{-6}$  and  $\lambda_{100} = -12.60 \times 10^{-6}$  and bismuth with  $\lambda_{111} = 15.50 \times 10^{-6}$  and  $\lambda_{100} = +8.20 \times 10^{-6}$ . Thus dysprosium may be used without making the coefficients positive; however, dysprosium has a damping factor that is about forty times greater than the standard rare-earths. By using both dysprosium and bismuth together in a film, we are able to satisfy the isotropic magnetostriction requirements and have large negative magnetostriction coefficients and maintain a reasonable damping. Two sets of films were grown from two different flux based melts; the first melt was a dysprosium doped standard  $\text{PbO-B}_2\text{O}_3$  flux melt and the second was a bismuth  $\text{PbO-Bi}_2\text{O}_3$  flux melt.

The dysprosium film composition was  $\text{Sm}_{0.3}\text{Dy}_{1.6}\text{Gd}_{0.4}\text{Lu}_{0.7}(\text{FeGa})_5\text{O}_{12}$  which had magnetostriction coefficients of  $-2.8 \times 10^{-6}$  and a mismatch of less than 0.005 Å. Films grown from this melt were however found not too well suited for device work.

The second isotropic melt was based on the bismuth system. The incorporation of bismuth into the film has several advantages including an increase of optical contrast due to an increase of the Faraday rotation<sup>9</sup>, a secondary source of anisotropy and the correction of magnetostriction. Due to bismuth's positive magnetostriction coefficients, bismuth is used in small quantities as a correction to the magnetostriction. The greatest difficulty with using bismuth was that a new flux system must be developed employing  $\text{PbO-Bi}_2\text{O}_3$  instead of  $\text{PbO-B}_2\text{O}_3$ . We have had little previous experience and no success with this system prior to this series of films.

We have grown films doped with bismuth of the general composition<sup>10</sup>  $(\{\text{Dy Sm Lu Y Bi}\}_3[\text{FeGa}]_5\text{O}_{12})$ . The magnetization of these films turned out to be larger than desired ( $4\pi M_s = 1750$  G) and the bubble diameter at  $0.35 \mu\text{m}$ . The magnetostriction coefficients were reasonably good with  $\lambda_{100} = -4.6 \times 10^{-6}$  and  $\lambda_{111} = -1.8 \times 10^{-6}$ ; the fact that  $\lambda_{100}$  is more negative than  $\lambda_{111}$  shows that the melt is overcompensated for isotropic magnetostriction.

The AK series melt is an improvement over this melt. Series of films with  $\lambda$ 's, ranging all the way from undercompensated ( $\lambda_{111}$  more negative than  $\lambda_{100}$ ) to isotropic composition were grown, with plans for overcompensated films in the future. These have good device properties. Devices made from the  $0.5 \mu\text{m}$  films are discussed elsewhere in this report and the corresponding propagation margins and their temperature dependences etc. are also discussed therein.

AG and AH series melts were also bismuth melts for 1.0  $\mu\text{m}$  films. These are essentially used for current access device fabrication, which is also discussed elsewhere in this report. These contain the same constituents as the 0.5  $\mu\text{m}$  films but have different compositions. These too were designed to be isotropic and were found to be reasonably so.

A difficulty with bismuth films is the non-uniformity of the surface. This is due to the flux adhering to the film while being withdrawn from the melt letting the film continue to grow until the flux drops solidify. These flux drops result in a thicker film where the flux drops remain after withdrawal. Solving this problem was accomplished by adding Vanadium oxide to the melt so that the surface tension of the melt was increased while the melt viscosity was decreased<sup>11</sup>. Besides producing cleaner films, the addition of Vanadium also slowed the growth rates resulting in more uniform films. It has also been shown that addition of Vanadium increased the amount of bismuth incorporation into the films.

Films of the AF series are 1.0  $\mu\text{m}$  non-bismuth type with composition  $\{\text{Tm Sm Lu}\}_3[\text{FeGa}]_5(\text{O})_{12}$  and are used for fabricating devices using silicon on garnet technology, which too is described elsewhere in this report.

## Section VI Temperature Studies

In order to be useful in practical applications, these isotropic IICD devices must be able to perform in a wide range of ambient temperature. Bubble devices are designed to operate in the extended temperature range of  $-50^\circ\text{C}$  to  $+150^\circ\text{C}$ . The temperature dependence of the properties of the isotropic bubbles that are grown here are being studied currently and preliminary results are reported here.

The important bubble device parameters whose temperature dependences need to be studied are (1) Bubble collapse field,  $H_c$  (2) Bubble diameter and (3) isotropy,  $\lambda_{111} - \lambda_{100}$  to ensure isotropic propagation at all temperatures of operation. The bubble collapse and bubble diameter are measured by direct observation under a microscope, as mentioned earlier. To study the temperature effects, an experimental set-up as shown in Fig. 1 is used. The magnetic bias field is provided by a set of flat 'pancake' coils on which a thermoelectric heater is mounted. Thus the heating is localized at the sample with no associated problems of the magnet heating up. The

thermoelectric heater covered a reasonably wide range of temperature ( $\sim -20^{\circ}\text{C}$  to  $+120^{\circ}\text{C}$ ). For greater range of temperature, we plan to use an insulating chamber on top of the bias field assembly, enclosing the heater and to circulate temperature-controlled nitrogen gas (from evaporating liquid nitrogen). The decrease in the bubble collapse field with temperature in typical bubble films is designed to match the rate of decrease in the rate of decrease in the field values of most commercially available Barium ferrite permanent magnets, which is the source of the bias field. This is about 0.2 % per degree C, in the  $20 - 60^{\circ}\text{C}$  range. Preliminary data taken on a  $1.0\text{ }\mu\text{m}$  bubble film for  $H_c$  is shown in Fig. 2 and it is seen that  $H_c$  decreases at an almost similar rate. Such temperature studies are being currently carried out on  $0.5\text{ }\mu\text{m}$  samples and the data is not complete at present.

### Section VII Current and Future work

Currently, work is being done in several areas. On the film growth front, overcompensated films are being grown and devices grown on these films will be evaluated for their performance at room temperature and over a temperature range. Studies are also being carried out to see how the film properties, especially the magnetostriction coefficients, depend on the growth temperature.

Evaluating better temperature dependences is going to be taken up next. Instrumentation for measurement over a large temperature range is being planned. Plans are also being made to adapt the FMR set-up for temperature measurements so the magnetostriction coefficients can be evaluated as a function of temperature. The study of propagation margins as a function of frequency of the isotropic films will be taken up. Materials aspects of such parameters as gilbert damping parameter etc. will also be studied. Controlling and optimizing the various film growth parameters to yield the highest quality films will always be a part of any of our future endeavor.

## References

- <sup>1</sup> Y.S. Lin, G.S. Almasi, D.B. Dove, G.E. Keefe, and C.C. Shir, "Orientation dependence of propagation margin of 1- $\mu$ m bubble contiguous-disk devices -- Clues and Cures", *J. of Appl. Phys.*, 50, 2258, (1979).
- <sup>2</sup> R. Wolfe, T.J. Nelson, "Crystal Symmetry Effects in Ion-Implanted Propagation Patterns for Magnetic bubbles: 'Roof-Top' Designs", *I.E.E.E. Trans. Magnet.*, MAG-15, 1323, (1979).
- <sup>3</sup> A. Hubert, "Domain Wall Phenomenon in Bubble Propagation Layers", *J. of Magnetism and Magnetic Materials*, 35, 249, (1983).
- <sup>4</sup> M.H. Kryder, D.A. Saunders, "The Effects of Stress Relaxation and Anisotropic Magnetostriction On Charged Walls in Ion-Implanted Garnets", *I.E.E.E. Trans. Magnet.*, MAG-19, 1817, (1983).
- <sup>5</sup> A. H. Eschenfelder, *Magnetic Bubble Technology*, Springer-Verlag, New York, (1980).
- <sup>6</sup> D. C. Fowles and J. A. Copeland, *AIP Conf. Proc.* 5, 240, (1972).
- <sup>7</sup> X. Wang, C.S. Krafft, M.H. Kryder, "Measurement of Magnetocrystalline Anisotropy Field and Magnetostriction Coefficient in Garnet Films", *I.E.E.E. Trans. Magnet.*, MAG-18, 1295, (1982).
- <sup>8</sup> H. Makino, O. Okada, and Y. Hidaka, "Dysprosium Containing Bubble Garnet Composition for Ion-Implanted Contiguous Disk Devices", *J. Appl. Phys.*, 55, 2551, (1984).
- <sup>9</sup> P. Hansen, K. Witter, and W. Tolksdorf, "Magnetic and Magneto-optic Properties of Lead- and Bismuth-Substituted Yttrium Iron Garnet", *Phys. Rev.*, B27, 6608, (1983).
- <sup>10</sup> R. O. Campbell, Masters Thesis, Carnegie Mellon University, 1985.
- <sup>11</sup> Y. Hosoe, K. Andoh, T. Ikeda and R. Suzuki, "Reduction of Growth Rate-in Bi-substituted Bubble Garnets Using MoO<sub>3</sub> and V<sub>2</sub>O<sub>5</sub> Added Flux", *I.E.E.E. Trans. Magnet.*, MAG-22, 1290, (1986).

## List of Tables

<b>Table 1:</b>	Calculated Properties of $\{\text{DySmLuYBi}\}_3[\text{FeGa}]_5(\text{O})_{12}$ films with isotropic magnetostriction, bubble diameter, $0.5\ \mu\text{m}$ .	11
<b>Table 2:</b>	Typical film properties	13

Composition	$4\pi M_s$	$\Delta a_o$	$\lambda_{111}$	$\lambda_{100}$	$\lambda_{111}-\lambda_{100}$	$K_g$	$K_s$	$K_u$
	[G]	[Å]	[ $10^{-6}$ ]	[ $10^{-6}$ ]	[ $10^{-6}$ ]		[ $10^4 \text{ erg/cm}^3$ ]	
$\text{Bi}_{0.20}\text{Dy}_{1.00}\text{Sm}_{0.20}\text{Lu}_{0.90}\text{Y}_{0.70}\text{Fe}_{5.00}\text{Ga}_{0.00}\text{O}_{12}$	1340	0.001	-2.78	-3.00	0.22	6.4	0.14	6.5
$\text{Bi}_{0.30}\text{Dy}_{0.80}\text{Sm}_{0.20}\text{Lu}_{1.10}\text{Y}_{0.60}\text{Fe}_{4.90}\text{Ga}_{0.10}\text{O}_{12}$	1300	0.000	-1.85	-1.83	-0.02	8.4	0.01	8.4
$\text{Bi}_{0.40}\text{Dy}_{0.60}\text{Sm}_{0.20}\text{Lu}_{1.20}\text{Y}_{0.60}\text{Fe}_{4.80}\text{Ga}_{0.20}\text{O}_{12}$	1270	0.002	-1.00	-0.78	-0.23	10.2	0.06	10.2
$\text{Bi}_{0.40}\text{Dy}_{0.70}\text{Sm}_{0.20}\text{Lu}_{1.30}\text{Y}_{0.40}\text{Fe}_{4.84}\text{Ga}_{0.16}\text{O}_{12}^*$	1280	0.000	-1.13	-1.14	0.00	10.3	0.01	10.4
$\text{Bi}_{0.50}\text{Dy}_{0.60}\text{Sm}_{0.20}\text{Lu}_{1.50}\text{Y}_{0.20}\text{Fe}_{4.78}\text{Ga}_{0.22}\text{O}_{12}$	1260	0.001	-0.46	-0.48	0.02	12.3	0.01	12.3

**Table 1:** Calculated Properties of  $\{\text{DySmLuYBi}\}_3[\text{FeGa}]_5(\text{O})_{12}$  films with isotropic magnetostriction, bubble diameter,  $0.5 \mu\text{m}$ .

film number	h ( $\mu\text{m}$ )	l ( $\mu\text{m}$ )	$4\pi M_s$ (G)	Rate ( $\mu\text{m}/\text{min.}$ )	Temp. ( $^{\circ}\text{C}$ )
$\text{Sm}_{0.3}\text{Gd}_{0.4}\text{Tm}_{0.73}\text{Y}_{1.57}\text{Fe}_{4.4}\text{Ga}_{0.6}\text{O}_{12}$					
207	1.98	0.159	586	0.33	854
208	1.64	0.146	593	0.33	838
$\text{Sm}_{1.2}\text{Lu}_{1.7}\text{Tm}_{0.1}(\text{FeGa})_{5.0}\text{O}_{12}$					
AC21	1.21	0.064	1230	0.24	860
AC22	1.29	0.059	1134	0.26	868
$\text{Y}_{2.8}\text{La}_{0.2}\text{Fe}_{3.7}\text{Ga}_{1.3}\text{O}_{12}$					
AD03	1.20	---	---	0.20	860
AD41	3.20	0.144	220	0.32	880
$\{\text{Dy Sm Lu Y}\}_3\text{Fe}_5\text{O}_{12}$					
BA01	1.25	0.044	1765	0.25	885
BA03	1.40	0.0395	1730	0.47	863
$\{\text{Tm Sm Lu}\}_3[\text{FeGa}]_5\text{O}_{12}$					
AF23	1.096	0.138	668	0.254	833
AF26	1.50	0.1308	667	0.25	834
$\{\text{Sm Lu Bi Y Dy}\}_3[\text{FeGa}]_5\text{O}_{12}$ 1.0 $\mu\text{m}$ .					
AG42	0.839	0.228	353	0.606	903
AG43	1.349	0.144	438	1.614	875
$\{\text{Sm Lu Bi Y Dy}\}_3[\text{FeGa}]_5\text{O}_{12}$ 1.0 $\mu\text{m}$ .					
AH47	1.19	0.119	576	---	945
AH48	1.15	0.112	555	---	945
$\{\text{Sm Lu Bi Y Dy}\}_3[\text{FeGa}]_5\text{O}_{12}$ 0.5 $\mu\text{m}$ .					
AK51	0.82	0.0526	1077	1.89	871
AK53	0.77	0.0549	1125	2.01	868

Table 2: Typical film properties



**List of Figures**

- Figure 1:** Experimental set-up for temperature studies of  $H_c$ .
- Figure 2:**  $H_c$  vs Temperature for sample AH 39.

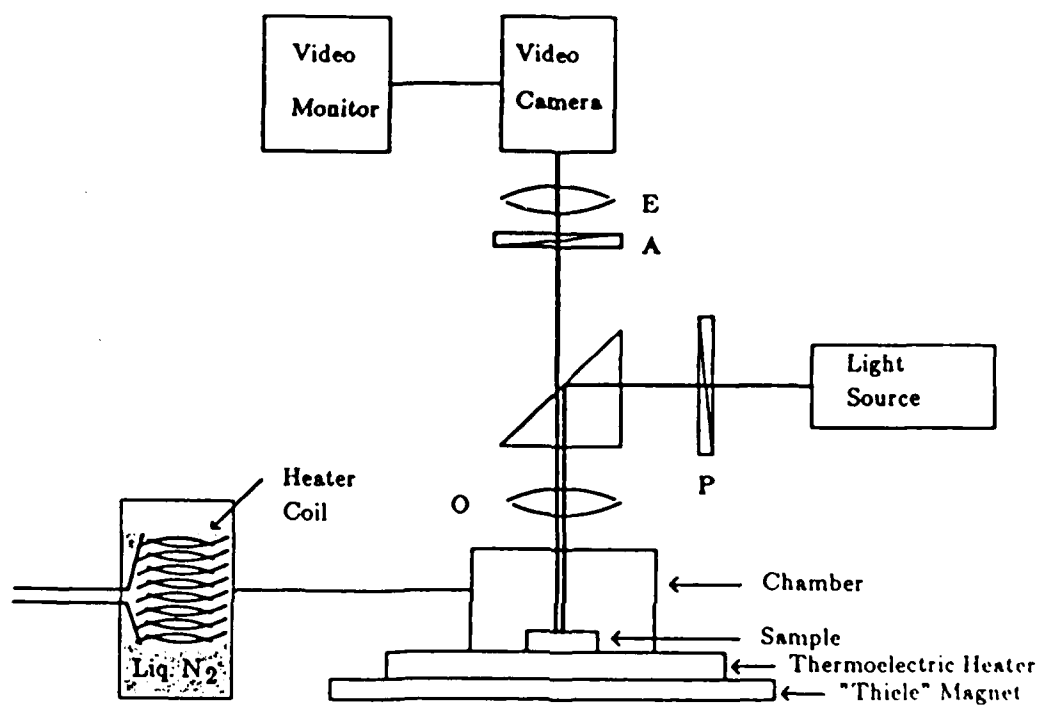


Figure 1: Experimental set-up for temperature studies of  $H_c$ .

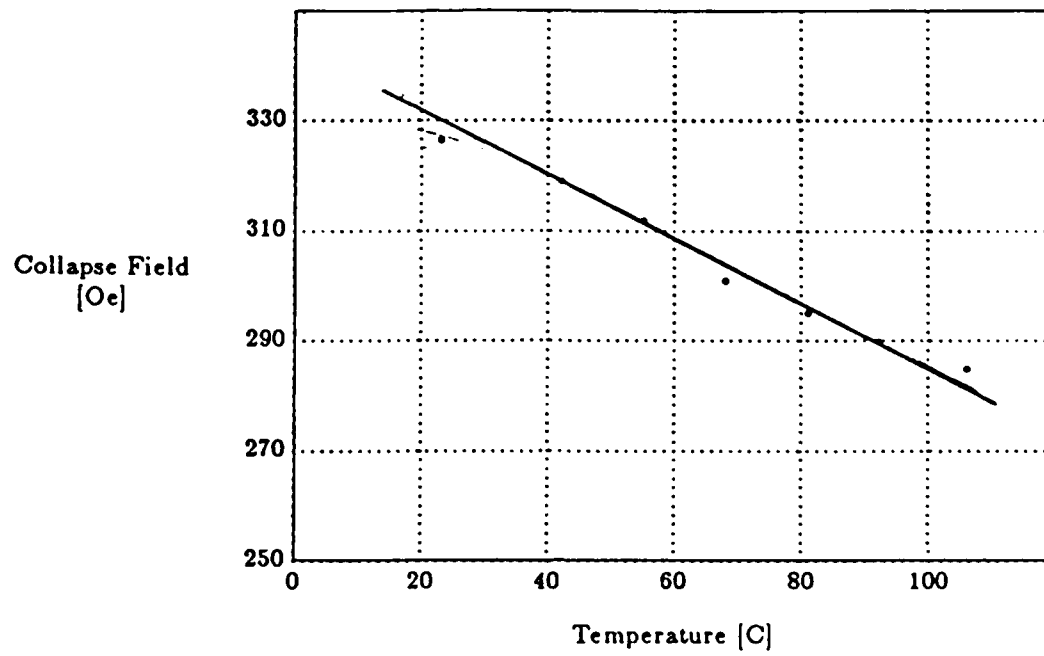


Figure 2:  $H_c$  vs Temperature for sample AH 39.

# Current-Access Ion-Implanted Magnetic Bubble Devices

Michael Alex and Mark H. Kryder  
Department of Electrical and Computer Engineering

## Abstract

A bubble propagation device based on the combination of ion-implanted devices and current-access devices is presented. Experimental results show that the potential well experienced by a bubble in these hybrid devices is greater than in either device alone. In addition, by utilizing the charged wall of the implanted structure the minimum drive current of the hybrid device is reduced by a factor of two when compared with the current-access device. A computer model used to calculate the enhanced well depth of the hybrid device accurately predicts the experimental results.

## Introduction

The current-access ion-implanted bubble device is a hybrid of two very different magnetic bubble propagation structures: the ion-implanted or contiguous disc device and the current-access or perforated sheet device. In this report the device is introduced and its method of operation is described. Computer simulations are performed comparing actual hybrid device data with that expected from the theory. There is excellent agreement between the experimental and computed results.

## The Device Structure

The current-accessed ion-implanted device structure is depicted in Fig. 1. It consists of a planar current sheet with a circular aperture; the area under the sheet is ion-implanted while in the aperture the magnetization remains normal to the film plane. Thus, except for the current sheet the device looks just like a basic contiguous disc propagation structure.

Current flow through the sheet has two effects. First, the in-plane magnetic field component produces charged walls at the positions shown in the figure. At these same positions potential wells due to the normal magnetic field component are created. Note

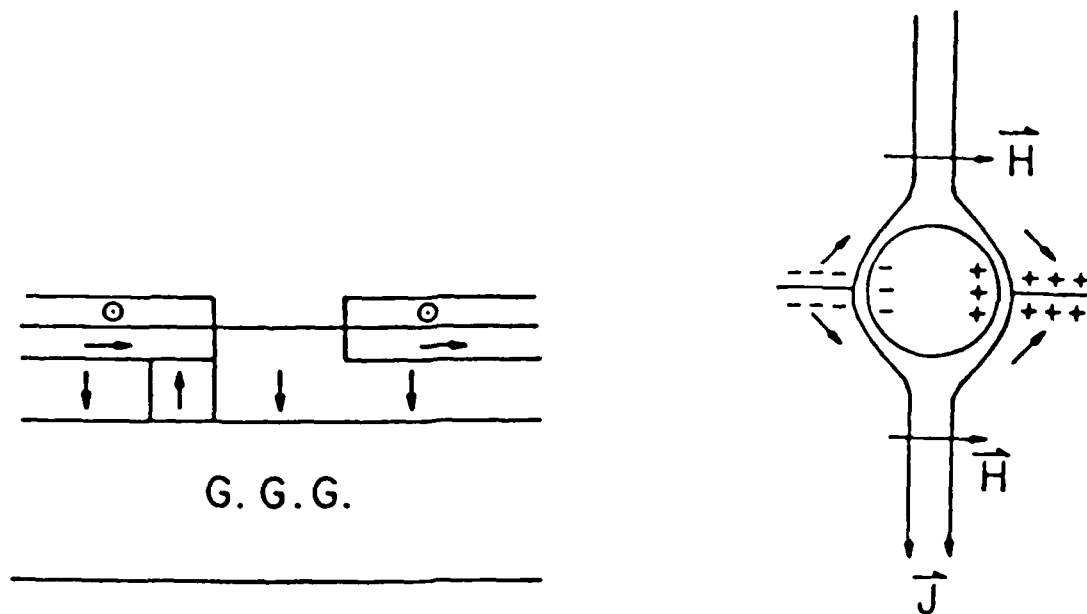


**Figure 1:** Cross-section and Top View of the Current-Access Ion-Implanted Bubble Device

that rotating the current will rotate the charged walls and the potential wells in phase with each other. In the figure a bubble is coupled to an attractive charged wall; this is also the location where the bias field is minimized, further enhancing bubble stability. Rotating the current in the film plane will result in the rotation of the bubble due to charged wall rotation as well as the bias field gradient in the same direction. The bubble, in essence, is driven independently by the two different mechanisms mentioned above.

One may measure the merits of each of these driving forces (the bias field gradient and the charged wall) by measuring the collapse field of a bubble as it is under the influence of each of these mechanisms. This measurement yields the "potential well" that the bubble experiences; the deeper the well the higher the collapse field and the more stable the bubble is. These measurements, as well as others, are presented in the next section.

### Experimental Results

In the work of Ohta and Kryder<sup>1</sup>, a  $1\mu\text{m}$  bubble was placed in the vicinity of an aperture with a radius of  $4\mu\text{m}$ . With a current density  $J$   $\text{mA}/\mu\text{m}$  flowing through the conductor, the bubble was attracted to the potential well as described above. The depth of the well was measured as a function of  $J$  by measuring the collapse field of the bubble at this location. The results are presented in Fig. 2. The collapse field increases linearly with increasing current density. At  $J = 0$ , the collapse field is 346 Oe. At a current density of  $2\text{mA}/\mu\text{m}$ , the collapse field increases to 356 Oe.

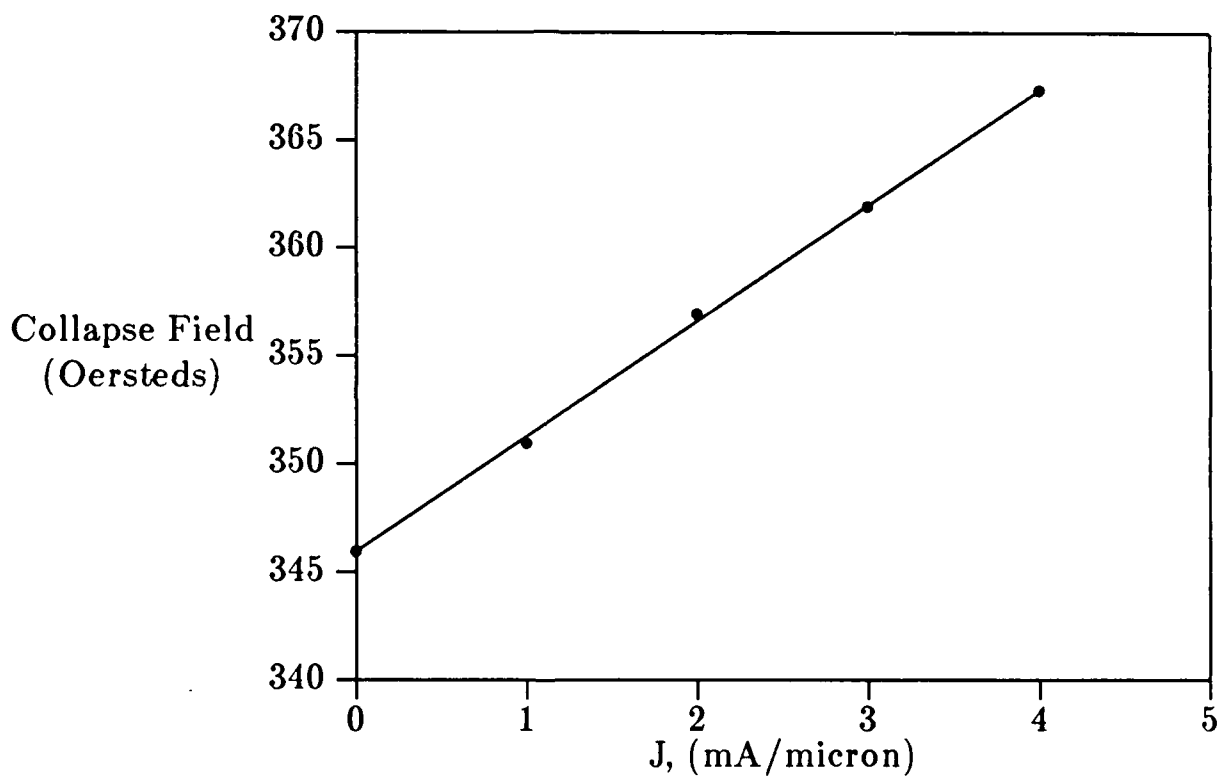


**Figure 2:** Bubble Collapse Field of Current Access Structure

For the ion-implanted structure, the bubble collapse field may be measured as a function of an applied in-plane field in order to obtain an estimate of the potential well

depth. For a bubble coupled to an unimplanted disc, there are "stable" and "unstable" bubble positions. Bubbles will reside at stable positions with no applied field; under the influence of an in-plane field however, the charged wall will stabilize a bubble at any position on the disc, even a previously unstable one. As seen in Fig. 3, the potential well characteristics of stable and unstable positions are different. For a bubble attached to the stable position, the collapse field decreases monotonically as the in-plane field increases. At the unstable position, the collapse field of the bubble increases, reaches a maximum and then decreases.

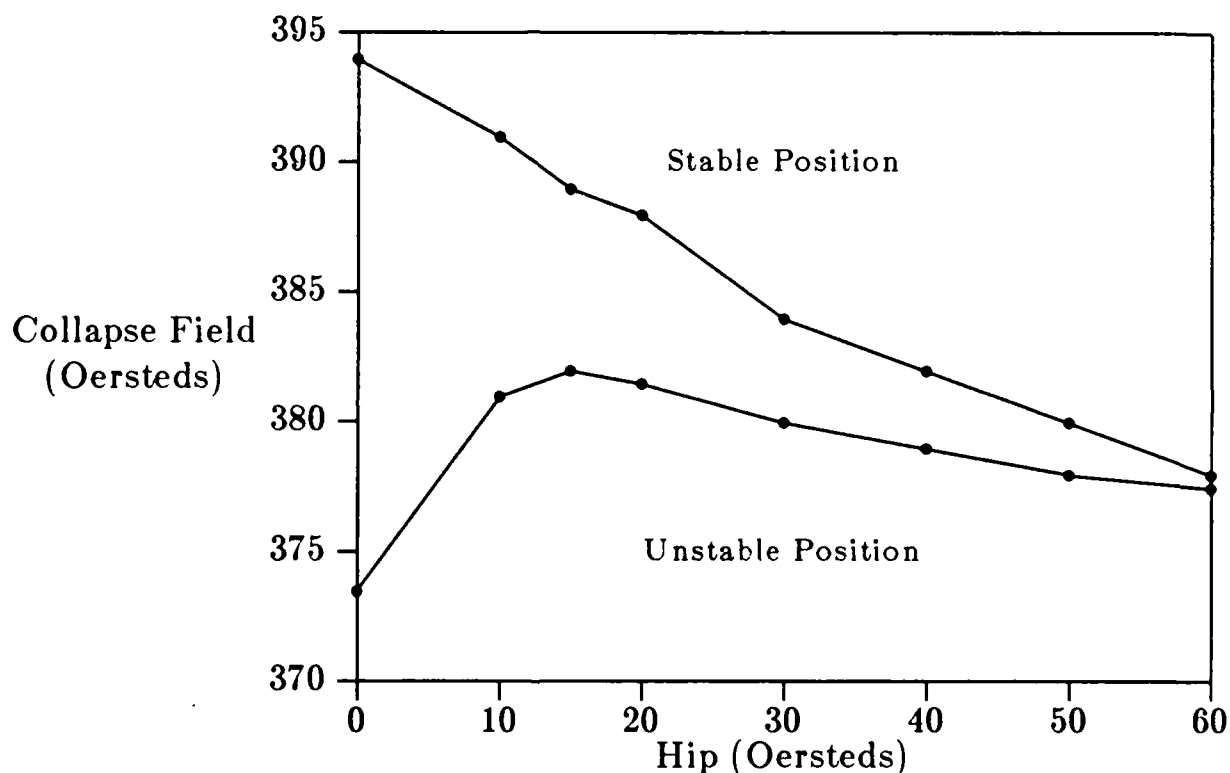


**Figure 3:** Bubble Collapse Field of Contiguous Disc Device Structure

Static characteristics of the ion-implanted current-accessed device are shown in Fig. 4. Recall that this device consists of an unimplanted disc underneath a current sheet

aperture of equal radius. As in the current-accessed device above, the collapse field of the bubble at a stable position was measured as a function of  $J$ , the current density through the sheet in  $\text{mA}/\mu\text{m}$ . As seen in the figure the collapse field at first increases linearly as in the current access device, and for current densities above  $2.5\text{mA}/\mu\text{m}$  decreases hysteretically.

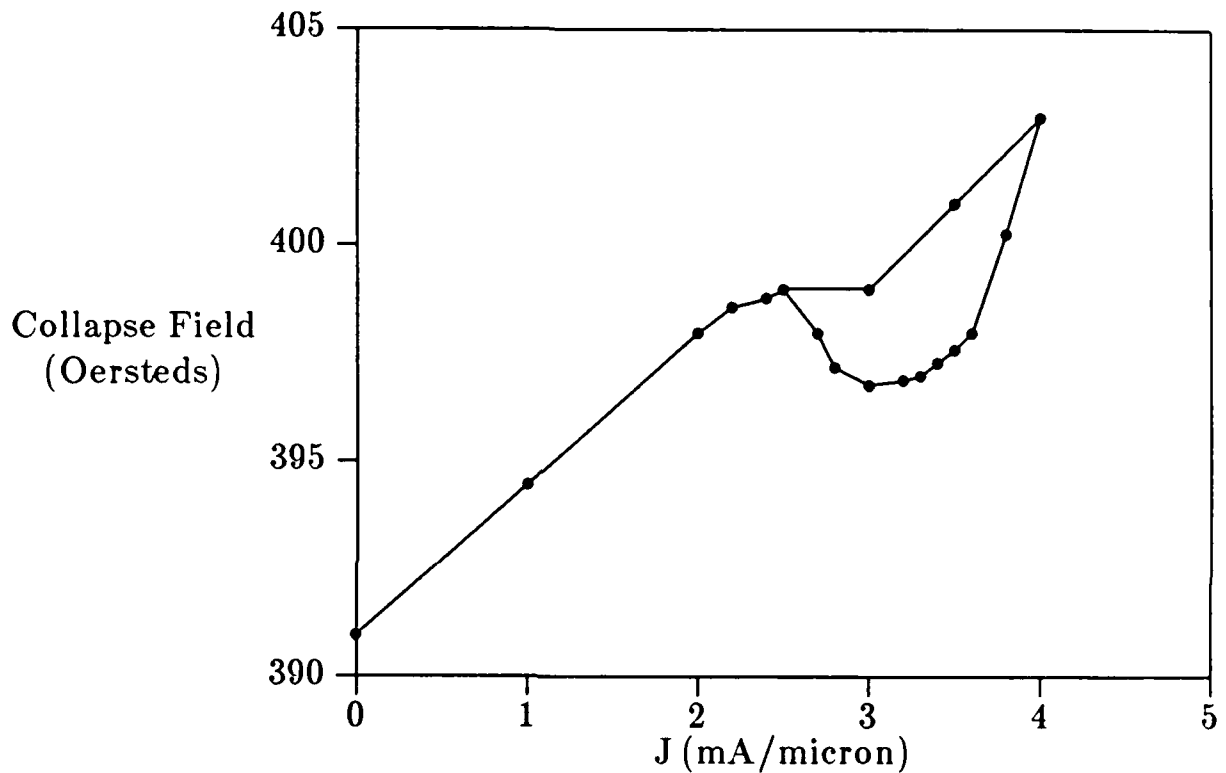


**Figure 4:** Bubble Collapse Field of Hybrid Device Structure

Another bubble device figure-of-merit and one that is pertinent for propagation structures is the bias field of circulation. In this experiment the bubble is circulated around an aperture at constant drive current and the bias fields at which the bubble strips out and collapses are measured. The better the device, the larger the range of bias fields expected. One would also like to minimize the drive current for circulation



at the same time. The bias field margins for circulation of a bubble around a  $6\mu\text{m}$  current-access aperture and a  $6\mu\text{m}$  hybrid device are seen in Fig. 5. Note that the hybrid structure has significantly better margins, and in particular, that the minimum drive current of the hybrid device is roughly one half that of the conventional current-access device. Since the power dissipation per unit device area is proportional to the square of the drive current, the hybrid device requires one quarter the power of the conventional structure.

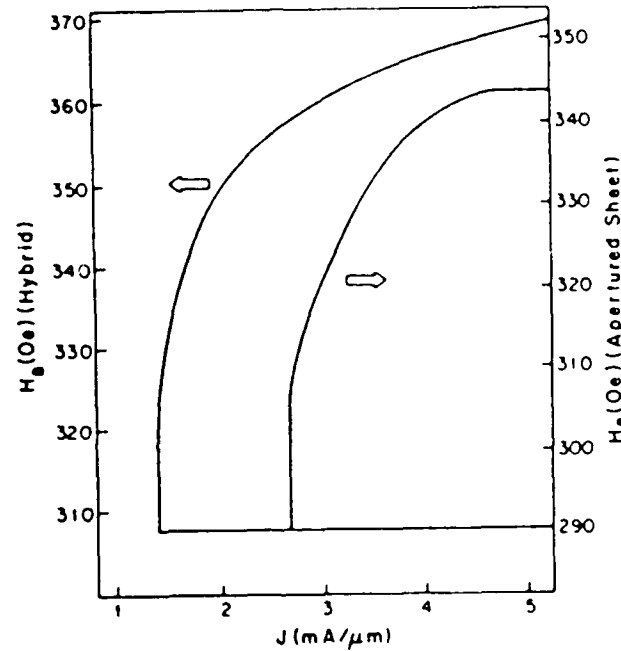


**Figure 5:** Current Access and Hybrid Device Circulation Margins

Finally, it should be noted that in the hybrid device, the drive field coils of conventional field-access devices have been eliminated. These coils are highly inductive and dissipate much power, especially at high frequencies. Through their elimination, these novel bubble devices will be capable of propagating bubbles at very high frequencies at low power consumption levels.

## Discussion

In this section computed fields and bubble behavior expected from these fields are presented and compared to the experimental results.

The simple current-accessed device will be discussed first. In the data of Fig. 2, it is seen that the bubble collapse field increases linearly with current density, as is to be expected. Using the geometry of the experimental device, magnetic fields were calculated and the perpendicular field component (which is responsible for the increase in bubble stability) was added to the bubble collapse field at  $J = 0$ . In other words the collapse field of the bubble in the current-access device,  $B_{c, cad}$  should be equal to the free bubble collapse field  $B_0$  (a constant) plus the perpendicular field from the current sheet aperture,  $B_p$ . The experimental and calculated results are shown in Fig. 6. Actually, in Fig. 6, the constant free bubble collapse field has been subtracted from the measured collapse field values of the current-access device; that is,  $\Delta B_0 = B_{c, cad} - B_0$ .

In the hybrid ion-implanted current-accessed device the situation is more complex. First, as has been demonstrated, is the fact that the perpendicular field increases the collapse field of a bubble as a linear function of current density. In the Experimental section, it was seen that for a bubble coupled to a charged wall in a stable position around an unimplanted disc the collapse field *decreases* as the in-plane field is increased. Thus, for the static case of a bubble in the stable position of the hybrid device, two competing effects are occurring as  $J$  is increased: 1) the perpendicular field component is increasing the potential well, and 2) the in-plane field component is decreasing the potential well. The net result is seen in Fig. 4.

One may calculate the expected potential well depth of the hybrid device (as a function of  $J$ ) by adding to the decreasing well depth of the ion-implanted structure the increasing well depth due to the perpendicular field component. In Fig. 7 is the net collapse field that results along with the previous experimental results. The computed result is actually the experimental bubble collapse field of the ion-implanted device that has been augmented by the perpendicular field component from the current sheet.

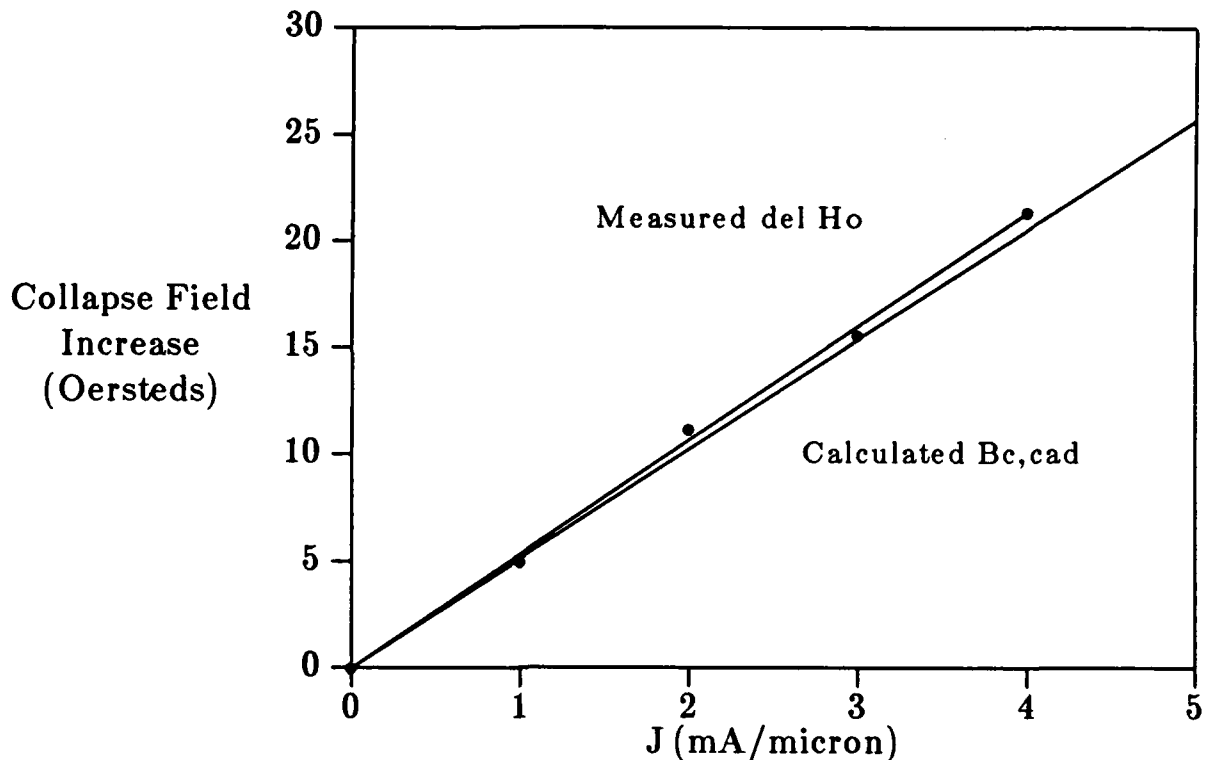


**Figure 6:** Calculated Perpendicular Field,  $B_z$ , and increase in bubble collapse field of the Current Access Device

### Present And Future Work

Although bubble circulation experiments indicate improved performance of the hybrid device over normal current-access devices, bubble propagation is required for practical memories. Thus, the concept of the hybrid aperture has been extended to the design of bubble propagators that behave much like contiguous disc devices but are driven by perforated current sheets. A typical design is seen in Fig. 8. Mask sets have been designed and written in order to fabricate these devices; device processing has been completed and at the time of this writing propagation structures are in the preliminary stages of testing. A mask set includes the ion-implanted level, perforated conductor levels as well as a bubble nucleator level. In addition, ion-implantation conditions have been established by measuring propagation margins of contiguous disc device structures.

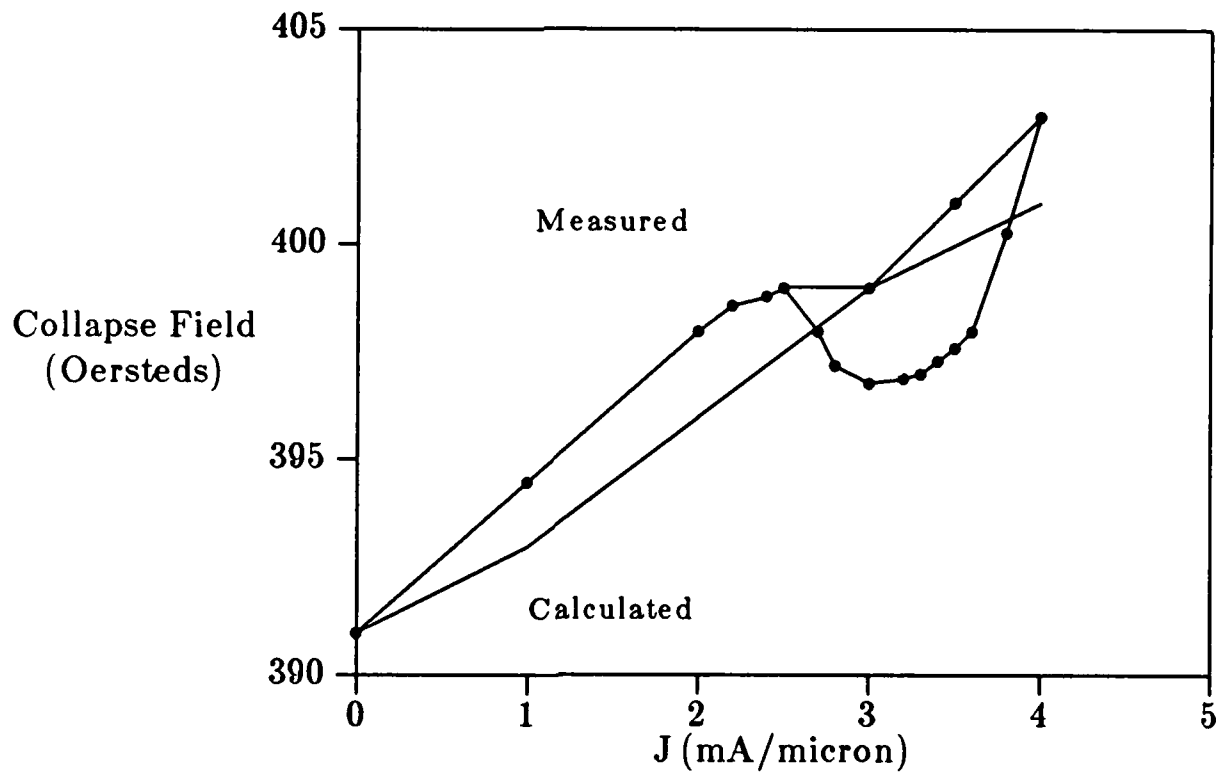


**Figure 7:** Calculated and Experimental Bubble Collapse Fields of the Hybrid Device.

The field calculations have been modified to include the influence of adjacent apertures, an important effect when the apertures get close, as in small bubble or high density configurations. For example, in Fig. 9 is seen the perpendicular magnetic field at the edge of an aperture of radius  $r$  as a function of angular position,  $\phi$  (in radians), around the aperture with center-to-center spacing of an approaching aperture,  $r_{ij}$  as a parameter. In this figure, the values of  $r_{ij}$  are  $2.5r$ ,  $3.0r$ ,  $4.0r$ ,  $10.0r$  and  $50.0r$ . The magnetic field has been normalized to  $2\pi$ . One can see that at  $r_{ij} = 2.5r$  the sign of the potential well changes polarity and that two "satellite" wells are formed. The implications of this effect as well as other aspects of the device and its structure are presently being studied.

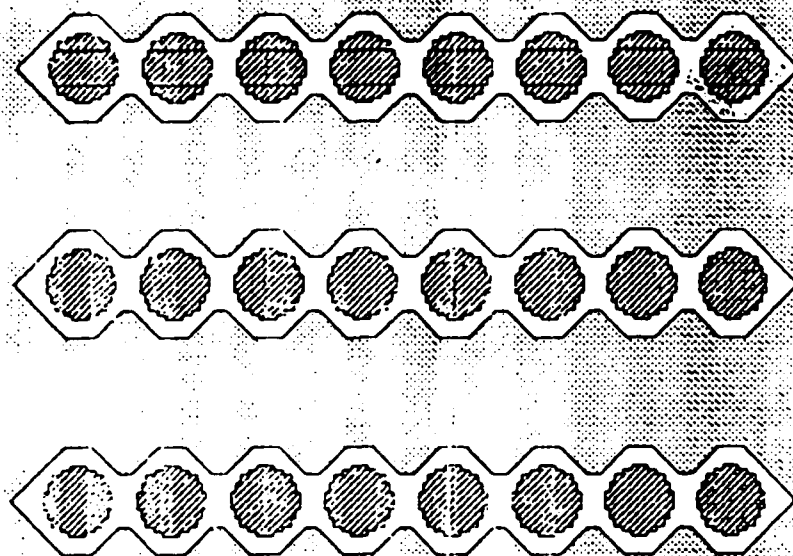


Figure 8: A Hybrid Device Propagation Structure

### Device Simulation

In order to build a foundation for modelling and simulation of bubble motion in propagation structures, the model of Calhoun was utilized as a starting point.<sup>7</sup> In his work, Calhoun simulated the motion of a bubble driven by a charged wall circulating about an unimplanted disc. A schematic of the situation is depicted in Fig. 10. Several assumptions are used to simplify the analysis. It is assumed that the bubble and charged wall are rigidly coupled and that all the damping of the moving charged wall/bubble system is due to the bubble. Experiments have borne out the latter assumption to be correct.<sup>9</sup> The damping force of the bubble may be approximated as

$$F_d = \pi d M_s t_s (R/\mu_w) d\theta/dt, \quad 1$$

where  $\mu_w$  is the wall mobility of the storage layer,  $t_s$  is the storage layer thickness,  $M_s$

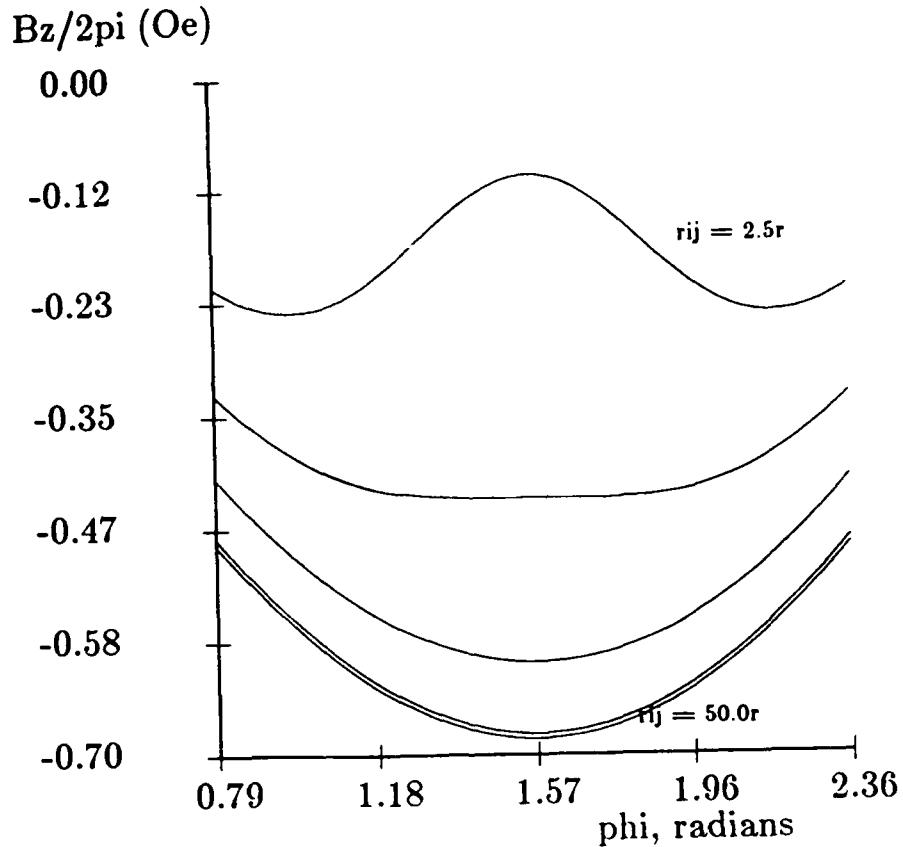


**Figure 9:** The effects of aperture separation on the perpendicular magnetic field of an aperture of radius  $r$ . The values of  $r_{ij}$  shown are  $2.5r$ ,  $3.0r$ ,  $4.0r$ ,  $4.0r$ ,  $10.0r$  and  $50.0r$ .  $\phi$  is the angular position around the aperture in radians. The current is incident at  $\phi = 0$ .

is the magnetization of the storage layer,  $R$  is the radius of the bubble trajectory and  $d$  is the bubble diameter.

The bubble/charged wall is driven around the disc by the applied field,  $H_{xy}$ . To first order, we may approximate the charged wall as a sheet of length  $L$ , height  $t_d$ , the thickness of the ion-implanted drive layer, having a uniform charge density  $\rho = 2M_d \cos \alpha$ , where  $\alpha$  is the angle between the wall normal and  $M_d$ , the drive layer magnetization. Then, the force due to  $H_{xy}$  driving the wall  $F_H$  may be given by:

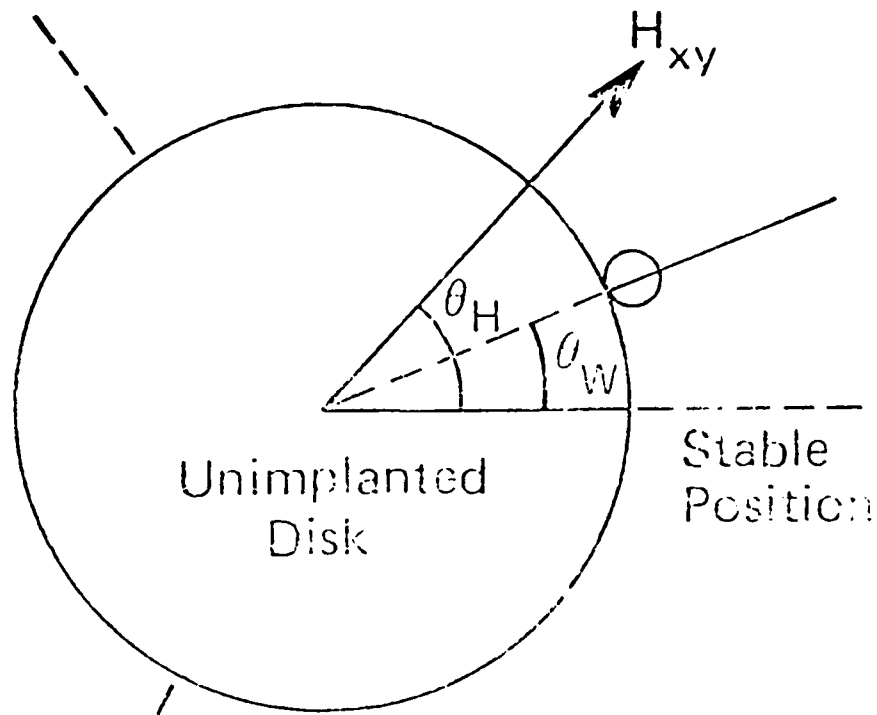


**Figure 10:** Charged wall/bubble circulating about an unimplanted disc.

$$F_H = (2M_d t_d L \cos \alpha) H_{xy} \sin(\theta_H - \theta_w)$$

2

where  $\theta_H$  is the angle of the applied field and  $\theta_w$  is the angular position of the wall and bubble.

In ion-implanted devices of the type described here, crystalline and stress-induced anisotropies play major roles in affecting charged wall behavior. The major component, the stress-induced anisotropy, has the same angular dependence as the crystalline anisotropy and is proportional to  $\sin 3\theta_w$ . The form of these anisotropies gives rise to the three "easy" and "hard" directions of these devices; the charged wall will prefer to reside at  $\theta = 0^\circ, 120^\circ$  or  $240^\circ$ . The restoring force is then given as:

$$F_r = (2M_d t_d L \cos \alpha) (H_{\text{eff}}/3) \sin 3\theta_w,$$

3

where  $H_{\text{eff}}$ , the effective anisotropy field due to crystal symmetry and stress relaxation is:

$$H_{\text{eff}} = 9\sqrt{2}[(1/3)K_1 + (\lambda_{111} - \lambda_{100})(\sigma_n - \sigma_p)]H_B / [(Q_d - 1)4\pi M^2], \quad 4$$

where  $Q_d$  is the quality factor of the implanted layer,  $H_B$  is the applied bias field, the  $\lambda$ 's are the appropriate magnetostriction constants and  $\sigma_n$  and  $\sigma_p$  are the stress components normal and parallel to the implanted edge respectively. Note that for equal magnetostriction constants there is no contribution to the anisotropy field due to magnetostriction.

By equating the driving force with the restoring and damping force,  $F_d + F_r = F_H$ , we get the following first order non-linear differential equation:

$$v \, d\theta/d\omega t + 1/3 \sin 3\theta = h \sin(\omega t - \theta), \quad 5$$

where  $h = H_{xy}/H_{\text{eff}}$ ,  $v = R\omega/\mu_e$ ,  $\theta_H = \omega t$  and  $\mu_e = \mu(2M_d t_d L \cos \alpha) / \pi d M_s t_s$ .

A computer program was written to solve the equation of motion by the Runge-Kutta method.<sup>10</sup> Two useful results obtained are 1), the position of the charged wall/bubble as a function of the in-plane field position, and 2), the phase lag between the drive field and the charged wall/bubble. In addition, the effects of drive field magnitude, stress and magnetostriction constants, operating frequency and dynamic bubble parameters on bubble circulation may be modelled.

In Fig. 11 is seen the bubble position around an unimplanted disc for two different values of the normalized in-plane field. Note that as the in-plane field is increased, the bubble follows the field more closely. This is seen more graphically in Fig. 12. which depicts the phase lag between the circulating bubble and the rotating in-plane field. For very high drive field values, the phase lag is virtually eliminated, as is seen in the laboratory.

It is interesting to see the effects on bubble motion due to having a material which is isotropic, that is the effects of the crystalline anisotropy and anisotropic magnetostrictive effect essentially neutralize each other. Referring back to equation 4



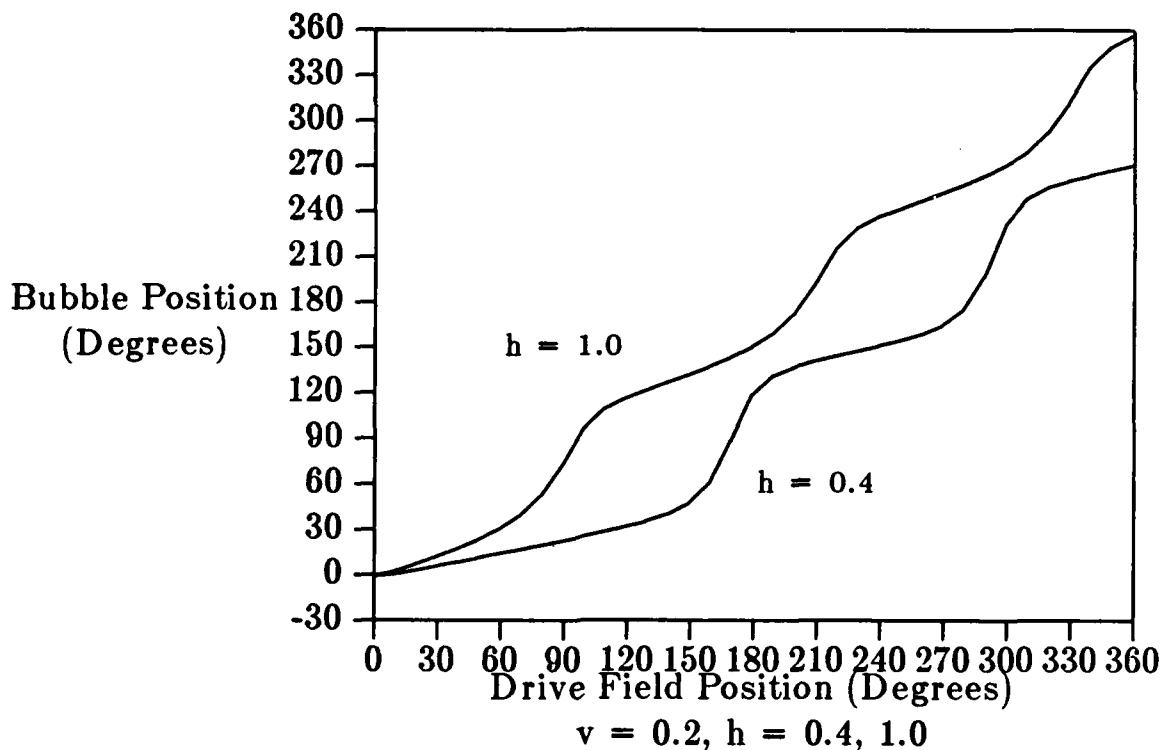


**Figure 11:** Bubble position as a function of drive field position around an unimplanted disc for two different values of the normalized drive field,  $h$ .

above, it is seen that a judicious selection of the magnetostriction coefficients,  $\lambda_{111}$  and  $\lambda_{100}$ , as well as knowledge of the stress distribution around the unimplanted disc can yield  $H_{\text{eff}} = 0$ . The simulated motion of a bubble in this case is depicted in Fig. 13 for two values of the normalized drive field,  $h$ . There is still a slight phase lag but it is constant, and the bubble's angular velocity, the derivative of the bubble position with respect to time, is also constant. This is certainly required for improved device operation and gives greater flexibility to the device designer who will not be restricted to limited propagation track geometries and orientations because of anisotropic bubble behavior.

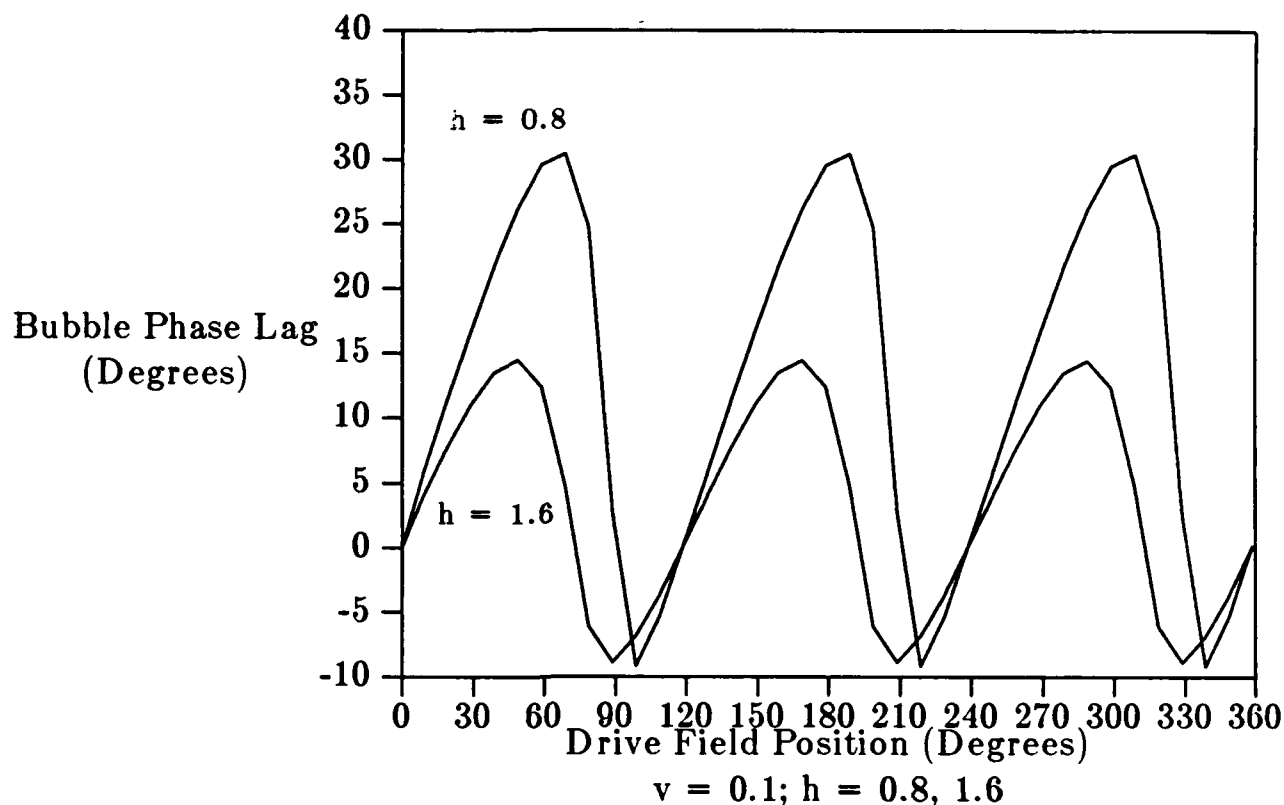


**Figure 12:** The phase lag between the drive field and circulating bubble for two different values of the normalized drive field,  $h$ .

Presently, the model described in this section is being modified to take into account other forces on the bubble, such as those induced by current carrying conductors. In this way, the current-access ion-implanted device described in the previous section may be modelled. Recall that the computer simulations of the previous section were basically for the *static* characteristics of the hybrid device, such as the bubble collapse field. However, with the model introduced in this section, we may predict bubble motion in the hybrid structure as was done for the ion-implanted device:

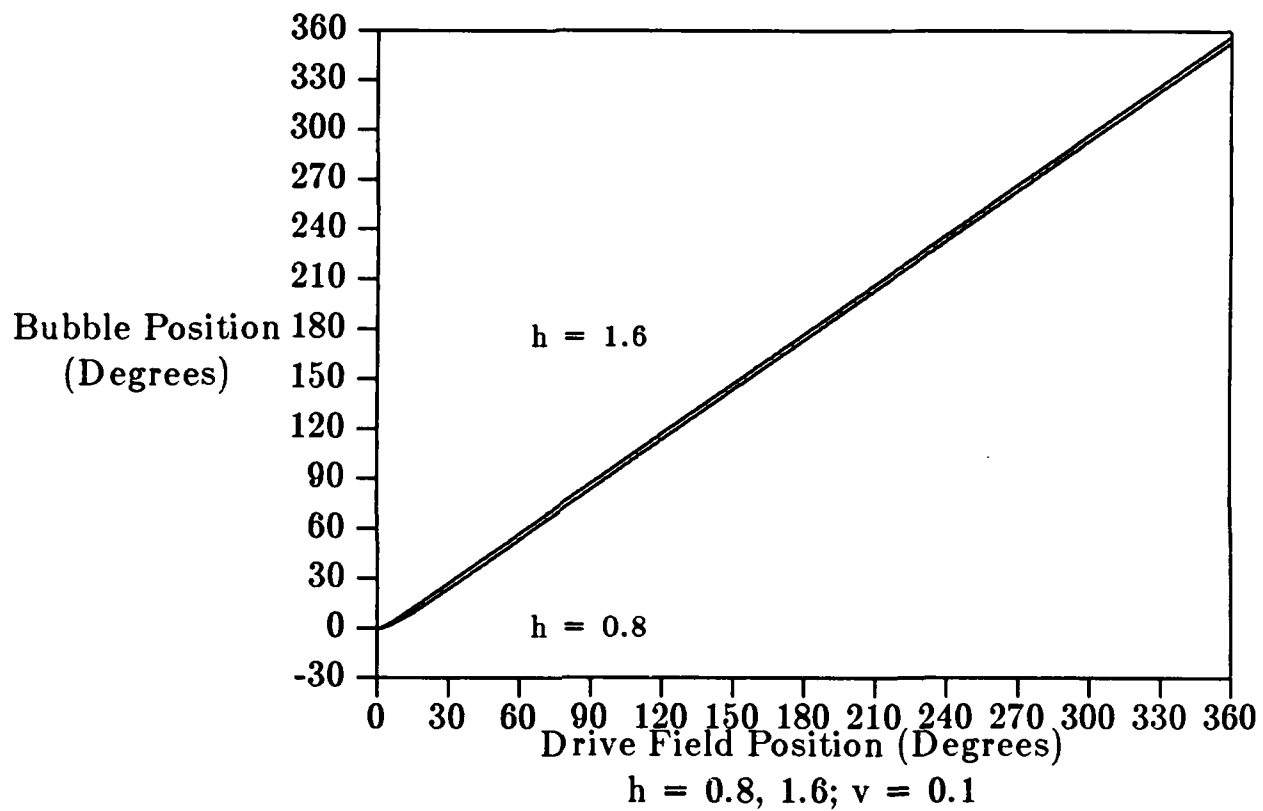


**Figure 13:** Bubble position as a function of drive field position around an unimplanted disc for two different values of the normalized drive field,  $h$  assuming an isotropic material.

## References

1. Ohta, H. and Kryder, M.H. "Current-access ion-implanted bubble device structure", *J. Appl. Phys.*, **53** (3), March 1982, pp. 2531-2533
2. Walsh, T. *Magnetic Bubble Propagation Using Distributed Electric Currents* Ph.D. Dissertation, Carnegie Mellon University, 1975
3. Walsh, T. and Charap, S.H. "Novel Bubble Drive", *A.I.P. Conference Proceedings*, No. 24, 1974 pp. 550-551
4. Bobeck, A.H., Blank, S.L., Butherus, A.D., Ciak, F.J., and Strauss, W. "Current Access Magnetic Bubble Circuits", *The Bell System Technical Journal*, Vol. 58, No. 6, July-August 1979
5. Copeland, J.A., Elward, J.P., Johnson, W.A. and Ruch, J.G. "Single-Conductor Magnetic Bubble Propagation Circuits", *J. Appl. Phys.*, Vol. 42, No. 4, March 1971, pp. 1266-1267
6. Keister, B.D. and Smith, R.L. "A Multiple Scattering Theory for Current-Access Magnetic Bubbles" To be published
7. Calhoun, B.A. *IEEE Trans. Magn.*, MAG-18, 1373-1375 (1982)
8. Keezer, D.C. Thesis, Carnegie Mellon University, (1983)
9. Argyle, B.E., Kryder, M.H., Mundie, R.E. and Slonczewski, J.C. *IEEE Trans. Magn.*, MAG-14, 593 (1978)
10. Greenberg, Michael D. in *Foundations of Applied Mathematics* Prentice-Hall Englewood Cliffs, NJ (1978)

## List of Figures

<b>Figure 1:</b>	Cross-section and Top View of the Current-Access Ion-Implanted Bubble Device	1
<b>Figure 2:</b>	Bubble Collapse Field of Current Access Structure	2
<b>Figure 3:</b>	Bubble Collapse Field of Contiguous Disc Device Structure	3
<b>Figure 4:</b>	Bubble Collapse Field of Hybrid Device Structure	4
<b>Figure 5:</b>	Current Access and Hybrid Device Circulation Margins	5
<b>Figure 6:</b>	Calculated Perpendicular Field, $B_z$ , and increase in bubble collapse field of the Current Access Device	7
<b>Figure 7:</b>	Calculated and Experimental Bubble Collapse Fields of the Hybrid Device.	8
<b>Figure 8:</b>	A Hybrid Device Propagation Structure	9
<b>Figure 9:</b>	The effects of aperture separation on the perpendicular magnetic field of an aperture of radius $r$ . The values of $r_{ij}$ shown are $2.5r$ , $3.0r$ , $4.0r$ , $4.0r$ , $10.0r$ and $50.0r$ . $\Phi$ is the angular position around the aperture in radians. The current is incident at $\Phi = 0$ .	10
<b>Figure 10:</b>	Charged wall/bubble circulating about an unimplanted disc.	11
<b>Figure 11:</b>	Bubble position as a function of drive field position around an unimplanted disc for two different values of the normalized drive field, $h$ .	13
<b>Figure 12:</b>	The phase lag between the drive field and circulating bubble for two different values of the normalized drive field, $h$ .	14
<b>Figure 13:</b>	Bubble position as a function of drive field position around an unimplanted disc for two different values of the normalized drive field, $h$ assuming an isotropic material.	15

INTEGRATION OF SEMICONDUCTOR  
AND  
MAGNETIC BUBBLE DEVICES: SOI ON GARNET

D.W. GREVE, M.H. KRYDER, AND P.H.L. RASKY  
Carnegie-Mellon University, Dept. of Electrical and Computer Engineering,  
Schenley Park, Pittsburgh, PA 15213

ABSTRACT

Silicon on insulator (SOI) technology makes it possible to fabricate semiconductor devices on foreign substrates. In this paper, we present results for a process in which field effect transistors are fabricated in recrystallized polysilicon on a magnetic bubble substrate. We report on the characteristics of the field effect transistors and the effect of the necessary processing steps on the magnetic properties of the substrate. A memory constructed in this hybrid technology would have very high density, multiple detectors for high speed, and direct logic level outputs.

INTRODUCTION

Fabrication of semiconductor devices on the same substrate as magnetic bubble memory structures offers a number of potential advantages. In current production technology, bubbles are detected by a magnetoresistive detector which occupies a considerable fraction of the chip area (~5%). The access time is limited by the rate at which bubbles can be moved past this detector. Unlike semiconductor memories, parallel outputs are not practical because of the large area required for each detector. In addition, the sensitivity of the detector is low resulting in the need for sensitive off-chip amplifier circuitry [1,2].

Bubble memories have the advantages of nonvolatility and relative immunity to environmental stresses. We are working to improve the performance of magnetic bubble memories by replacing magnetoresistive detectors with semiconductor detectors which are smaller and more sensitive. In addition, we believe that on-chip amplifiers can be produced which will drive loads at standard logic levels. We therefore seek to fabricate working semiconductor devices on bubble substrates without damaging the magnetic properties of the substrate underneath.

In our present technology, laser recrystallization is used to convert small grain polysilicon into large grain material which can then be used to make MOSFETs and magnetic detectors. To date, we have demonstrated

operating MOSFETs although problems with yield and device quality still need to be solved. The major problems in such a technology concern changes to the bubble substrate during the thermal processing necessary for MOSFET fabrication and contamination of the semiconductor devices by impurities from the bubble substrate. We note that similar problems of contamination and substrate damage are encountered in other thin film transistor technologies.

In the following, we first illustrate a possible structure integrating bubble propagation patterns and semiconductor detectors. We then explore the feasibility of fabricating such a structure. First, studies of the effect of various annealing treatments and depositions on the properties of bubble films are reported. We then discuss the characteristics of semiconductor devices which we have fabricated on bubble substrates.

#### INTEGRATED DETECTOR AND PROPAGATION PATTERN

In this section, we describe a possible design for a semiconductor detector integrated with bubble propagation patterns. Semiconductor magnetic field detectors fit best into modern bubble memory fabrication processes using ion-implanted propagation patterns. As an example, consider the design for an integrated detector and propagation pattern shown in Fig. 1. The detector used in this design is a magnetodiode; the high sensitivity of this type of detector, with 5-80 volts/Tesla values reported [3,4], makes this device a natural candidate for bubble detectors. In this design, magnetic bubbles move along the bubble propagation pattern in response to a rotating external magnetic field until they reach the hairpin stretcher. The hairpin stretcher is then activated by applying a large current pulse of 100- 200 mA, causing the effective bias field in the ion-implanted channel to be lowered. If a bubble is present when this occurs, the bubble will expand into the channel. The in-plane component of the bubble's magnetic field is sensed by the nearby magnetodiode.

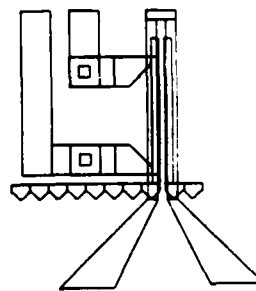


Fig. 1: Top view of a silicon on garnet magnetodiode with integrated bubble propagation pattern.

It is difficult to make an estimate of the sensitivity of this design. Since the magnetodiode responds to the in-plane component of the magnetic field, the signal produced by a bubble is expected to be a strong function of the separation between the detector and the ion-implanted channel and also the thickness of the spacer layer. However, the high sensitivity of the magnetodiode makes it likely that the signals will be substantially larger than present magnetoresistive detectors.

We have also considered other designs using multiple drain MOSFET detectors [5]. The sensitivity of this detector is lower than a magnetodiode, but use of a dummy detector is not required since the MOSFET detector responds only to the perpendicular component of the magnetic field. All of these designs require that the semiconductor film be adequate for fabrication of MOSFETs and that the bubble film be undamaged during the fabrication process. In the following sections, we describe experiments which address these issues.

#### ANNEALING STUDIES

Figure 2 shows a MOSFET fabricated in our silicon on garnet technology. Major thermal steps required for fabrication include the polysilicon deposition (625 °C), laser recrystallization (1415 °C in polysilicon), and gate oxide growth and implant diffusion (850 °C). In order to establish the feasibility of fabricating semiconductor devices, we conducted a series of annealing studies [6].

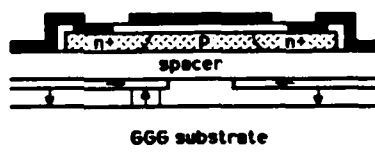


Fig. 2: Cross section of a silicon on garnet MOSFET.

Briefly, we found that essentially no change in the properties of the bubble film occurred during annealing in an oxygen environment at 1000 °C or less for 30 minutes. Polysilicon deposition on a 1  $\mu\text{m}$  sputtered  $\text{SiO}_2$  layer caused changes in magnetic properties for some film compositions but not for others. When the more stable film composition was used, recrystallization of the polysilicon film resulted in changes which were reversible by subsequent oxygen annealing. It was therefore reasonable to expect that appropriate choice of the film composition would allow fabrication of MOSFETs without damaging the substrate.

Attempts to fabricate such transistors, however, revealed other



problems. Although operating transistors were obtained with the process described above, the yield was poor and the devices suffered from high gate leakage and low channel mobility. Comparison with devices fabricated in the same run on silicon substrates showed that contamination from the substrate or spacer layer was probably responsible [7].

We therefore conducted additional studies to explore the possibility of using other spacer layers which would act as barriers to the metal ions in the bubble film. Silicon nitride is an obvious choice. We have studied the possibility of using plasma (~25 °C) and LPCVD (~800 °C) silicon nitride.

We first tried LPCVD (low pressure chemical vapor deposited) silicon nitride since this material has been used in oxide isolation processes as an oxygen diffusion barrier [8]. The depositions were done by reacting silane and ammonia at 800 °C.

Our first depositions were on films with the composition  $\text{Y}_{0.6}\text{Sm}_{0.3}\text{Tm}_{1.3}\text{Gd}_{0.6}\text{Fe}_{4.6}\text{Al}_{0.2}\text{Ga}_{0.2}\text{O}_{12}$ . Attempts to deposit silicon nitride directly on the bubble substrate were unsuccessful. A black deposit was observed on the bubble film although visually good films were obtained on silicon wafers in the same run. A subsequent experiment showed that a hazy deposit on the surface resulted from an anneal at 800 °C in ammonia gas alone. Auger spectra showed a high concentration of iron at the surface after annealing suggesting that diffusion to the surface had taken place.

We next tried a two step process in which 9000 Å LPCVD  $\text{SiO}_2$  was deposited first followed by deposition of 8500 Å of silicon nitride. The  $\text{SiO}_2$  film was deposited by the reaction of silane and nitrous oxide at 860 °C and the bubble films had the compositions  $\text{Sm}_x\text{Tm}_y\text{Lu}_{3-(x+y)}\text{Ga}_2\text{Fe}_{5-2}\text{O}_{12}$ . Results are shown in Table I where the saturation magnetization  $4\pi M_s$  and the characteristic length  $\lambda$  are shown before and after each deposition. The results show fairly small changes in these two parameters. We plan to use this LPCVD spacer layer in future experiments and expect to also investigate the reversibility of the small changes observed in the magnetic properties.

Table I. Effect of LPCVD deposition on magnetic properties.

	$4\pi M_s$ [G]	$\lambda$ [ $\mu\text{m}$ ]
as grown	1371	0.0648
after LPCVD $\text{SiO}_2$	1247	0.0627
after LPCVD $\text{Si}_3\text{N}_4$	1216	0.0651

We have also deposited double layer spacers consisting of sputtered silicon dioxide followed by plasma silicon nitride. Since these are low temperature processes, no damage to the substrate is expected. However, microscopic examination of the films after polysilicon deposition showed large ( $\sim 25 \mu\text{m}$  diameter) defects. We attributed these defects to particulates deposited onto the substrate during plasma nitride deposition or stress in the film. We have completed fabrication of devices on this type of spacer layer; however, as discussed in the following section, the defects caused low yield for this process.

#### DEVICE CHARACTERISTICS

In this section, we report on the device characteristics obtained on garnet wafers. We will show that devices fabricated to date on garnet have characteristics inferior to those fabricated on silicon substrates with the same laser recrystallization process. We will also show that improvements in the process are likely to result in much improved devices.

The structure of our devices has already been introduced in Fig. 2; at this point we will describe the fabrication process in more detail. First, a single or multilayer spacer is deposited on the substrate. This insulating spacer is typically  $0.15\text{--}1.0 \mu\text{m}$  thick. On top of the spacer layer, a  $0.5\text{--}0.75 \mu\text{m}$  LPCVD polysilicon film is deposited at  $625^\circ\text{C}$ . The polysilicon is capped with  $1 \mu\text{m}$  of sputtered  $\text{SiO}_2$ , recrystallized, and then patterned into  $25 \times 100 \mu\text{m}$  islands. The silicon islands are then doped and a  $0.1 \mu\text{m}$  gate oxide is grown at  $850^\circ\text{C}$ . After opening contact windows, aluminum is deposited and patterned to form the source, drain and gate electrodes.

In a first set of wafers, we explored the feasibility of fabricating working devices and also the relative quality of devices made on garnet and silicon substrates. The devices fabricated on bubble wafers used a sputtered  $\text{SiO}_2$  spacer layer while devices fabricated on silicon used either a sputtered  $\text{SiO}_2$  or a thermal  $\text{SiO}_2$  spacer. Results from measurements of threshold voltage  $V_T$ , channel mobility  $\mu_n$  and gate leakage current  $I_G$  are shown in Table II. It should be noted that the results for the bubble substrate are from a small sample of devices since the yield was low.

The results show that devices fabricated on a thermal  $\text{SiO}_2$  layer had mobility close to that reported in the literature for laser recrystallized transistors [9], with low threshold voltages and negligible gate leakage. Devices with a sputtered  $\text{SiO}_2$  spacer on a silicon substrate showed high gate leakage and low mobility; and the worst results were on the bubble substrate where even lower mobility was observed. We attributed the high gate leakage to contamination originating in the sputtered  $\text{SiO}_2$  layer and

possibly also in the bubble substrate. Contamination was also a possible explanation for the low mobility found in transistors fabricated on the sputtered  $\text{SiO}_2$ .

Table II. Comparison of MOSFETs fabricated on sputtered and thermal  $\text{SiO}_2$ . The leakage current  $I_G$  was measured at  $V_{GS} = 3.0\text{V}$  and  $V_{DS} = 0\text{V}$ .

	sputtered $\text{SiO}_2$		thermal $\text{SiO}_2$
	GGG	silicon	silicon
$\mu_n$ [ $\text{cm}^2/\text{Vs}$ ]	6	9	306
$V_T$ [V]	2.4	2.1	-1.24
$I_G$ [A]	$5 \times 10^{-6}$	$1.0 \times 10^{-8}$	$1.1 \times 10^{-11}$

In a second experiment, some of the wafers had the double layer sputtered  $\text{SiO}_2$ / plasma  $\text{Si}_3\text{N}_4$  spacer layer which was expected to reduce contamination. Results from this experiment are shown in Table III. A bubble wafer with the double layer was initially part of the experiment, but particulate defects and process difficulties resulted in a yield too low to draw definite conclusions. As shown in the table, samples with the sputtered oxide alone had very high gate leakage currents but mobilities much improved from our first experiment. Based on these results, we are inclined to attribute the low mobilities in the first experiment to incomplete recrystallization. Partial recrystallization was observed optically in the first experiment but all wafers shown in Table II were well recrystallized. Characteristics of a good device from the bubble substrate are shown in Fig. 3.

Table III. MOSFET characteristics with improved recrystallization. The leakage current  $I_G$  was measured at  $V_{GS} = V_T + 0.7\text{V}$  and  $V_{DS} = 0\text{V}$ .

	sputtered $\text{SiO}_2$		$\text{SiO}_2/\text{Si}_3\text{N}_4$
	GGG	silicon	silicon
$\mu_n$ [ $\text{cm}^2/\text{Vs}$ ]	47	179	33
$V_T$ [V]	0.5	0.2	2.8
$I_G$ [A]	$2.5 \times 10^{-5}$	$1.5 \times 10^{-6}$	$< 6 \times 10^{-11}$

Another interesting result from this experiment is the low gate leakage current observed for the sample with the double layer spacer. Although this result needs to be confirmed, it appears that the plasma nitride is effective in preventing contamination of the gate oxide. Taking the results of the two experiments together, it appears that contamination of the oxide is the cause of the high gate leakage but that low mobility is largely a consequence of incomplete recrystallization.

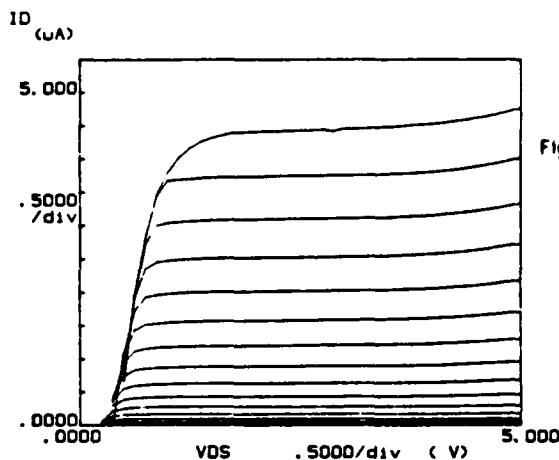


Fig 3  $I_D(V_{DS})$  characteristics for a transistor on a garnet substrate with a sputtered  $\text{SiO}_2$  spacer. The top curve is for  $V_{GS} = 1.8 \text{ V}$  and the  $V_{GS}$  step size is  $0.1 \text{ V}$ .

#### SUMMARY

In the preceding sections, we have shown that bubble films can tolerate the high temperature steps necessary for fabrication of semiconductor devices. Deposition of high quality spacer layers by LPCVD appears to be practical, although additional annealing studies clearly need to be carried out.

Operating field effect transistors have been fabricated on bubble substrates. The results show that gate leakage current still needs to be improved but that the low channel mobility initially reported is probably attributable to incomplete recrystallization. Encouraging results were obtained with a double layer spacer layer on silicon substrates so improvement of the leakage current on bubble substrates appears to be possible.

Further development of this technology will allow fabrication of an integrated semiconductor/ magnetic bubble memory device as discussed above. Such a device will offer considerable improvements in access time while retaining the nonvolatile characteristics of present bubble memories. Finally, the contamination and substrate damage problems which are found in this technology are also found in other TFT applications. Solution of these

common problems will lead to many important new applications of semiconductor device technology

#### ACKNOWLEDGEMENTS

The authors wish to acknowledge support from NASA grant #NAG-1-395 and AFOSR grant #AFOSR-84-0341. We also wish to thank J. Tabacchi for performing the ion implantation, R. Campbell for growth of LPE films, P. McMullin for assistance with the laser recrystallization, and T. Tamagawa for performing the plasma nitride depositions. The assistance of S. Dutta with our first experiment was particularly invaluable.

#### REFERENCES

1. T.J. Nelson, IEEE Transactions on Magnetics **MAG-13**, 1773 (1977).
2. A.H. Bobeck et al, IEEE Transactions on Magnetics **MAG-9**, 474 (1973).
3. O.S. Lutes, P.S. Nussbaum, O.S. Aadland, IEEE Transactions on Electron Devices **ED-27**, 2156 (1980).
4. G.A. Egiazaryan, G.A. Mantsakanyan, V.I. Murigin, and V.I. Staveev, Sov. Phys. -Semicond. **9**, 829 (1975).
5. P.W. Fry and S.J. Hoey, IEEE Transactions on Electron Devices **ED-16**, 35 (1969).
6. P.H.L. Rasky, D.W. Greve, M.H. Kryder and S. Dutta, J. Appl. Phys. **57**, 4077 (1985).
7. P.H.L. Rasky, M.S. project report, Carnegie-Mellon University, 1984 (unpublished).
8. J.A. Appels et al, Philips Res. Rep. **25**, 118 (1970).
9. H.S. Lee, Appl. Phys. Lett. **38**, 770 (1981).

# NEARLY ISOTROPIC PROPAGATION OF 0.5 MICROMETER BUBBLES IN CONTIGUOUS DISK DEVICES\*

Soonchul Jo and M.H.Kryder  
Magnetics Technology Center and  
Department of Electrical and Computer Engineering  
Carnegie Mellon University, Pittsburgh, PA 15213

## Abstract

"Good" and "bad" ion implanted bubble propagation tracks of various shaped patterns (snake, diamond, circular and triangular shapes) were fabricated on garnet films for 0.5  $\mu\text{m}$  bubbles with nearly isotropic magnetostriction. Quasistatic bias margin measurements show great improvement of bad track margins for all pattern shapes. The best overlapping bias margins were obtained from 2.5  $\mu\text{m}$  period diamond shaped patterns, which show a 30 Oe minimum drive field and 78 Oe margin width at 50 Oe drive. On the other hand, snake patterns exhibit the best "good" track margin with a minimum drive of 25 Oe and a margin width of 78 Oe at 50 Oe drive, but show somewhat inferior "bad" track margins. It was found that "bad" track margins of snake patterns are especially sensitive to ion implantation conditions and the propagation pattern cusp shape. By carefully adjusting ion implantation conditions (implantation energy and dosage) and the pattern cusp shape, nearly isotropic propagation was achieved for all propagation pattern shapes tested.

## Introduction

Bubble garnets of (111) orientation and small magnetostriction coefficient difference  $\delta\lambda$  ( $=\lambda_{100} - \lambda_{111}$ ) are of considerable interest for use in ion implanted contiguous disk bubble memory devices (1), since they open up the possibility of fabricating devices with propagation margins which are independent of their propagation track orientation. Theory (2,3) indicates that the three fold symmetric behavior of bubbles in ion implanted contiguous disk devices can be drastically reduced by proper selection of magnetostriction coefficients ( $\lambda_{111} \approx \lambda_{100}$ ). Since unequal bias margins for bubbles, propagating along different crystal directions are believed to be due to the three fold symmetric magnetostrictive anisotropy, virtual elimination of the magnetostrictive anisotropy should allow uniformly good bubble propagation independent of track orientation. This will in turn significantly alleviate chip layout problems associated with the so called "bad" tracks (4,5). Here we describe an experimental study of propagation of 0.5  $\mu\text{m}$  bubbles in (111) garnets having nearly isotropic magnetostriction. The effects of pattern geometry, ion implantation conditions, and propagation direction are all considered.

## Experimental

Propagation tracks with various cell shapes and different orientations were fabricated on 0.5 $\mu\text{m}$  bubble garnet films with small  $\delta\lambda$ . Garnet films used for the device fabrication are bismuth and dysprosium substituted iron garnets grown by liquid phase epitaxy. The characteristics of one of the films (CA 71) studied are shown in Table I. The other film (CA 72) studied has slightly different film characteristics than CA 71, the main difference being somewhat higher effective uniaxial anisotropy (by 250 Oe).

\*This work was supported by the Air Force Office of Scientific Research under grant 84-0341, the National Science Foundation under grant ECS-8307261, and the National Research and Resource Facility for Submicron Structures under NSF grant ECS-8200312.

Table 1: Garnet Film Characteristics (CA 71)

Composition	$\{\text{Bi}_{0.4}\text{Dy}_{0.7}\text{Sm}_{0.2}\text{Lu}_{1.5}\text{Y}_{0.2}\}\text{[FeGa]}_5(\text{O})_{12}$
Thickness t	0.65 $\mu\text{m}$
Collapse field $H_0$	580 Oe
Material length l	0.054 $\mu\text{m}$
Magnetization $4\pi M$	960 G
Uniaxial anisotropy $H_k$	1850 Oe
Quality factor Q	1.9
Bubble diameter d	0.5 $\mu\text{m}$
Magnetostriction coeff. $\lambda_{111}$	$-3.1 \times 10^{-6}$
$\lambda_{100}$	$-2.1 \times 10^{-6}$

Ion implantation masks for propagation patterns were formed by electroplating gold through a photolithographic mask. Firstly, 80 nm of  $\text{SiO}_2$  and the plating base (Mo and Au) were sputtered on the film. Then, photoresist patterns were delineated using 500 nm thick AZ 4070 resist and a Karl Suss contact aligner with a mid U.V. (310 nm) light source. Then, 350 nm of gold was electroplated using Selrex Corporations' BDT 510 gold bath. Current density used was 3  $\text{mA}/\text{cm}^2$ . After the electroplating, deuterium was doubly implanted to define the propagation tracks. Implantation energies and dosages were varied to find optimum conditions for bubble propagation. Implantation energies and dosages which give approximately 230 nm of implantation depth and relatively uniform implant with in plane Q of -2.5, gave good propagation margins for most of the 2.5  $\mu\text{m}$  period patterns. The ion implantation conditions are listed in Table II.

Table 2: Ion Implantation Conditions

	Ion species	Energy	Dosage
1st implantation	Deuterium	46 Kev	$7.5 \times 10^{15}/\text{cm}^2$
2nd implantation	Deuterium	26 Kev	$5 \times 10^{15}/\text{cm}^2$

Finally, the gold implantation masks together with the plating base were stripped with Au etchant and aluminum was evaporated to be used as the reflection layer for the observation of bubbles by a polarized light microscope. High Faraday rotation due to Bi substitution in the garnet film and the Al mirror gave excellent visibility so that bubbles were easily observed up to collapse.

The devices were tested by measuring quasi-static (1 Hz) bias margins for "good" and "bad" tracks. Data patterns were randomly generated by slowly raising the bias field from the bubble stripe out state. Propagation around the corners was included in the bias margin measurements and the number of cycles of propagation varied from a few tens to 250. The propagation pattern shapes studied in this paper are illustrated in Figure 1.

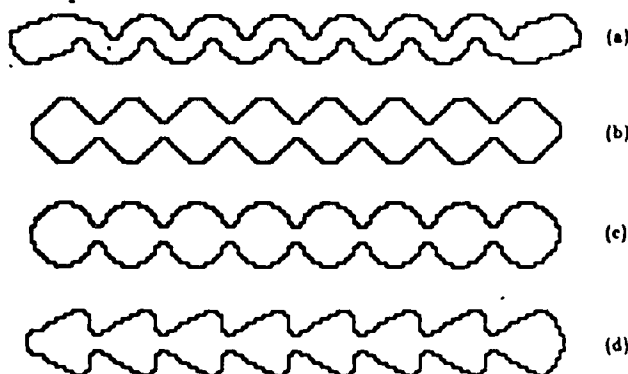


Figure 1: Bubble Propagation Shapes  
(a) Snake (b) Diamond (c) Circle (d) Triangle

### Results and Discussion

Bubble circulation bias margins around isolated propagation elements were measured and results are shown in Figure 2. Bias margin curves around 2  $\mu\text{m}$  and 4  $\mu\text{m}$  diameter circles show minimum drive field of 10 Oe and margin width of at least 24% and 27% of mid bias values, respectively. These results are comparable to those published earlier (6), for 1  $\mu\text{m}$  bubbles circulating 4  $\mu\text{m}$  and 8  $\mu\text{m}$  circles, fabricated from garnet films with low magnetostriction coefficient difference. Circulation margins for two 2  $\mu\text{m}$  period triangular propagation elements are

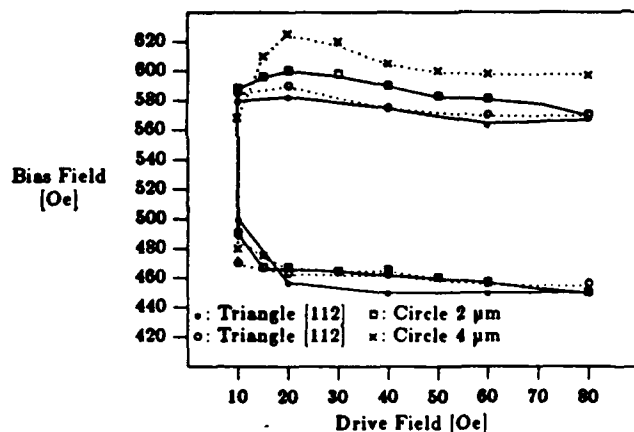


Figure 2: Bubble Circulation Bias Margins around Isolated Propagation Pattern Cells Film CA 71

also shown in Figure 2. One triangle is oriented in such a way that the vertices point to the easy magnetization directions ( $[11\bar{2}]$ ) and the other triangle to the easy stripeout directions ( $[\bar{1}\bar{1}2]$ ). The margins are quite similar to those for the 2  $\mu\text{m}$  diameter circle except slightly lower collapse field is observed for the diamonds. This is strongly in contrast to the results obtained from conventional high  $\delta\lambda$  garnet films, which show drastically smaller margin width for  $[11\bar{2}]$  oriented triangles (7). We attribute these results to the small magnetostriction coefficient difference in our films.

Bias margins of "good" and "bad" 2.5  $\mu\text{m}$  period tracks for diamond, circle, triangle and snake shaped bubble propagation patterns were measured. Figures 3, 4 and 5 show results obtained from film CA71. "Good" and "bad" track margins for diamond shaped patterns are shown in Figure 3, which show almost identical bias margins for "good" and "bad" tracks with the minimum in plane drive field of 30 Oe and the margin width of 80 Oe (15% of the mid bias).

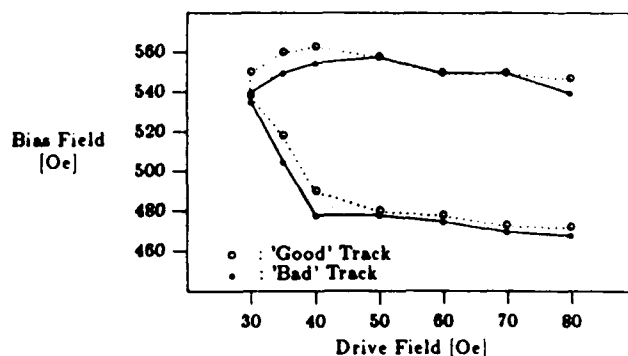


Figure 3: Margins for 2.5  $\mu\text{m}$  period Diamond Shaped propagation pattern Film CA 71

This is a dramatic improvement of "bad" track margins over those typically seen in ion implanted devices with conventional garnet films (4).

Bias margins for other cell shapes show slightly higher minimum drive fields for "bad" tracks, but similar margin widths for both tracks except the snake shape. Overlapping bias margins of "good" and "bad" tracks for diamond, triangle, circle and snake shaped propagation tracks are shown in Figure 4. The best overlapping margins are obtained from the diamond shape and the worst from the snake. The reason that the snake patterns have the worst overlapping bias margins is mainly due to the skidding of bubbles along the bad tracks (propagation of more than one period of the track during one cycle of the in-plane drive field) at high bias fields. On the other hand, the snake patterns show the

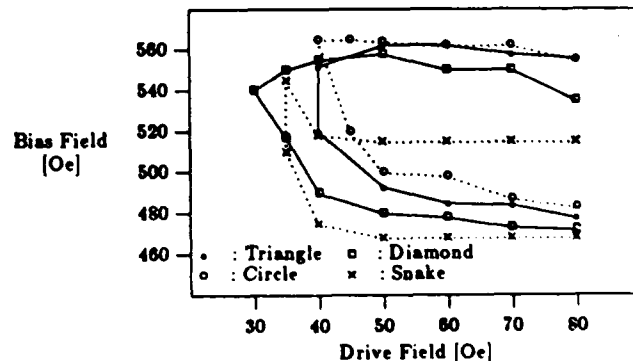


Figure 4: Overlapping Margins for 2.5  $\mu\text{m}$  Period Diamond, Triangle, Circle and Snake Patterns Film CA 71

best "good" track margin (25 Oe minimum drive and 15% margin width). The "good" and "bad" track bias margins for snake patterns are plotted in Figure 5.

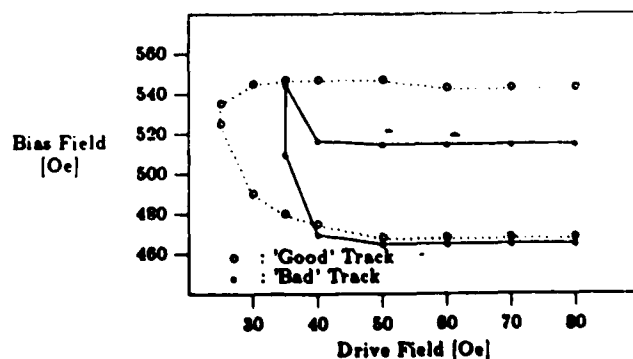


Figure 5: Margins for 2.5  $\mu\text{m}$  Period Snake Shaped Patterns Film CA 71

Figures 6 and 7 illustrate bias margin measurements obtained from snake patterns on film CA 72. Ion implantation conditions were the same as CA 71, which were shown in Table II. "Good" and "bad" track margins for 2  $\mu\text{m}$  period snake patterns are shown in Fig. 6. Figure 6 (a) shows the results obtained from the patterns with the cusp depth to track period ratio of 0.44, while Figure 6 (b) shows margins from the patterns with the cusp depth to track period ratio of 0.38. It is clear from the margin plots

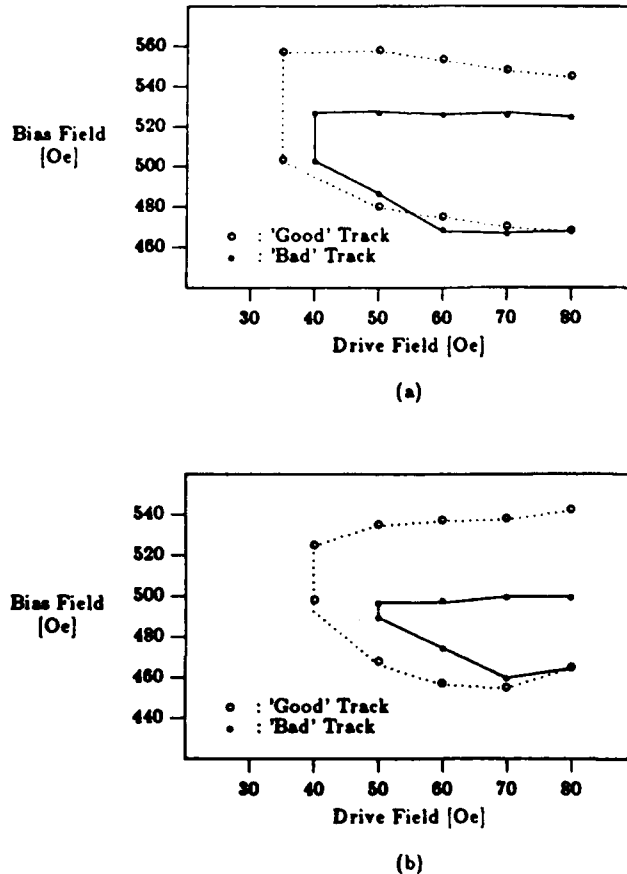


Figure 6: Margins for 2  $\mu\text{m}$  Period Snake Patterns with (a) Cusp to Period Ratio of 0.44 (b) Cusp to Period Ratio of 0.38 Film CA 72

that a slight change of cusp dimension ( $1/8 \mu\text{m}$ ) could significantly affect the bias margins, especially for the "bad" tracks. It seems from these plots and previous margin plots of film CA 71 that sharper cusp definition (for example, snake patterns with deeper cusps and diamond patterns) help prevent bubbles from skidding along "bad" tracks. As Lin et al. (1) pointed out, wider and smoother cusps yield better margins as demonstrated in "good" snake patterns. But, at the same time such cusps seem to promote the skidding failure mode in "bad" tracks.

Figure 7 shows bias margins for 2.5  $\mu\text{m}$  period snake patterns made with film CA 72. They have the same cusp shape as the patterns whose margins are shown in Figure 5 (CA 71). The cusp depth to track period ratio of these patterns is 0.35. CA 71 and CA 72 were ion implanted with the same conditions and at the same time as noted earlier. Somewhat higher effective anisotropy of CA 72 than CA 71 (by 250 Oe) resulted in a slightly lower (magnitude) in plane Q for CA 72 than CA 71. The "bad" track margin shows considerable improvement in margin width compared with CA 71, even though the minimum drive field of the good track margin has increased slightly (by 5 Oe). Still, the overlapping bias margin is significantly better than the margin of CA 71 with a minimum drive of 35 Oe and margin width of 70 Oe (14% of mid bias value).

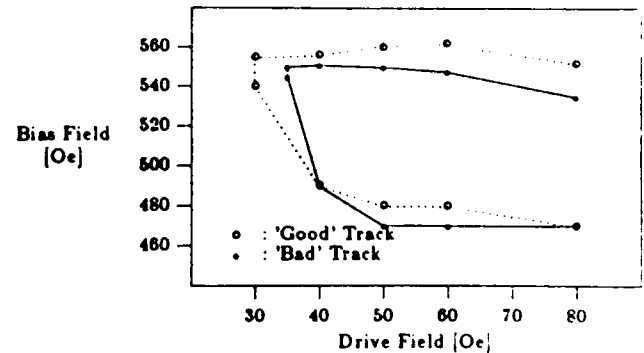


Figure 7: Margins for 2.5  $\mu\text{m}$  Period Snake Patterns Film CA 72

The failure mechanism of the "bad" tracks in the snake pattern at high bias fields was bubble collapse at low and medium drive and bubble skidding at high drive. This contrasts to the predominant skidding failure mechanism of film CA 71. This shows that with proper ion implantation, we can largely avoid skidding failures at high bias, producing good "bad" track propagation. It is to be noted that the skidding failure mode is not limited to snake patterns. It was observed in other propagation patterns with different ion implantation conditions.

## Conclusions

Bubble propagation tracks of various cell shapes were fabricated on bismuth substituted 0.5  $\mu\text{m}$  garnet films with small magnetostriction coefficient difference. Bias margin measurements show great improvement of "bad" track margins for all cell shapes tested. Diamond shaped patterns exhibited the best overlapping bias margins. Although snake shaped patterns show the best "good" track margins, their "bad" track margins are most susceptible to a skidding failure mechanism at high bias fields, which could significantly degrade the margins. It was found that "bad" track margins (notably of snake patterns) are very sensitive to ion implantation conditions and pattern cusp shape. Nearly isotropic bubble propagation was achieved for all the track shapes tested by careful adjustment of ion implantation conditions (implantation energy and dosage, i.e., implantation depth and in plane Q) and track cusp shape.

## Acknowledgement

The authors wish to thank R. Campbell and S. Santhanam for garnet film growth, J. Tabacchi and Dr. A. Guzman for ion implantation, R. Tiberio and S. Burgess of the National Submicron Facility for E-beam mask generation and J. Wullert for setting up the bubble exerciser.

## References

1. Y.S. Lin, G.S. Almasi and G.E. Keefe, IEEE Tran. Mag., **MAG-13**, No. 6, 1744(1977).
2. M.H. Kryder and D.A. Saunders, IEEE Tran. Mag., **MAG-19**, No. 3, 1817(1983).
3. A. Hubert, J. Magnetism and Magnetic Materials, **31-34**, 976(1983).
4. Y.S. Lin, G.S. Almasi, D.B. Dove, G.E. Keefe and C.C. Shir, J. Appl. Phys., **50**(3), 2258(1979).
5. R. Wolfe and T. J. Nelson, IEEE Tran. Mag., **MAG-15**, No. 5, 1323(1979).
6. H. Makino, O. Okada, Y. Hidaka, J. of Appl. Phys., **55**(6), 2551(1984).
7. C.C. Shir, J. Appl. Phys., **52**(3), 2388(1981).



# TEMPERATURE DEPENDENCE OF 0.5 MICROMETER BUBBLE PROPAGATION IN ION IMPLANTED DEVICES\*

Soonchul Jo and M.H.Kryder  
Magnetics Technology Center and  
Department of Electrical and Computer Engineering  
Carnegie Mellon University, Pittsburgh, PA 15213

## Abstract

The temperature dependence of 0.5  $\mu\text{m}$  bubble propagation in ion implanted propagation tracks fabricated with garnet films having nearly isotropic magnetostriction is reported. The propagation track cell size was 2.5  $\mu\text{m}$  x 2.5  $\mu\text{m}$  and the nominal bubble garnet film composition was  $\{\text{Bi}_{0.4}\text{Dy}_{0.7}\text{Sm}_{0.2}\text{Lu}_{1.5}\text{Y}_{0.2}\}[\text{FeGa}]_5(\text{O})_{12}$ . "Good" and "bad" track bias margins of diamond and circular patterns were measured from 0°C to 130 °C. The patterns showed good overlapping margin width (at least 13 % of mid bias value) of "good" and "bad" tracks up to 120 °C. The margins shifted down monotonically as temperature increased with a coefficient of roughly -0.27 % /°C (at 50 °C). The minimum drive field in general showed a monotonic decrease with temperature increase. The wider overlapping bias margin width (at least 14% of mid bias value) and the lower minimum drive field ( at most 40 Oe) over the temperature range tested were obtained from the diamond patterns. It was also observed that the patterns actually showed slightly higher collapse field for "bad" tracks than "good" tracks depending on the rotation sense of the drive field.

\*This work was supported by the Air Force Office of Scientific Research under grant 84-0341, the National Science Foundation under grant ECS-8307261, and the National Research and Resource Facility for Submicron Structures under NSF grant ECS-8200312.

PACS numbers: 85.70Ge, 85.90Kh, 85.70Qn

## Introduction

The temperature dependence of magnetic bubble propagation is of great practical interest because it essentially determines the operating temperature range of the magnetic bubble memory devices. It has been reported that the operating temperature range of ion implanted devices depends on the garnet film characteristics and the ion implantation conditions. Mizuo and Urai<sup>1</sup> demonstrated that hydrogen implantation allows much higher operating temperature limits than the helium implantation for the same garnet films. Fratello et al.<sup>2</sup> and Arbaugh and Fairholme<sup>3</sup> showed that bismuth substituted garnet films gave wide operating temperature range.

As was reported in our previous paper<sup>4</sup>, we have grown garnet films supporting 0.5  $\mu\text{m}$  bubbles with nearly isotropic magnetostriction. The various shaped propagation tracks fabricated on the films by implanting deuterium molecules showed nearly isotropic propagation. Here, we describe the temperature dependence of 0.5  $\mu\text{m}$  bubble propagation in those propagation tracks.

## Experimental

The garnet film used in this experiment was bismuth and dysprosium substituted iron garnet and its nominal composition is  $\{\text{Bi}_{0.4}\text{Dy}_{0.7}\text{Sm}_{0.2}\text{Lu}_{1.5}\text{Y}_{0.2}\}[\text{FeGa}]_5(\text{O})_{12}$ . Other material

characteristics are as follows: film thickness  $t=0.65 \mu\text{m}$ , characteristic length  $l=0.054 \mu\text{m}$ , collapse field  $H_c=580 \text{ Oe}$ , saturation magnetization  $4\pi M=1020 \text{ G}$ , uniaxial anisotropy field  $H_k=2100 \text{ Oe}$ , magnetostriction coefficients  $\lambda_{111}=-3.1 \times 10^{-6}$  and  $\lambda_{100}=-2.1 \times 10^{-6}$ . Deterium was doubly implanted to define the propagation tracks. Implantation depth of approximately 230 nm and in-plane Q of -2.5 gave the best bubble propagation. The propagation test was performed without annealing. The detailed fabrication procedure is described in our previous paper<sup>4</sup>.

Quasi-static (1 Hz) bias margins were measured to study the temperature characteristics of the device. The propagation pattern shapes studied in this paper are illustrated in Figure 1. The device cell size was  $2.5 \mu\text{m} \times 2.5 \mu\text{m}$ . Propagation tracks were oriented in the  $[\bar{1}12]$  direction of the garnet crystal which is a "good" propagation direction<sup>5,6</sup> and in the  $[1\bar{1}0]$  direction. The  $[1\bar{1}0]$  direction is perpendicular to the  $[\bar{1}12]$  direction and is a "bad" and "super" propagation direction i.e., one side of the track is a "bad" direction and the other "super".

## Results and Discussion

"Good" and "bad" track bias margins of diamond and circular propagation patterns were measured from  $0^\circ\text{C}$  to  $130^\circ\text{C}$ . Figure 2 shows the temperature dependence of the minimum drive fields of diamond and circular propagation patterns as a function of

temperature. The curves show a monotonic decrease of the minimum drive as the temperature is increased. The decrease of the minimum drive was previously attributed to the decrease of the cubic magnetocrystalline anisotropy<sup>1</sup>. Since it is now believed that the dominant source of the three fold anisotropy is the magnetostrictive anisotropy due to partial relaxation of the stress at the boundary of the implanted and unimplanted regions<sup>7,8</sup>, it seems to be more reasonable to assume that the decrease of the minimum drive is mainly due to the decrease of the magnetostriction coefficients and the difference of the two coefficients  $\lambda_{111}$  and  $\lambda_{100}$  which is proportional to the anisotropy energy<sup>7</sup>. The temperature dependence of magnetostriction coefficients of  $\text{Sm}_3\text{Fe}_5\text{O}_{12}$  and  $\text{Dy}_3\text{Fe}_5\text{O}_{12}$  as well as the difference of the two coefficients shows a steady decrease as the temperature increases<sup>9</sup>. Since the magnetostriction coefficients of our garnet film are mainly determined by Dy and Sm, the above explanation seems to be reasonable. Diamond patterns showed lower drive fields for both "good" and "bad" tracks (less than 40 Oe). It is interesting to see that the minimum drive fields for supposedly "bad" tracks are actually lower than "good" tracks for most of the temperature range. This will be explained later on.

Figure 3 shows bubble propagation bias margins at 60 Oe drive field as a function of chip temperature of diamond and circular

patterns. The margins shifted downward monotonically as the temperature increased with a coefficient of roughly  $-0.27\%/^{\circ}\text{C}$  (at  $50^{\circ}\text{C}$ ). Diamond patterns showed the wider overlapping margin of "good" and "bad" tracks (80 Oe or 15% of mid bias value at  $40^{\circ}\text{C}$ ). Circular patterns showed almost no margin width variation throughout the temperature range tested. At  $130^{\circ}\text{C}$ , they still showed 55 Oe (14% of mid bias) of overlapping bias margin. Margin degradation at high temperature was due to a decrease of collapse field at high drive field.

It is interesting to note that the collapse field of the "bad" tracks in most of the temperature range is actually slightly higher than that of "good" tracks. The reason why the collapse field of "bad" tracks is higher than that of "good" tracks is as follows. To understand the problem, we observed the charged wall (and bubble) direction as a function of drive field around an unimplanted disk of diameter  $4\text{ }\mu\text{m}$  at low drive field (15 Oe). The crystal orientation of the disk and bubble jumping directions due to charged wall flip motion<sup>10</sup> are shown in Figure 4 (a). The  $[\bar{1}12]$  direction is designated as  $0^{\circ}$  of rotation. As is shown in the figure, charged wall (and bubble) jumping occurs at  $20^{\circ}$ ,  $180^{\circ}$  and  $290^{\circ}$ . Figure 4 (b) shows propagation tracks oriented in the "good" direction ( $[\bar{1}12]$ ) and "super" and "bad" direction (perpendicular to "good" direction). Short lines around the tracks

indicate in-plane drive field directions where the charged wall flip motion or the bubble jumping occurs. It is to be noted at this point that the most difficult part of the propagation process is to move the bubbles out of the cusps. Suppose that the drive field rotates in a clockwise direction. Bubbles leaving cusps from the bottom side of the "good" tracks are subject to charged wall jumping as they start to move out of the cusps while bubbles on the top side of the tracks do not encounter such adverse condition as they leave the cusps. Therefore, the failure mode at high bias is bubble collapse at the bottom cusps.

Now consider the "bad" track. Here, bubbles are subject to charged wall jumping after they come out of the cusps. Therefore bubbles can follow the jumping motion of the charged wall relatively well and thus have higher collapse field. This charged wall behavior difference is believed to be responsible for the slightly higher collapse field of "bad" tracks than "good" tracks. It is to be remembered that the garnet film is nearly isotropic to begin with.

Further evidence to support this explanation is found by reversing the in-plane field rotation direction. Now bubbles both on the top side of the "good" track and on the "bad" track encounter charged wall jumping after they get out of the cusps.

Therefore, we expect that the bubbles on both tracks will behave similarly. It is to be noted that all the margin plots presented so far were measured using clockwise rotating in-plane fields. Figure 5 shows bias margins of diamond patterns obtained by clockwise (a) and counterclockwise (b) rotating in-plane fields. Figure 5 (b) shows an increase of "good" track collapse field and almost identical bias margins for both "good" and "bad" tracks. This is in agreement with our explanation above.

As was mentioned earlier, the minimum drive field of "bad" tracks are generally lower than that of "good" tracks. By looking at Figures 2 and 3, we find excellent correlation between the minimum drive field and the collapse field of respective "good" and "bad" tracks. When the collapse field of the "bad" track is higher than that of the "good" track, the minimum drive of the "bad" track is lower than that of the "good" track and vice versa. This is easily explained by the previous argument. When the collapse field is higher, it is easier for the bubbles to come out of the cusps, therefore the minimum drive is lower and vice versa.

### Conclusion

The temperature dependence of 0.5  $\mu\text{m}$  bubble propagation in ion implanted propagation tracks fabricated with garnet films having nearly isotropic magnetostriction was measured over the temperature range of 0  $^{\circ}\text{C}$  to 130  $^{\circ}\text{C}$ . The results show good



overlapping bias margins of "good" and "bad" tracks up to 120 °C (at least 13% of mid bias). The wider overlapping margin width (at least 14% of mid bias) and the lower minimum drive field (at most 40 Oe) over the temperature range tested were obtained from the diamond patterns. Circular patterns showed a consistent margin width (60 Oe) throughout the temperature range. The patterns exhibited slightly higher collapse fields for "bad" tracks than "good" tracks depending on the rotation sense of the drive field. This is explained by the fact that the charged wall flip motion occurred when the bubble was being pulled out of a cusp for the "good" tracks, but after coming out of a cusp for the "bad" tracks.

### **Acknowledgement**

The authors wish to thank R. Campbell and S. Santhanam for garnet film growth and useful discussions, J. Tabacchi and Dr. A. Guzman for ion implantation and R. Tiberio and S. Burgess of the National Submicron Facility at Cornell University for E-beam mask generation.

## References

1. K. Mizuno and H. Urai, IEEE tran. Mag., MAG-21, No.5, 1706(1985)
2. V.J. Fratello, R.D. Pierce and C.D. Brandle, J. Appl. Phys., 57(8), 4043(1985).
3. L.G. Arbaugh Jr. and R.J. Fairholme, IEEE tran. Mag., MAG-22, No.5, 1287(1986)
4. S.Jo and M.H. Kryder, IEEE tran. MAG., MAG-22, No.5, 1278(1986)
5. Y.S. Lin, G.S. Almasi, D.B. Dove, G.E. Keefe and C.C. Shir, J. Appl. Phys., 50(3), 2258(1979).
6. R. Wolfe and T. J. Nelson, IEEE Tran. Mag., MAG-15, No.5, 1323(1979).
7. M.H. Kryder and D.A. Saunders, IEEE Tran. Mag., MAG-19, No.5, 1817(1983).
8. A. Hubert, J. Magnetism and Magnetic Materials, 31-34, 976(1983).
9. G. Winkler, *Magnetic Garnets*, Friedr. Vieweg & Sohn, 1981.
10. Y.S. Lin, D.B. Dove, S. Schwarzl and C.C. Shir, IEEE Tran. MAG., MAG-14, No.5, 494(1978).

## List of Figures

<b>Figure 1:</b>	Bubble propagation shapes. (a) diamond and (b) circular patterns	10
<b>Figure 2:</b>	Temperature dependence of minimum drive field for (a) diamond and (b) circular patterns	12
<b>Figure 3:</b>	Temperature dependence of bias margin at 60 Oe of drive field for (a) diamond (b) circular patterns	13
<b>Figure 4:</b>	Charged wall flip (and bubble jumping) directions of (a) unimplanted disk and (b) propagation tracks	14
<b>Figure 5:</b>	Bias margins of diamond patterns with (a) clockwise and (b) counterclockwise rotating drive field at 40 °C	15

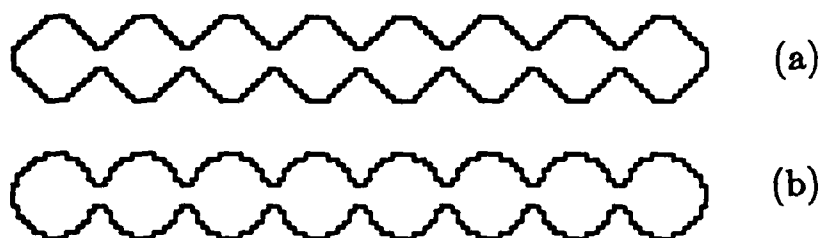


**Figure 1: Bubble propagation shapes.**  
(a) diamond and (b) circular patterns

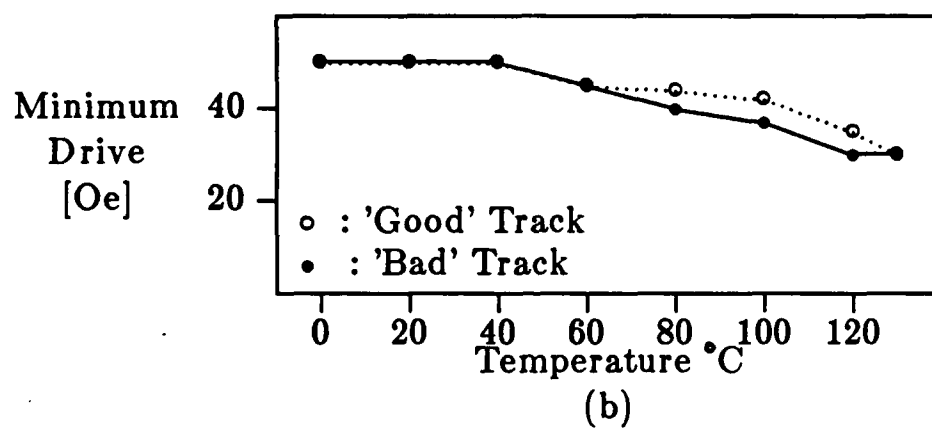
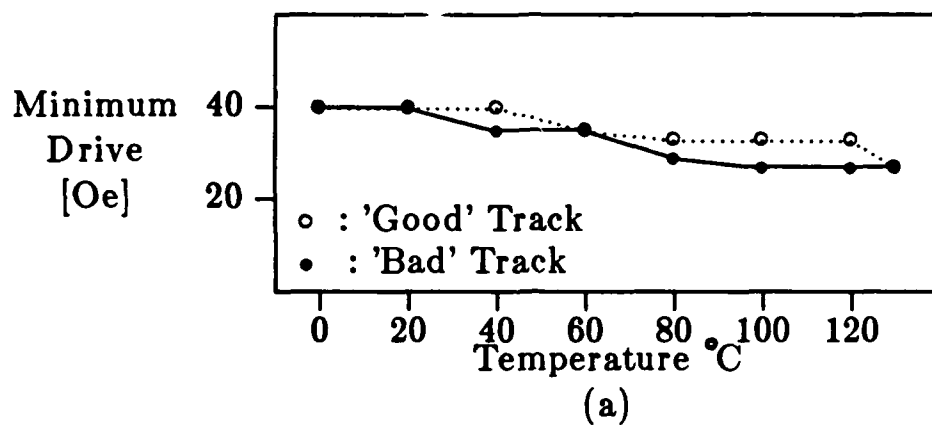


**Figure 2:** Temperature dependence of minimum drive field for  
(a) diamond and (b) circular patterns

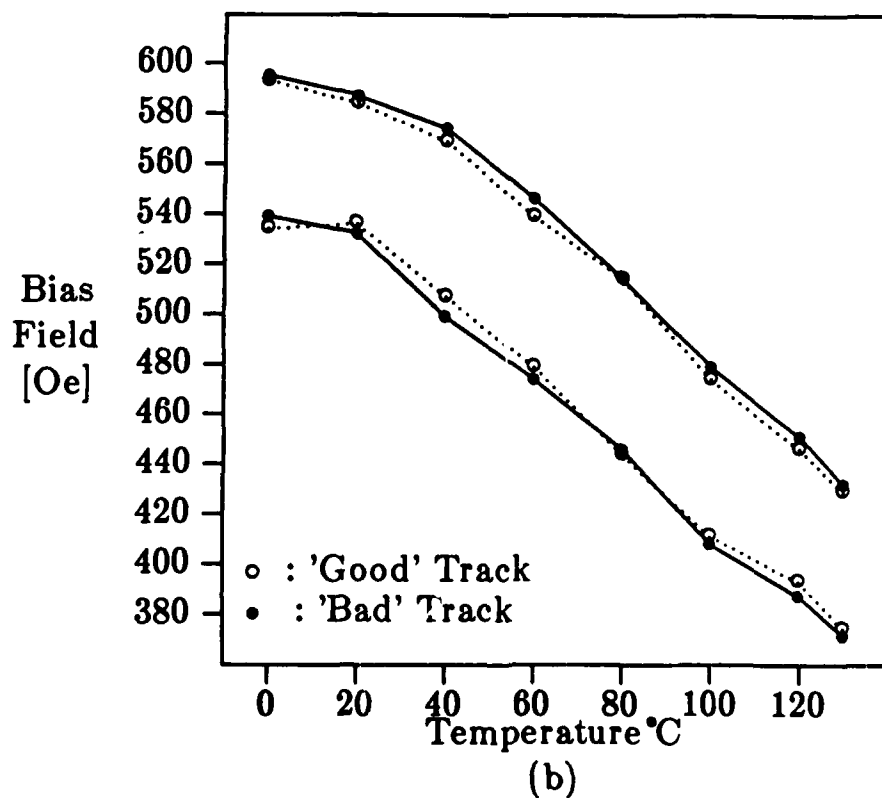
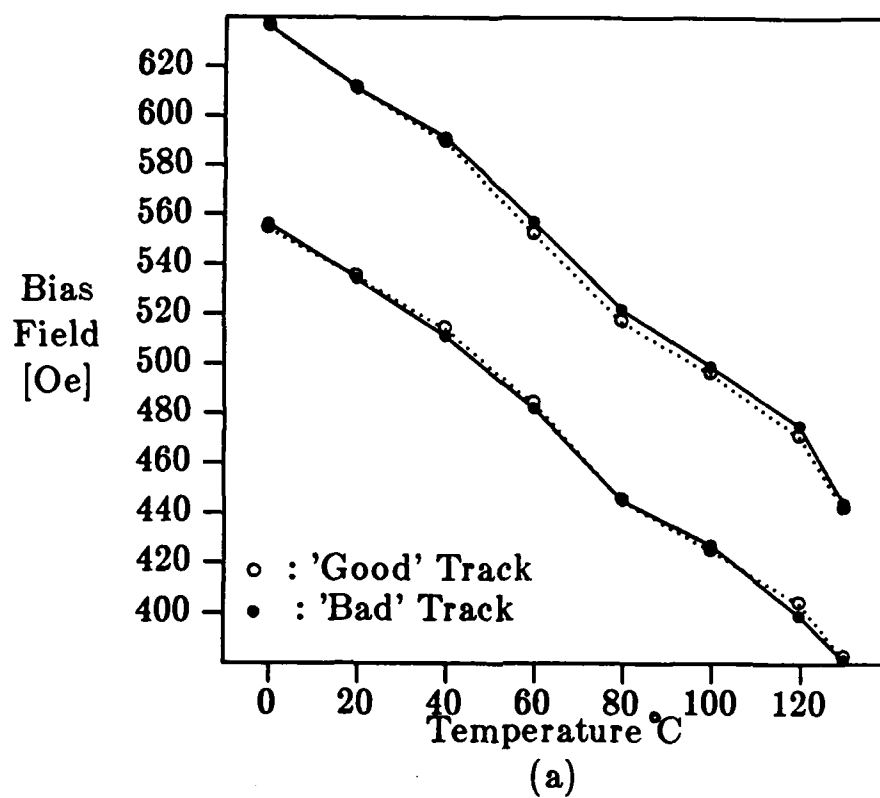
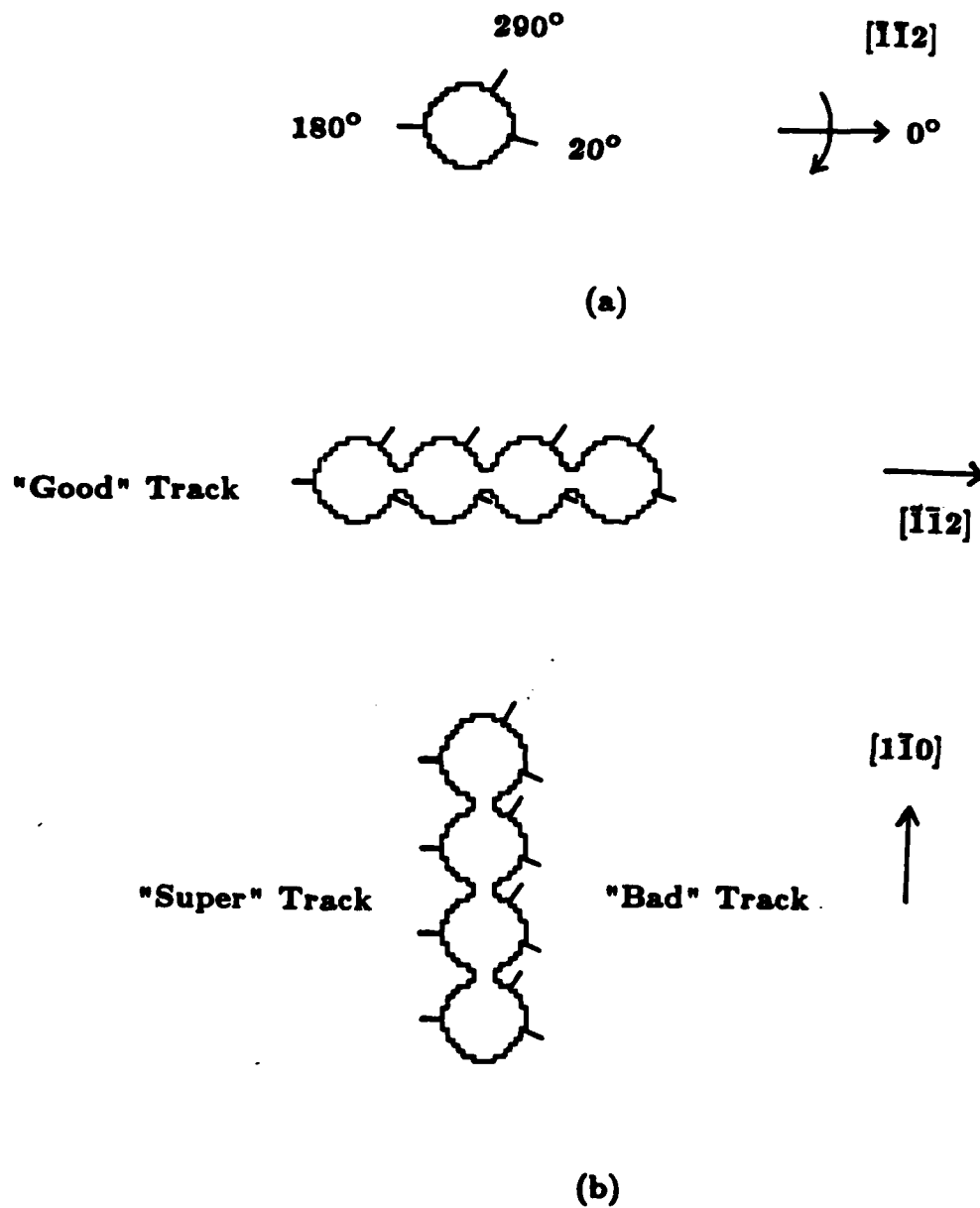
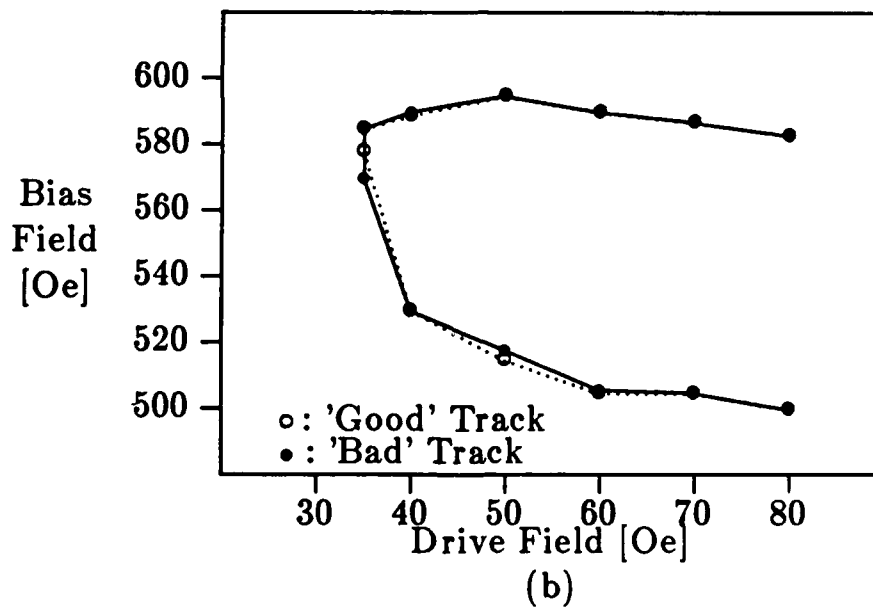
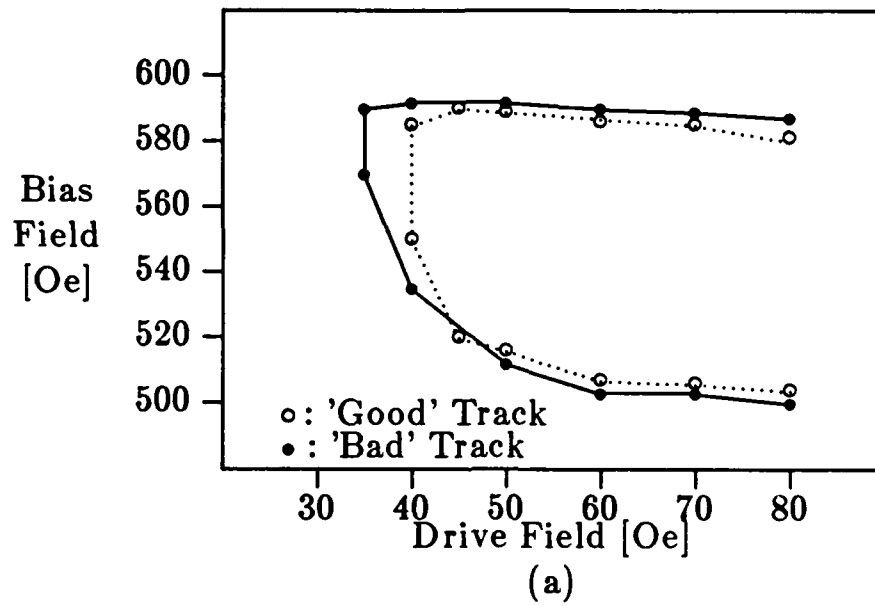


Figure 3: Temperature dependence of bias margin at 60 Oe of drive field for (a) diamond (b) circular patterns



**Figure 4:** Charged wall flip (and bubble jumping) directions of  
(a) unimplanted disk and (b) propagation tracks



**Figure 5:** Bias margins of diamond patterns with (a) clockwise and (b) counterclockwise rotating drive field at 40 °C



# Isotropic Propagation in Submicron Ion Implanted Magnetic Bubble Devices

R.O. Campbell, Soonchul Jo, and M.H. Kryder

Magnetics Technology Center

Carnegie-Mellon University

Pittsburgh, PA 15213

## Abstract

Submicrometer diameter bubble materials with nearly isotropic magnetostriction were used in  $2.5\mu\text{m}$  period ion-implanted contiguous disk devices. Similar margins for the "good" and "bad" propagation directions (parallel and perpendicular to  $[11\bar{2}]$ ) were measured with a minimum drive of about 40 Oe. The propagation margins were shown to be 14% for the bad orientation and 15% for the good orientation with significant overlap. The films have large, negative, and nearly equal magnetostriction coefficients along the  $[111]$  and the  $[100]$  directions. The use of Dy and Bi enabled the films to have isotropic magnetostriction, and the use of Bi allowed  $0.5\mu\text{m}$  diameter bubbles with a large  $Q (=H_k/4\pi M_s)$  of 1.85.

## Introduction

The propagation margins of bubble domains in ion-implanted contiguous disk devices fabricated on  $[111]$  garnets were observed by Lin<sup>1</sup> and Wolfe<sup>2</sup> to exhibit three-fold symmetry. Lin<sup>1</sup> noted that the propagation margins of bubble domains propagating on both sides of tracks parallel to the  $[11\bar{2}]$  direction were approximately equal and acceptably large. These he referred to as "good" tracks. On the other hand, he observed that for tracks oriented perpendicular to the  $[11\bar{2}]$  directions, margins were anomalously large on one side (the "super" track) and anomalously small on the other side (the "bad" track). These three-fold symmetric margins have considerably complicated the design of ion-implanted devices. Initially it was believed that magnetocrystalline anisotropy caused the anisotropic behavior<sup>1</sup>, but later it was realized that anisotropic magnetostriction was the cause.<sup>3, 4</sup> Kryder and Saunders<sup>4</sup> proposed that the anisotropic effects could be eliminated by growing materials with negative and isotropic magnetostriction constants,  $\lambda_{111} = \lambda_{100}$ . Garnet materials with negative magnetostriction coefficients have been reported by Makino et al.<sup>5</sup>; however, the material did not have isotropic magnetostriction ( $\lambda_{111} = -2.3 \times 10^{-6}$  and  $\lambda_{100} = -0.9 \times 10^{-6}$ ). In this letter we report the growth of materials with nearly isotropic magnetostriction, which support submicrometer bubble domains and which have been demonstrated to provide greatly improved propagation margins along the so-called "bad" track.

## Film Development

The development of the isotropic magnetostrictive films described here relies upon the film constituents bismuth and dysprosium. Dysprosium iron garnet has  $\lambda_{100} < \lambda_{111}$  while most other rare-earth iron garnets have  $\lambda_{111} < \lambda_{100}$ . Bismuth does not affect the magnetostriction coefficients greatly, but it does provide the uniaxial anisotropy required for a bubble device. The magnetostriction coefficients of bismuth iron garnet were estimated from data given by Makino et al.<sup>5</sup> and Hansen et al.<sup>6</sup> By careful selection of film constituents it is possible to obtain films in which  $\lambda_{111} = \lambda_{100}$ , and in which the magnetostriction is large and negative as required for ion-implanted devices.

AD-A174 621

DESIGN AND FABRICATION OF SUBMICRON MAGNETIC BUBBLE  
DEVICE TECHNOLOGY (U) CARNEGIE-MELLON UNIV PITTSBURGH  
PA DEPT OF ELECTRICAL AND COM H H KRYDER ET AL

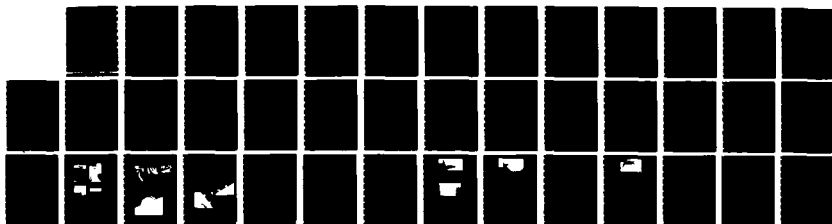
2/2

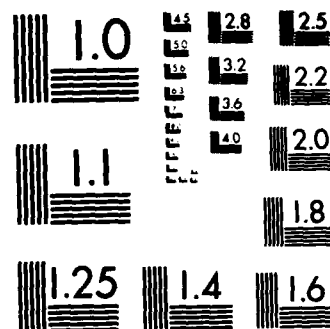
UNCLASSIFIED

31 OCT 86 AFOSR-TR-86-1075 AFOSR-84-0341

F/G 14/3

NL





MICROCOPY RESOLUTION TEST CHART  
NATIONAL BUREAU OF STANDARDS-1963-A

## Introduction

The propagation margins of bubble domains in ion-implanted contiguous disk devices fabricated on [111] garnets were observed by Lin<sup>1</sup> and Wolfe<sup>2</sup> to exhibit three-fold symmetry. Lin<sup>1</sup> noted that the propagation margins of bubble domains propagating on both sides of tracks parallel to the  $[11\bar{2}]$  direction were approximately equal and acceptably large. These he referred to as "good" tracks. On the other hand, he observed that for tracks oriented perpendicular to the  $[11\bar{2}]$  directions, margins were anomalously large on one side (the "super" track) and anomalously small on the other side (the "bad" track). These three-fold symmetric margins have considerably complicated the design of ion-implanted devices. Initially it was believed that magnetocrystalline anisotropy caused the anisotropic behavior<sup>1</sup>, but later it was realized that anisotropic magnetostriction was the cause.<sup>3, 4</sup> Kryder and Saunders<sup>4</sup> proposed that the anisotropic effects could be eliminated by growing materials with negative and isotropic magnetostriction constants,  $\lambda_{111} = \lambda_{100}$ . Garnet materials with negative magnetostriction coefficients have been reported by Makino et al.<sup>5</sup>; however, the material did not have isotropic magnetostriction ( $\lambda_{111} = -2.3 \times 10^{-6}$  and  $\lambda_{100} = -0.9 \times 10^{-6}$ ). In this letter we report the growth of materials with nearly isotropic magnetostriction, which support submicrometer bubble domains and which have been demonstrated to provide greatly improved propagation margins along the so-called "bad" track.

## Film Development

The development of the isotropic magnetostrictive films described here relies upon the film constituents bismuth and dysprosium. Dysprosium iron garnet has  $\lambda_{100} < \lambda_{111}$  while most other rare-earth iron garnets have  $\lambda_{111} < \lambda_{100}$ . Bismuth does not affect the magnetostriction coefficients greatly, but it does provide the uniaxial anisotropy required for a bubble device. The magnetostriction coefficients of bismuth iron garnet were estimated from data given by Makino et al.<sup>5</sup> and Hansen et al.<sup>6</sup> By careful selection of film constituents it is possible to obtain films in which  $\lambda_{111} = \lambda_{100}$ , and in which the magnetostriction is large and negative as required for ion-implanted devices.

To aid in the film development, a computer program which can be used to estimate the magnetic parameters of films of various compositions was used. The program is based on the assumption that properties of films containing several constituents can be calculated from the known properties of single constituent rare-earth iron garnets. The final film properties are determined by weighting the particular pure iron garnet values of each element by the amount in the mixed composition and summing all of the weighted values. This value is then adjusted for exchange, and tetrahedral-octahedral site preference. Computer analysis provided several acceptable compositions from the  $\{\text{DySmLuYBi}\}_3[\text{FeGa}]_5(\text{O})_{12}$  film system that would have isotropic magnetostriction,  $0.5\mu\text{m}$  diameter bubbles, and an acceptable quality factor (Q). Table I shows typical bubble film properties calculated for various film compositions. The dependence of the magnetostriction upon the Bi and Dy is easily seen by noting that as the Bi incorporation increases and the Dy incorporation decreases, both  $\lambda_{111}$  and  $\lambda_{100}$  tend to become less negative, while the difference of the coefficients remains small. Also shown is the dependence of the anisotropy on the Bi incorporation.

### Film Growth and Characterization

After identifying attractive film compositions by computer analysis,  $\{\text{DySmLuYBi}\}_3[\text{FeGa}]_5(\text{O})_{12}$  garnet films were grown by liquid phase epitaxy. Films were grown with a  $60^\circ\text{C}$  to  $70^\circ\text{C}$  super cooling at  $860^\circ\text{C}$  to  $900^\circ\text{C}$  with a rotation of 40 to 100 RPM. Two different GGG substrates were used to grow the bubble films;  $[111]$  oriented films were used for devices and  $[100]$  oriented films were used for measurements of  $\lambda_{100}$ .

Film thickness was measured by interferometry, while magnetization and length-parameters( $l$ ) were determined from bubble collapse and domain stripwidth measurements. Ferromagnetic resonance was used to determine the anisotropy and hence the Q of the films. A previously described ferromagnetic resonance apparatus was used to measure the magnetostriction constants.<sup>7</sup> To determine  $\lambda_{111}$  and  $\lambda_{100}$ , both  $[111]$  and  $[100]$  oriented films were used.

## Experimental Results

All of the film properties are strongly dependent on growth temperature. Although  $0.35\mu\text{m}$  diameter bubbles were observed and briefly studied, a  $0.5\mu\text{m}$  diameter bubble material with nearly isotropic magnetostriction was desired for use in devices. Optimal films had a characteristic length of  $0.54\mu\text{m}$ , a magnetization of 1060G, and an anisotropy field of 1900G providing a Q of 1.85. The damping of these films was large, but not unusable;  $\alpha$  was measured by FMR to be 0.11. The magnetostriction at the isotropy point was  $-2.6 \times 10^{-6}$  and could be varied by 20% by adjusting the growth temperature. Figure 1 shows the effect that the growth temperature has on the magnetostriction of the films. This variation can be attributed to changes in the amount of bismuth and dysprosium incorporated into the films.

Ion implanted contiguous disk propagation patterns with  $2.5\mu\text{m}$  period were fabricated on a film in which  $\lambda_{100} = -1.76 \times 10^{-6}$ ,  $\lambda_{111} = -0.80 \times 10^{-6}$ ,  $4\pi M_s = 1040\text{G}$ , and  $Q = 2.02$ . The low value of the magnetostriction coefficients is due to the relatively large amounts of bismuth, lutetium, and yttrium in the film, all of which have small magnetostriction coefficients. Fig. 2 shows margins for tracks oriented in the conventionally defined "good" and "bad" directions. Both margins were made for propagation completely around the loops at low frequency; thus, the "bad" track margin is actually the intersection of the "super" and "bad" track margins. The propagation margins are seen to be about 15% for both the "good" and the "bad" orientations. The minimum drive field of the normally "bad" track orientation (35 Oe) is actually lower than that of the "good" track (45 Oe). This is due to the fact that  $\lambda_{100} < \lambda_{111}$  in the film used. We believe that by using films with more perfect isotropy of magnetostriction, the margins could be made to match more perfectly and thus that the relation between the two margins can be controlled by varying the magnetostriction coefficients. We plan to verify this by fabricating devices on films having more perfect isotropy as indicated in Fig. 1 in the near future. It is noted that, even with the limited degree of isotropy achieved in the material used for the data of

Fig. 2, the two margins overlap at 60 Oe. drive field by 12%, a value which is large compared to previous results in much larger bubble size devices.

### Conclusion

The operating margins in Fig. 2 clearly show that the "bad" track propagation can be improved by the use of films having more nearly isotropic magnetostriction. The reason that the "bad" track orientation has better margins than the "good" track orientation in this film is believed to be due to the fact that  $\lambda_{100}$  is more negative than  $\lambda_{111}$  which, as indicated in Eq. 1 of Kryder and Saunders paper<sup>4</sup>, would reverse the sign of the three-fold anisotropy.

This research was supported by the Air Force Office of Scientific Research under grant 84-0341, the National Science Foundation under grant ECS-8307261, and the National Research and Resource Facility for Submicron Structures under NSF grant ECS-8200312.



Composition	$4\pi M_s$ [G]	$\Delta a_0$ [Å]	$\lambda_{111}$ [ $10^{-6}$ ]	$\lambda_{100}$ [ $10^{-6}$ ]	$\lambda_{111}-\lambda_{100}$ [ $10^{-6}$ ]	$K_g$	$K_s$ [ $10^{-4}$ erg/cm <sup>3</sup> ]	$K_u$
$\text{Bi}_{0.20}\text{Dy}_{1.00}\text{Sm}_{0.20}\text{Lu}_{0.90}\text{Y}_{0.70}\text{Fe}_{5.00}\text{Ga}_{0.00}\text{O}_{12}$	1340	0.001	-2.78	-3.00	0.22	6.4	0.14	6.5
$\text{Bi}_{0.30}\text{Dy}_{0.80}\text{Sm}_{0.20}\text{Lu}_{1.10}\text{Y}_{0.60}\text{Fe}_{4.90}\text{Ga}_{0.10}\text{O}_{12}$	1300	0.000	-1.85	-1.83	-0.02	8.4	0.01	8.4
$\text{Bi}_{0.40}\text{Dy}_{0.60}\text{Sm}_{0.20}\text{Lu}_{1.20}\text{Y}_{0.60}\text{Fe}_{4.80}\text{Ga}_{0.20}\text{O}_{12}$	1270	0.002	-1.00	-0.78	-0.23	10.2	0.06	10.2
$\text{Bi}_{0.40}\text{Dy}_{0.70}\text{Sm}_{0.20}\text{Lu}_{1.30}\text{Y}_{0.40}\text{Fe}_{4.84}\text{Ga}_{0.16}\text{O}_{12}$	1280	0.000	-1.13	-1.14	0.00	10.3	0.01	10.4
$\text{Bi}_{0.50}\text{Dy}_{0.60}\text{Sm}_{0.20}\text{Lu}_{1.50}\text{Y}_{0.20}\text{Fe}_{4.78}\text{Ga}_{0.22}\text{O}_{12}$	1260	0.001	-0.46	-0.48	0.02	12.3	0.01	12.3

Table 1: Calculated Properties of  $\{\text{DySmLuYBi}\}_3[\text{FeGa}]_5(\text{O})_{12}$  films with isotropic magnetostriction

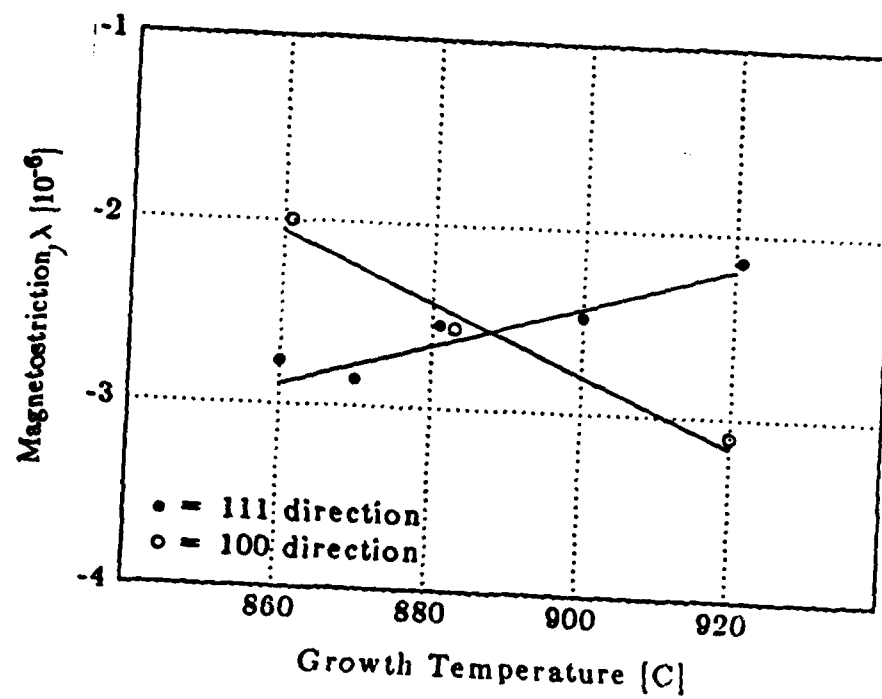


Figure 1: Magnetostriction Dependence on Growth Temperature

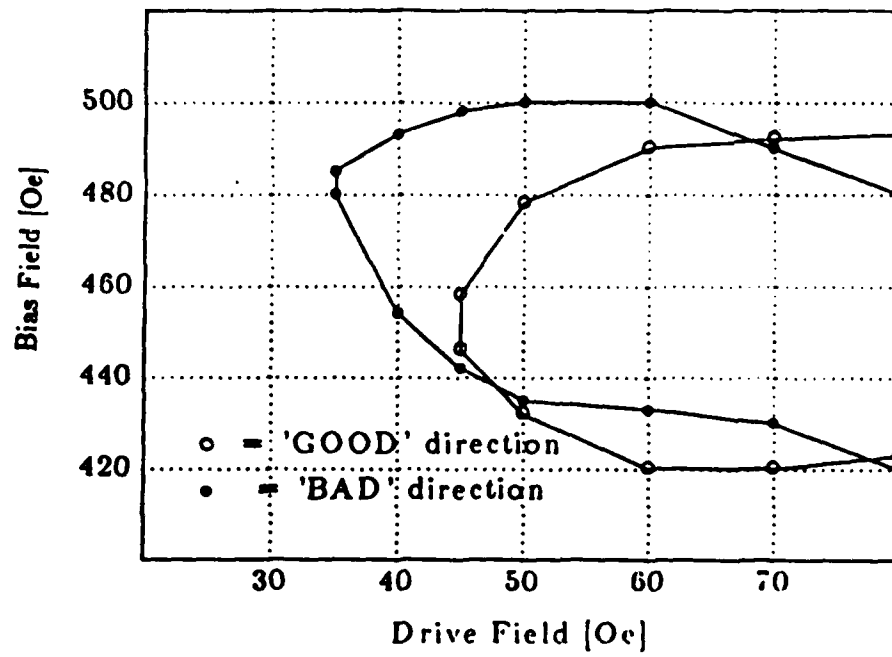


Figure 2: Margins of 2.5 $\mu$ m period IICD pattern

## REFERENCES

- <sup>1</sup> Y.S. Lin, G.S. Almasi, D.B. Dove, G.E. Keefe, and C.C. Shir, "Orientation dependence of propagation margin of 1- $\mu$ m bubble contiguous-disk devices -- Clues and Cures", *J. of Appl. Phys.*, 50, 2258, (1979).
- <sup>2</sup> R. Wolfe, T.J. Nelson, "Crystal Symmetry Effects in Ion-Implanted Propagation Patterns for Magnetic bubbles: 'Roof-Top' Designs", *I.E.E.E. Trans. Magnet.*, MAG-15, 1323, (1979).
- <sup>3</sup> A. Hubert, "Domain Wall Phenomenon in Bubble Propagation Layers", *J. of Magnetism and Magnetic Materials*, 35, 249, (1983).
- <sup>4</sup> M.H. Kryder, D.A. Saunders, "The Effects of Stress Relaxation and Anisotropic Magnetostriction On Charged Walls in Ion-Implanted Garnets", *I.E.E.E. Trans. Magnet.*, MAG-19, 1817, (1983).
- <sup>5</sup> H. Makino, O. Okada, and Y. Hidaka, "Dysprosium Containing Bubble Garnet Composition for Ion-Implanted Contiguous Disk Devices", *J. Appl. Phys.*, 55, 2551, (1984).
- <sup>6</sup> P. Hansen, K. Witter, and W. Tolksdorf, "Magnetic and Magneto-optic Properties of Lead- and Bismuth-Substituted Yttrium Iron Garnet", *Phys. Rev.*, B27, 6608, (1983).
- <sup>7</sup> X. Wang, C.S. Krafft, M.H. Kryder, "Measurement of Magnetocrystalline Anisotropy Field and Magnetostriction Coefficient in Garnet Films", *I.E.E.E. Trans. Magnet.*, MAG-18, 1295, (1982).

### List of Figures

- |                  |  |          |
|------------------|--|----------|
| <b>Figure 1:</b> | <b>Magnetostriction Dependence on Growth Temperature</b>   | <b>6</b> |
| <b>Figure 2:</b> | <b>Margins of 2.5<math>\mu</math>m period IICD pattern</b> | <b>7</b> |

## List of Tables

<b>Table I:</b>	Calculated properties of $\{\text{DySmLuYBi}\}_3 [\text{FeGa}]_5 (\text{O})_{12}$ films with	5
	isotropic magnetostriction	

## ANALYSIS AND DESIGN OF ION-IMPLANTED BUBBLE MEMEORY DEVICES

J. R. Wullert II\* and M. H. Kryder, Magnetics Technology Center, Dept. of Electrical and Computer Engineering, Carnegie Mellon University, Pittsburgh, PA 15213

Ion-implanted contiguous disk bubble memory circuits, designed and fabricated at Bell Laboratories, Murray Hill, NJ, have been investigated. Quasi-static testing has provided information about both the operational bias field ranges and the exact failure modes. This information is then used to design new device elements.

A variety of major loop lay-outs were investigated and two local configurations found to severely limit bias field margins are discussed. The generation process, using a hairpin nucleator, was tested and several interesting failure modes were uncovered. Propagation on four different minor loop paths was observed and each was found to have characteristic failure modes. Again new designs are presented. The transfer processes, both into and out of the minor loops, were investigated non-quasi-staticly as heating in the area of the transfer gate was found to reduce high bias margins at low frequencies. Even at 25 kilohertz, heating was still suspected of limiting margins and design modifications to correct for this and other observed failure mechanisms are presented.

In this way, the operation of each of these functions has been observed and analyzed and the results of these analyses were used to design improved bubble memory elements.

This work has been supported by the Air Force Office of Scientific Research under grant 84-0341 and the National Science Foundation under grant ECS-8307261.

PACS numbers: 85.70Ge 85.70Kh, 85.70Qn

## Introduction

Ion-implanted bubble memories, rather than the hybrids discussed in [1], have been shown to work [2] [3]. In this investigation, quasi-static testing and visual verification have been used to accurately identify failure modes and bias margins for the generation, propagation, and transfer processes for the devices used in [3]: four micron period ion-implanted structures fabricated at Bell Laboratories. This information is then used to design new device elements.

## Generation

In testing generation, bubbles were generated every other drive field cycle to correspond with the minor loop spacing on the major loop and generation was defined to include propagation to the third cusp from the generator. The current pulse was a 50ns triangle with amplitudes from 165 to 250 mA. Two typical generators are shown in Figs. 1A and 1B.

The bias margin for the generator in Fig. 1A is shown in Fig. 2, with the margins for the rest of the functions. The margin for this generator is rather wide: near 50 Oersteds. At the lower bias limit, near 412 Oe, the observed failure showed bubbles skipping out of the generator cusp during the generation cycle.

With generators like Fig. 1B, the lower limit was about 420 Oe. The failure was one of double generation: bubbles were generated both in the cusp and also away from the propagation path. Bubbles generated away from the path were attracted by the charged wall to the path and then represented errors.

At higher bias fields, on some circuits, the current pulse could not overcome the bias field. Raising the peak current would usually not increase this limit, shown in Fig. 2. This type of failure would occur on the generators with the conductor pushed into the cusp which, as noted in [3], required lower currents. Circuits which did not have the conductor pushed into the cusp needed larger currents and the high bias limit would



be below that shown in Fig. 2 by about 10 Oe. At this limit, the pulse that created a bubble would collapse the bubble generated by a previous pulse. Raising the peak current here would actually lower the high bias limit as a larger collapse field was produced.

The generator shown in Fig. 1C shows changes expected to eliminate the above failure modes. The propagation path period is extended to reduce the possibility of bubbles skipping or collapsing. The conductor loop is spread away from the propagation path to prevent double-generation and is pushed well into the cusp to reduce the required current.

### Minor Loop Propagation

Each of the four different minor loop structures that were tested, shown in Fig. 3, had its own special failure modes. Margins for the four patterns are shown in Table I.

The first of the two low bias failures seen on the snakes resulted in bubbles "marching double-time" or moving two cusps during each cycle. The failure, observed at 0.2 Hz, went as follows: When the drive field was pointed into the cusp, the bubble would stripe out under the charged wall. This short stripe would fall into the next cusp and contract into a bubble as the field turned parallel to the loop. The drive field would then carry the bubble into the next cusp normally. This failure is probably a result of the fact that adjacent minor loops had peaks facing cusps, offering a good place for charged walls to bridge.

The second low bias failure of the snakes was also seen on the contiguous disks: bubbles jumping from loop to loop at the end away from the major loop. In this failure, the bubbles would go two thirds of the way around the end before jumping. It is believed that this failure is a result of the extended charged walls that have been observed in the large unimplanted regions, using Bitter technique [4].

The triangular loops exhibited a directionally dependent low bias failure. On the side

of the path where they slid up the slope into the next cusp, bubbles would stripe to that cusp prematurely. At the same bias fields, near 430 Oe, bubbles on the other side would propagate normally. This failure was not influenced by the orientation of the paths, as seen in Tbl. I, but just by the direction of bubble motion with respect to the triangles.

The most common high bias failure, bubble collapse, was found to occur at peaks and was more likely at points of triangles. Some snake loops also exhibited a high bias double-time failure where bubbles would roll through every other cusp. This failure was found to occur on tracks that had unimplanted regions less than 2.5 microns wide.

On the far right of Fig. 3 is a propagation path that might eliminate the observed failure modes. It allows propagation only in one direction, but keeps bubbles pressed against a flat side. It is set up so that neighboring loops are peak to peak and has rounded edges rather than points. It also has a shortened path around the top end which might trap the bubble before it can jump.

### Major Loop Propagation

Two areas of the major loops that were found to be weak are shown in Figs. 4A and 4B. Fig. 4A is a backward turn that had depressed high bias limits. The 330° turn in Fig. 4B, which took the bubble onto or off the minor loop side of the major loop, exhibited sticking problems at low drive fields.

Since the backward turn looks like a 'bad' track [5], bubble collapse at reduced bias fields is not surprising. Using films that exhibit more isotropic propagation [6] this type of failure would not be expected to be a problem.

On the 330° turns, shown in Fig. 4B, bubbles stuck in the cusp after the turn. As seen in Fig. 2, the climb of the low bias margin from 414 Oe at 50 Oe drive to 438 Oe at 35 Oe is due to this failure. This failure is presumed to be caused by the charged wall, which extends into the large implanted region, simply skipping over this cusp

when it makes the sharp corner. Since this failure did not occur on  $270^\circ$  turns, it might be avoided by using the turn shown in Fig. 4C, which breaks the  $330^\circ$  into a  $270^\circ$  and a  $60^\circ$  turn.

### Transfer Into and Out of the Minor Loops

Initial testing of the transfer process, using the gate shown in Fig. 5A, was performed at 1 Hz. The resulting high bias margins were depressed below what was expected. This was attributed to heating in the area of the gate, caused by the long current pulse. Further testing was performed at 25 kHz to avoid this problem.

Transfer into the minor loops had the smallest of the bias margins, as seen in Fig. 2. The low bias failure was poor propagation in the major loop, before the current pulse. The failure mode at high bias fields was collapse in the gate during transfer. This seemed to indicate that local heating was reducing the bubble collapse field. This was supported by the high bias limit decreasing with increasing current, above a certain current value. This value varied from chip to chip, from 45 to 55 mA. The lowest required currents coincided with chips on which the mask alignment was such that the transfer conductor was pushed closer to the major loop.

The leading edge phase margin was found to be rather narrow, as at higher bias fields bubbles tended to stay in the major loop rather than transfer properly. Here, wider phase margins were observed on chips that had the conductor pushed toward the major loop.

Transfer Out margins, shown in Fig. 2, are slightly wider than Transfer In, although they close below 45 Oe drive. The reason for the raised margins is again probably related to heating: Transfer Out required only 25 to 30 mA to operate and so the gates ran cooler. At lower drive fields, bubbles tended to stay in the minor loops rather than transfer. The effect of this failure is obvious in the steep slope of the low bias limit from 40 to 45 Oe drive. This failure might be eliminated by locating the conductor closer to the major loop, holding the bubble closer to the charged wall.

Having observed the failure modes in the transfer processes, it is not too difficult to propose changes to improve their operation. By widening the conductor to reduce heating and by moving the conductor turn closer to the major loop to better position the bubble during transfer and to reduce the required currents, and hence heating, one arrives at the modified transfer gate design shown in Figure 5B.

### Conclusion

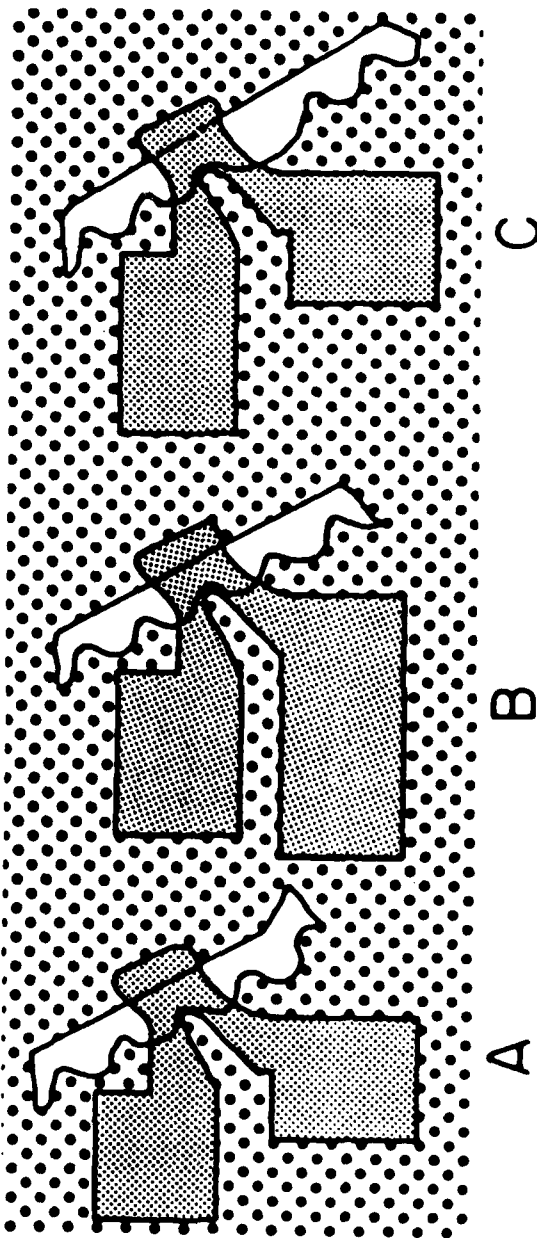
Referring to Fig. 2 one last time, it is apparent that a reasonable overlap of bias margins exists for these functions. By testing these devices at quasi-static frequencies, both the high and low bias failure modes were readily observed. Failures such as the "double-time" minor loop failures or the double generate mechanism could be discovered only through such close observation. In the major loop, where many possible failure spots exist, this observation lead to finding two specific turns that limit the margins. In cases like transfer, where heating makes quasi-static operation impossible, observation of the bubble before and after the event also produced information about the failure mechanisms. Based upon the observed failure mechanisms, modified designs have been proposed.

### References

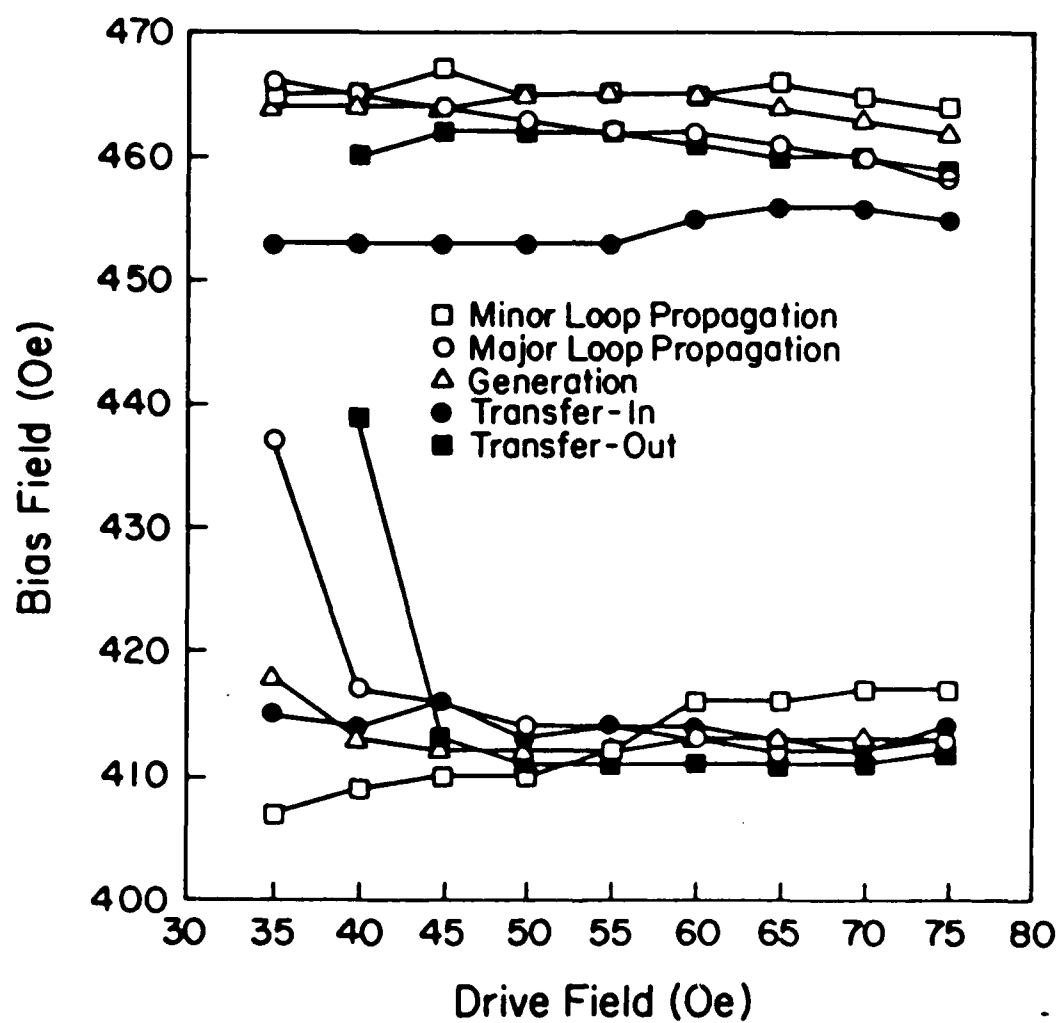
1. \*Present Address: Bell Communications Research, Red Bank NJ.
2. Y. Sugita, R. Suzuki, T. Ikeda, T. Takeuchi, N. Kodama, M. Takeshita, R. Imura, T. Satoh, H. Umezaki, and N. Koyama, IEEE Trans. Magnet. MAG-22, 239 (1986).
3. P. I. Bonyhard, F. B. Hagedorn, D. T. Ekholm, D. J. Muehlner, T. J. Nelson, and B. J. Roman, IEEE Trans. Magnet. MAG-18, 737 (1982).
4. T. J. Nelson, V. J. Fratello, D. J. Muehlner, B. J. Roman, and S. E. G. Slusky, IEEE Trans. Magnet. MAG-22, 93 (1986).
5. S. Jo, Private Communication.
6. R. Wolfe and T. J. Nelson, IEEE Trans. Magnet. MAG-15, 1323 (1979).
7. S. Jo and M. H. Kryder, IEEE Trans. Magnet. MAG-22, (1986).

### List of Figures

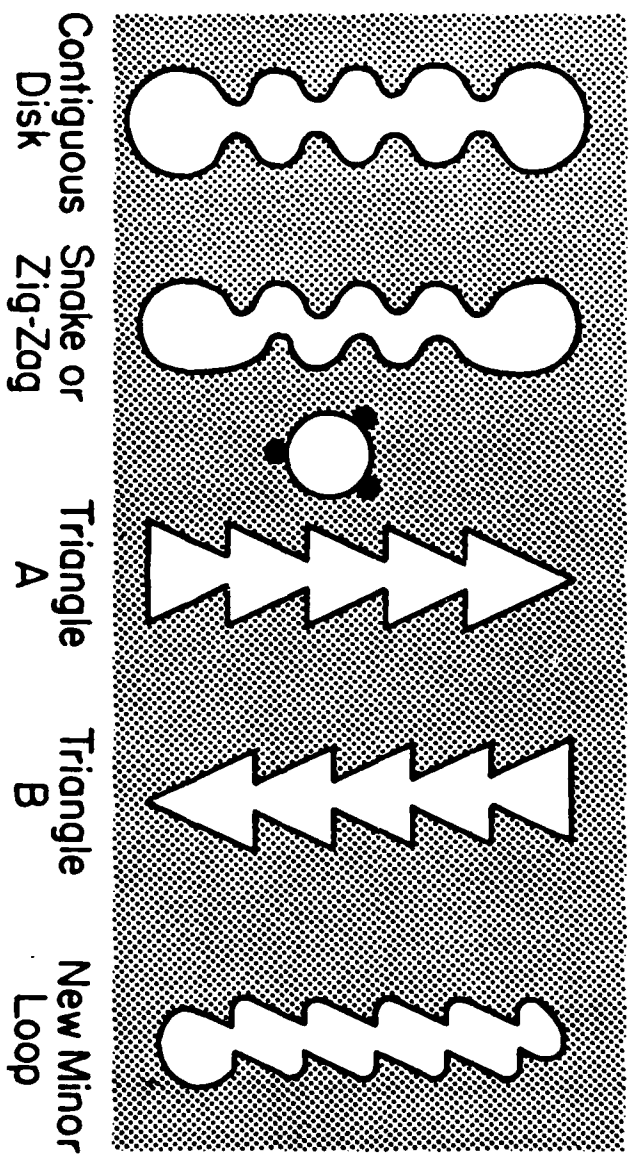
- Figure 1: Bubble generators. A-B: Tested designs. C: Modified design.
- Figure 2: Quasi-static margins for all functions. (Transfer at 25 kHz.)
- Figure 3. Minor loop propagation. 4 tested paths and modified design.
- Figure 4. Major loop propagation failure points. A: Backward turn. B: 330° turn. C: Modified 330° turn.
- Figure 5. Trapping transfer gate. A: Tested design B: Modified design

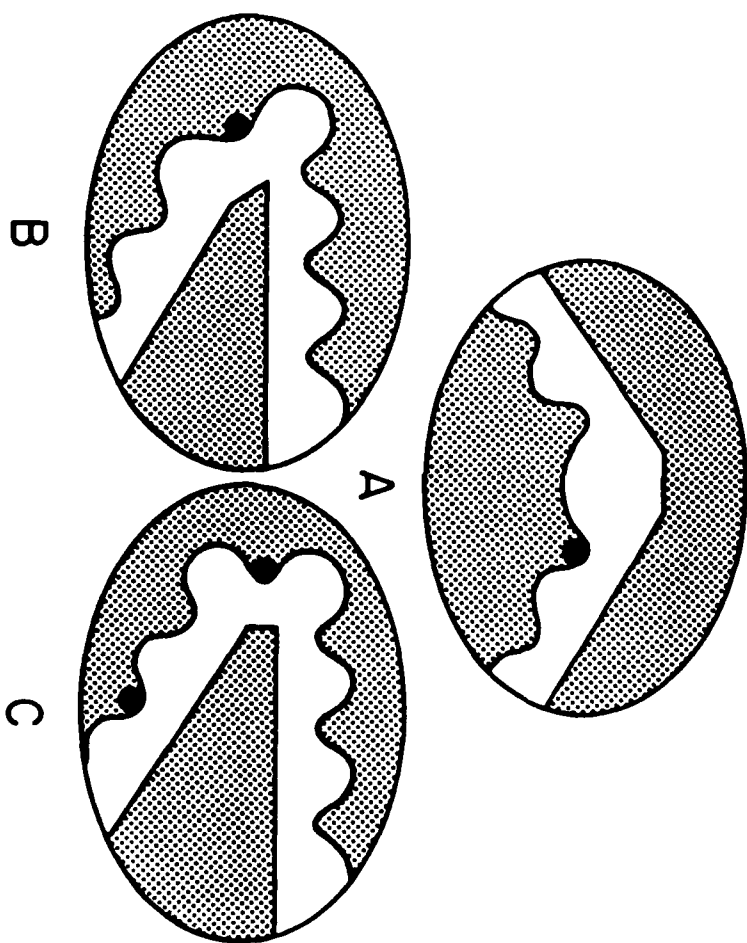


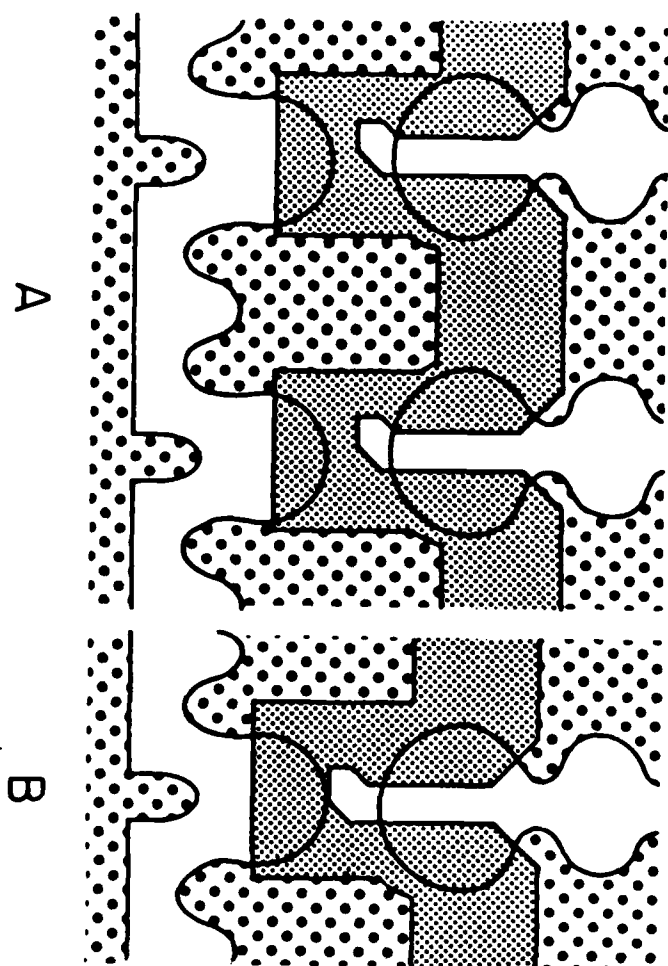
# Overall Bias Margin











## Minor Loop Propagation Bias Margins

**Table I**

$H_{rot}$	Contiguous Disk	Snake or Zig-Zag	Triangle A	Triangle B
40	450-477	421-456	434-479	424-485
50	426-473	416-449	427-478	432-480
60	416-466	406-435	425-479	431-465

## THE IRRADIATION EFFECTS OF ION IMPLANTATION ON MAGNETIC GARNETS

A.M. GUZMAN, C.L. BAUER, J.-F. SILVAIN and M.H. KRYDER

*Carnegie-Mellon University, Pittsburgh, Pennsylvania, 15213 USA*

The microstructure of epitaxially grown garnets, used for magnetic bubble memory devices, has been examined prior and subsequent to implantation with high-energy ions by transmission electron microscopy, incorporating a special cross-section technique. In this particular investigation, thin films of  $(\text{SmY}\text{Gd}\text{Tm})_3\text{Ga}_5\text{Fe}_4\text{O}_{12}$  have been produced by liquid phase epitaxy on (111) substrates of gadolinium-gallium garnet and subsequently exposed to various doses of oxygen and/or deuterium ions. At moderate implantation doses ( $5 \times 10^{15} \text{ D}_2^+/\text{cm}^2$  and/or  $1 \times 10^{16} \text{ O}^+/\text{cm}^2$ ), magnetic properties are favorably modified, whereas, at larger doses, isolated amorphous regions nucleate and grow into a continuous layer, thereby degrading desirable magnetic properties. Implantation-induced changes of the garnet crystal structure near the unimplanted/implanted boundary are described. Relationships between these microstructural features and concomitant magnetic properties are suggested.

## 1. Introduction

The explosion in magnetic information technology has been precipitated by development of devices with extremely high information storage capacity and rapid access and transfer times. Contiguous disk magnetic bubble devices which are fabricated in magnetic garnets, produced by liquid-phase epitaxy by using ion implantation to define bubble propagation patterns represent one class of such devices. Ion implantation produces compressive stresses in implanted regions of the surface layer. The stresses in turn, induce the desired magnetic anisotropy via magnetostriction. An ion-implanted garnet is shown schematically in fig. 1. An implantation mask serves to delineate the unimplanted/implanted regions. In the implanted areas there is an in-plane magnetization  $M$ . As there is a discontinuity in  $M$  at the unimplanted/implanted boundary, magnetically charged walls are formed, as shown in fig. 1. Magnetic bubbles are then generated, attracted to the edge of the implanted patterns and to the charged walls. When an

external rotating in-plane magnetic field is applied, the charged walls move around the implanted patterns, and thus propagate the underlying bubbles transferring bits of binary information at a rate equivalent to the frequency of the applied field (about 100 kHz). The thicknesses given in fig. 1 are for a  $1 \mu\text{m}$  diameter bubble device. This type of solid-state device is highly reliable and resistant to extremes in environmental conditions, such as temperature, vibration and radiation [1].

As demand for higher storage capacities and more rapid access and transfer of information increases, the bubble propagation patterns defined by ion implantation must be reduced in size and carefully controlled. The effect of ion implantation is to generate isolated vacancies and interstitials, as well as cascades of displaced atoms, which produce an expansion of the lattice and corresponding changes in magnetic anisotropy. Gradient stresses resulting from the implantation process at the edge of an ion implantation region in a magnetic garnet film have been reported in a previous paper [2]. Because of perpendicular and shearing stresses, the anisotropy under the edge of the implantation mask was found to favor planar magnetization, especially for materials having anisotropic magnetostriction. For similar reasons, the anisotropy in the implanted region near the mask edge was found to favor perpendicular magnetization. Fig. 2 shows the magnetization distribution (indicated by the arrow orientation) near the squared edge of a mask of uniform thickness. In this example, the implanted material is assumed to be magnetostrictively isotropic. In addition, the anisotropy distribution near a beveled mask edge (fig. 3) indicates that a charged wall may not be well defined along such an edge. Therefore, it is important to examine the structure of garnet in the implanted/unimplanted zones in order to determine if the desired

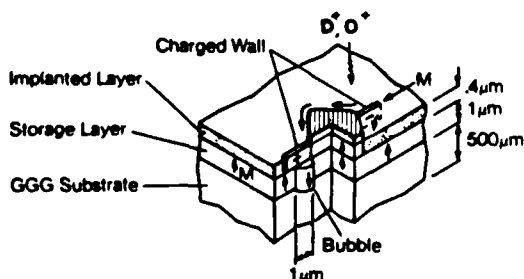


Fig. 1. View of an ion implanted magnetic garnet thin film epitaxially deposited on a gadolinium-gallium garnet (GGG) substrate.

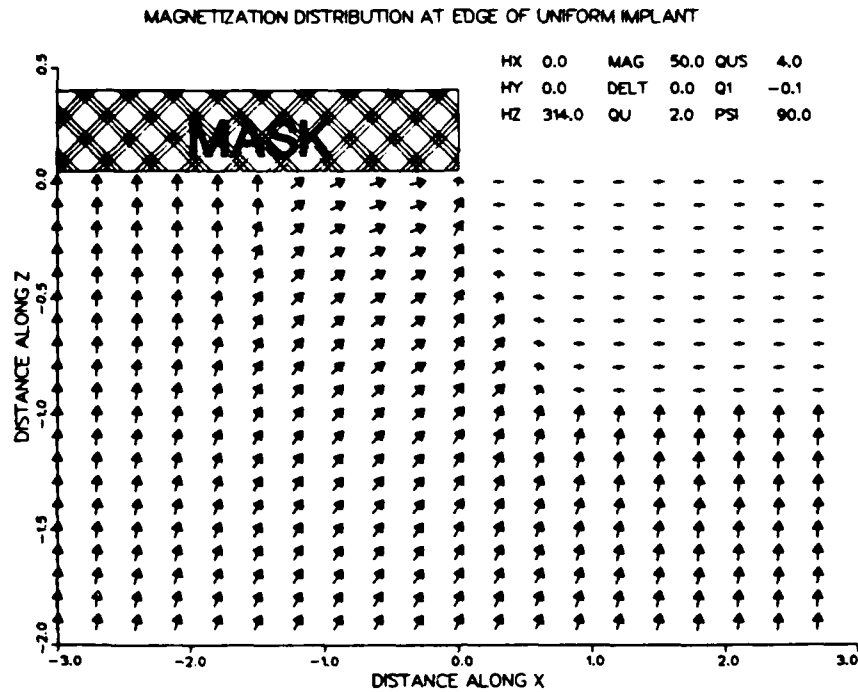


Fig. 2. Distribution of the magnetization at the edge of an abrupt mask for a uniform implant in a magnetostrictively isotropic garnet film. (The mask's edge extends along the y-axis.)

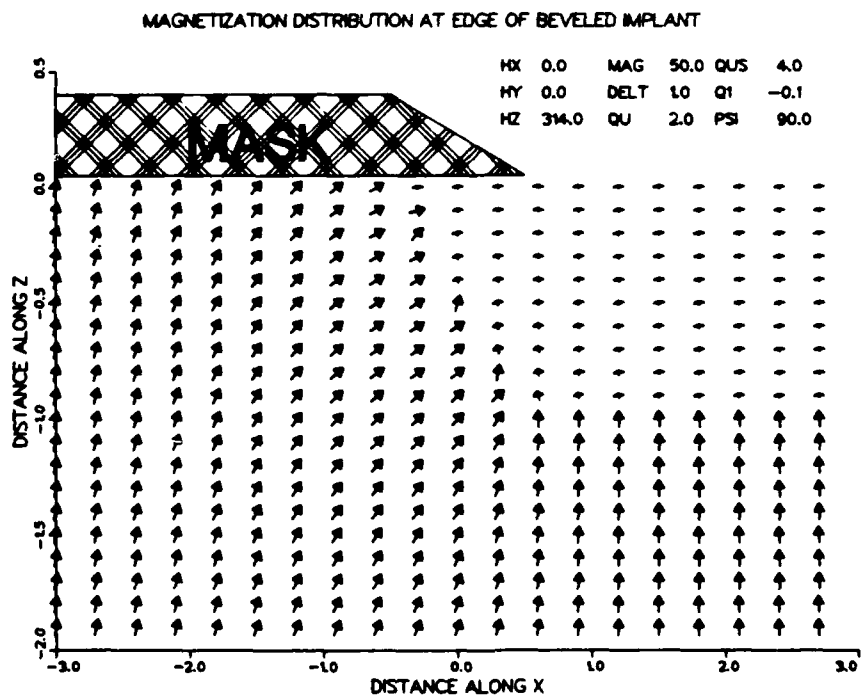


Fig. 3. Distribution of the magnetization at the edge of a beveled mask in a magnetostrictively isotropic garnet film.

implantation levels have actually been achieved. Depth and lateral profiles of implantation patterns must be resolved over distances less than one micrometer [3].

The purpose of this article is to review the results of previous investigations on the implantation induced structural changes in magnetic garnet [4-6] as well as to present results on the examination of the microstructure of the regions near the edge of the implantation mask. Depth profiles of implanted patterns were determined quantitatively by transmission electron microscopy (TEM), incorporating a special cross-section technique.

## 2. Experimental details

Films of  $(\text{SmYGDm})_3\text{Ga}_{0.4}\text{Fe}_{4.6}\text{O}_{12}$  garnet, ranging from 0.6 to 1.1  $\mu\text{m}$  in thickness, are produced by liquid-phase epitaxy (LPE) on (111) gadolinium-gallium garnet (GGG) substrates and subsequently implanted at ambient temperature with ions of deuterium at 60 or 88 keV and doses ranging from  $0.50$  to  $4.5 \times 10^{16}$   $\text{D}_2^+/\text{cm}^2$  and with ions of oxygen at 100 or 110 keV and doses ranging from  $0.95$  to  $8.6 \times 10^{14}$   $\text{O}^+/\text{cm}^2$ . Following ion implantation, specimens are prepared for examination parallel to the implanted surface by TEM. The sample preparation technique has been reported elsewhere [6].

## 3. Experimental results and discussion

Examination of the implanted samples by TEM revealed that substantial changes of the garnet microstructure occurred as a consequence of ion implantation. Results of our previous investigation are summarized at the beginning of this section. The evolution from crystalline to amorphous states, as well as crystal regrowth from the amorphous phase are briefly discussed. Subsequently, recent results on the examination of unimplanted/implanted lateral boundaries are presented and interpreted in view of our current understanding of radiation damage processes in garnets.

Typical results are presented in fig. 4, wherein bright-field images perpendicular to the implanted surface of garnet; i.e., in the (110) plane, following implantation with (a) 1, (b) 3, (c) 6, (d) 9 times a standard dose of  $0.50 \times 10^{16}$   $\text{D}_2^+/\text{cm}^2$  at 60 keV and then  $0.95 \times 10^{14}$   $\text{O}^+/\text{cm}^2$  at 110 keV are pictured. In addition to the LPE/GGG interface, a faint band, corresponding to the implantation profile for deuterium and terminating at about 450 nm below the implanted surface, is visible in fig. 4a. In this case, however, the oxygen profile, estimated to extend about 150 nm below the implanted surface, is too faint to be easily detected. For implantation conditions corresponding to  $3 \times$  of the standard dose, localized amorphous regions are

produced by the implantation process in an otherwise monocrystalline matrix, as pictured in Fig. 4b. In this case, a mixture of amorphous particles, about 10 nm in diameter, in a crystalline matrix is observed in the oxygen-plus-deuterium implanted zone, extending about 150 nm below the implanted surface, whereas a fully monocrystalline structure is observed in the deuterium implanted and unimplanted zones, as verified by the corresponding (inserted) micro-microdiffraction patterns. For implantation conditions corresponding to  $6 \times$  of standard dose, the oxygen-plus-deuterium implanted zone is transformed into an entirely amorphous band, as pictured in fig. 4c and verified by the sole presence of halo rings in the (inserted) micro-microdiffraction pattern, whereas the deuterium implanted region remains entirely crystalline, as verified by the (inserted) monocrystalline micro-microdiffraction pattern. The LPE/GGG interface is also clearly visible in this figure. For implantation conditions corresponding to  $9 \times$  of the standard dose, a completely amorphous structure is produced in the oxygen-plus-deuterium implanted band, extending about 200 nm below the implanted surface, as pictured in fig. 4d. The crystalline deuterium implanted band, extending about 450 nm below the implanted surface, is also visible. In this case, the width of the amorphous layer has increased by 20 nm (about 10%) compared to the layer produced by a dose of  $6 \times$ .

Reversion of the amorphous region, produced by ion implantation, to the crystalline state was investigated in a specimen implanted with deuterium and then oxygen to  $9 \times$  of the standard dose as a function of in situ annealing. Significant structural changes are not observed following annealing for 30 min at  $300^\circ\text{C}$  or less. However, annealing at higher temperatures produces noticeable structural changes, as revealed in Fig. 5, wherein bright-field images perpendicular to the implanted surface, following annealing for (a) 5 min at  $350^\circ\text{C}$ , (b) 10 min at  $450^\circ\text{C}$  and (c) 10 min at  $500^\circ\text{C}$  are pictured. Following annealing at  $350^\circ\text{C}$ , small crystallites of about 10 nm in diameter appear. Some of these crystallites may nucleate heterogeneously at the amorphous/crystalline interface, but the majority nucleate homogeneously in the bulk of the amorphous layer. Following annealing at  $450^\circ\text{C}$ , crystal growth is observed, demonstrating that crystallites have nucleated at both the (external) implanted surface and the amorphous/crystalline interface. Following annealing at  $500^\circ\text{C}$ , a polycrystalline region, confined to the original oxygen-plus-deuterium implanted zone, is produced. In addition, epitaxial regrowth of about 20 nm has occurred at the polycrystalline/monocrystalline interface (cf. dashed line in fig. 5c).

It may be concluded that the amorphization process involves production of small amorphous particles below the implanted surface, gradual merger of these particles

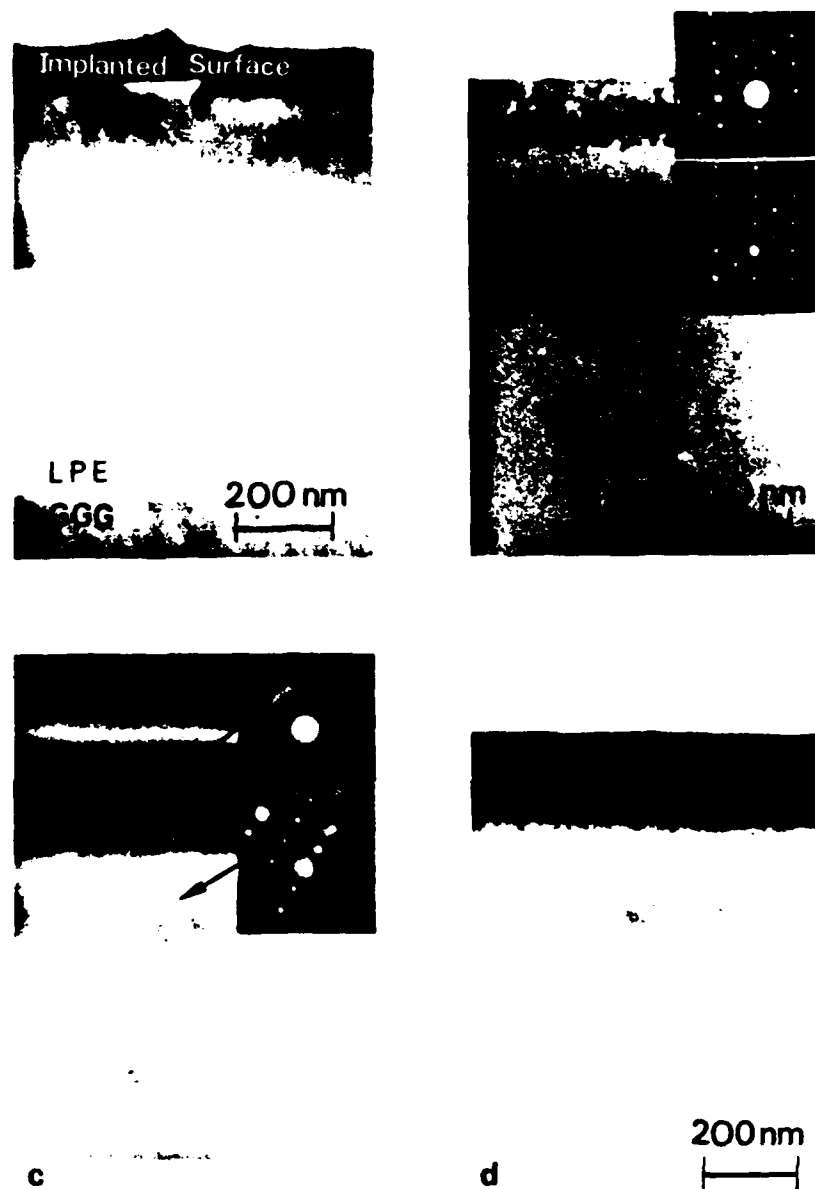


Fig. 4. Bright-field images (with inserted micro-microdiffraction patterns) perpendicular to the implanted surface of garnet following implantation with (a) 1, (b) 3, (c) 6, (d) 9 times a standard dose of  $0.50 \times 10^{16} \text{ D}_2^+/\text{cm}^2$  at 60 keV and then  $0.95 \times 10^{14} \text{ O}^+/\text{cm}^2$  at 110 keV. The implanted surface, deuterium-plus-oxygen and deuterium implanted zones, and LPE/GGG interface are visible.

to form a continuous band, and subsequent expansion of this band to the implanted surface. When the order of the implantation sequence is reversed, however, so that first deuterium is implanted at a dose of  $4.5 \times 10^{16} \text{ D}_2^+/\text{cm}^2$  and then oxygen is implanted at a dose of  $8.6 \times 10^{14} \text{ O}^+/\text{cm}^2$ , another type of crystallization is observed. Namely, by annealing for 10 min at  $300^\circ\text{C}$ , band widths of the amorphous layer decrease from about 200 to 160 nm. This particular process allows

epitaxial regrowth of the crystalline region without detectable change in orientation. Following this stage, crystallization proceeds in an identical manner as for the case of implantation of oxygen followed by deuterium.

Although processes associated with implantation and subsequent annealing of garnet are of fundamental interest, actual bubble memory devices also depend on delineation and precision of implanted patterns. These



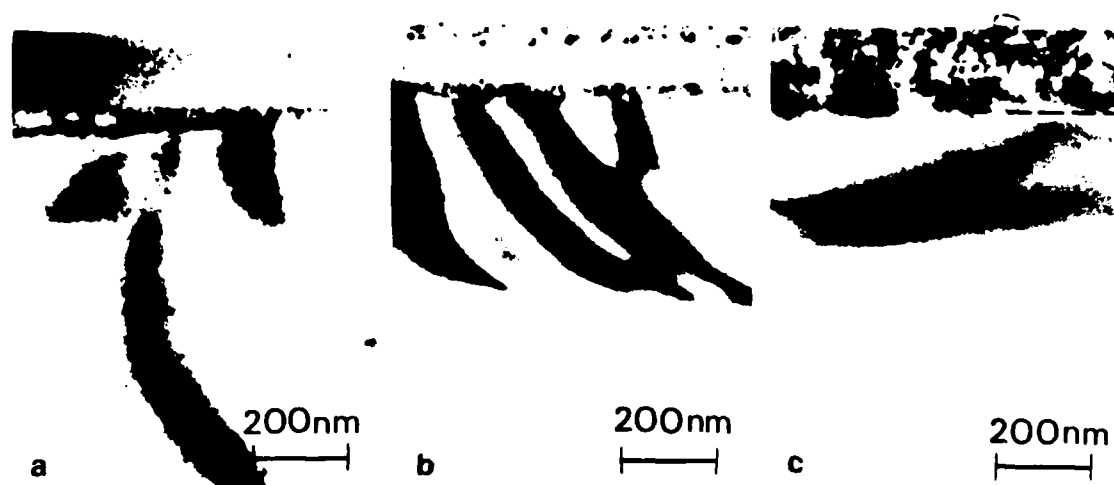


Fig. 5. Bright-field image perpendicular to the implanted surface of garnet following implantation with oxygen at 110 keV and a dose of  $8.6 \times 10^{14} \text{ O}^+/\text{cm}^2$  and then with deuterium at 60 keV and a dose of  $4.5 \times 10^{16} \text{ D}_2^+/\text{cm}^2$  following annealing for (a) 5 min at 350°C, (b) 20 min at 450°C, and (c) 10 min at 500°C.

patterns are delineated by means of an implantation mask, typically made of a photosensitive polymer. The scanning electron micrograph shown in Fig. 6 depicts the cross-section of a masked garnet film where the beveled edge of the mask is apparent. Profiles of the unmasked (left)/masked (right) surface of garnet are

identified in fig. 7, wherein a bright-field image and (inserted) micro-microdiffraction patterns following implantation with deuterium at 88 keV and a dose of  $4.5 \times 10^{16} \text{ D}_2^+/\text{cm}^2$  and then with oxygen at 100 keV and a dose of  $3.0 \times 10^{14} \text{ O}^+/\text{cm}^2$  is pictured. As expected from the previous discussion, the deuterium-

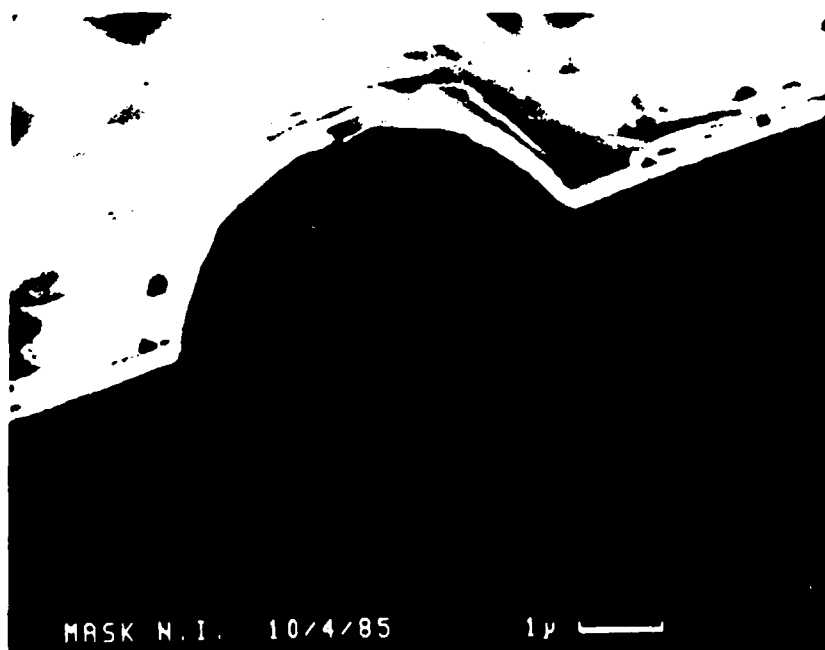


Fig. 6. SEM cross-sectional view of a masked garnet film showing the beveled edge of the implantation mask.

plus-oxygen band is partially amorphous, whereas the deuterium implanted band remains crystalline, as demonstrated by the (inserted) micro-microdiffraction patterns. Of special interest is the fact that lateral termination of the implanted zones is characterized by a gradual transition and termination of the deuterium-plus-oxygen implanted zone does not coincide with that for the deuterium-implanted zone. The LPE/GGG interface is also evident in fig. 7.

The implanted profiles near a mask edge are quantified in fig. 8, wherein (a) a bright-field image perpendicular to the surface of garnet near a mask edge following implantation with deuterium at 88 keV and a dose of  $5.5 \times 10^{16} \text{ D}_2^+/\text{cm}^2$  and then with oxygen at 100 keV and a dose of  $1.0 \times 10^{14} \text{ O}^+/\text{cm}^2$  and (b) schematic representation of the oxygen and deuterium profiles are pictured.

It is not known whether the gradual transition from implanted to unimplanted zones is due to imperfect (beveled) masking or scattering of ions in the LPE layer. Additional research using abrupt implantation masks is currently underway. A comparison of the example presented in fig. 8 and fig. 3, representing the calculated distribution of the magnetization for a beveled mask, suggests that the propagation patterns may not be well defined along the edge of the mask since the implantation profile is not sharply defined. Control of bubble trajectories depends on the abruptness of unimplanted/implanted interfaces. The sloped edge of the implant profile extending a lateral distance of  $1.05 \mu\text{m}$  places a

limit on the scale of the devices. If the scale of corresponding devices is to be reduced below  $1 \mu\text{m}$ , improved delineation of implantation profiles must be achieved.

The amorphization/crystallization processes identified in figs. 4 and 5 demonstrate clearly the effect of ion implantation on the evolution of microstructure as well as delineation of implanted zones by cross-section TEM. These results are relevant to fabrication of ion-implanted contiguous disk bubble devices. The fact that the order of implantation affects the degree of amorphization suggests that order of implantation should also effect, to some extent, operating margins of bubble devices. In particular, results of this investigation suggest that, if large implantation doses are to be used, it would be preferable to implant first with oxygen and then with deuterium rather than in the reverse order, since amorphization, which generally reduces device margins, occurs more easily in a sample first implanted with deuterium. Moreover, results suggest that a tem-

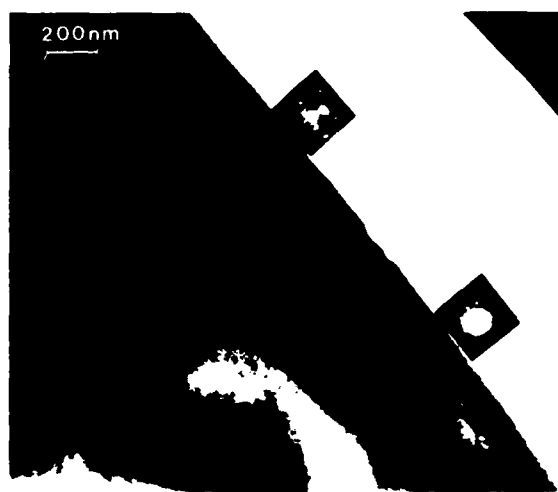


Fig. 7. Bright field image (with inserted micro-microdiffraction patterns) perpendicular to the unmasked (left)/masked (right) surface of garnet following implantation with deuterium at 88 keV and a dose of  $4.5 \times 10^{16} \text{ D}_2^+/\text{cm}^2$  and then with oxygen at 100 keV and a dose of  $3.0 \times 10^{14} \text{ O}^+/\text{cm}^2$ . The implanted surface, deuterium-plus-oxygen and deuterium implanted profiles and the LPE/GGG interface are visible.

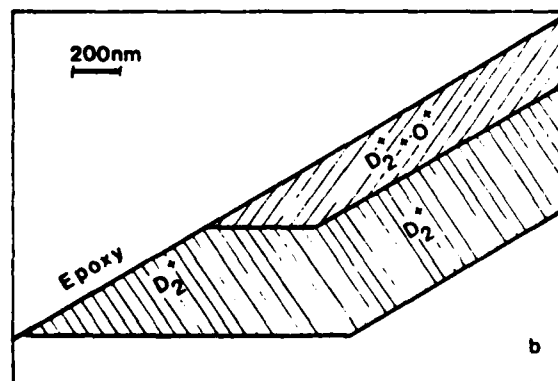
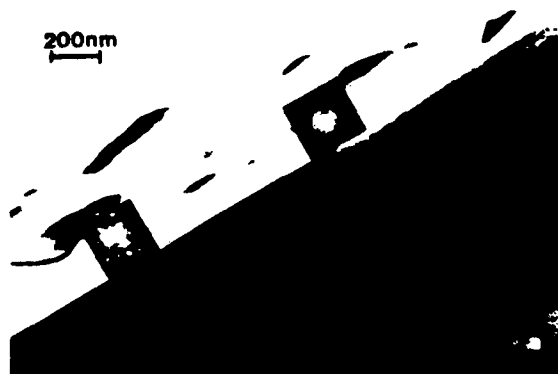


Fig. 8. (a) Bright field image perpendicular to the unmasked (left)/masked (right) surface of garnet following implantation with deuterium at 88 keV and a dose of  $5.5 \times 10^{16} \text{ D}_2^+/\text{cm}^2$  and then with oxygen at 100 keV and a dose of  $1.0 \times 10^{14} \text{ O}^+/\text{cm}^2$  and (b) schematic representation of the oxygen and deuterium implanted profiles.

### III. AMORPHIZATION AND CERAMICS

perature of about 350°C is required to induce reversion of the amorphous regions to the crystalline state. This temperature is in good agreement with observations that characteristics of devices implanted with moderately heavy doses can be improved by annealing at temperatures near 350°C. It is likely that such annealing promotes a reversion of small amorphous regions to the crystalline state [7].

#### 4. Summary

Implantation with ions of deuterium and oxygen, subsequent thermal treatments, and profile delineation at masked/unmasked interface have been investigated in films of  $(\text{SmYGdTm})_3\text{Ga}_{0.4}\text{Fe}_{4.6}\text{O}_{12}$  garnet by transmission electron microscopy, incorporating a special cross-section technique. The amorphization process evolves in four separate stages: (1) an implanted (crystalline) band, delineated by the implantation strain profile is formed at low doses, (2) isolated amorphous regions of about 10 nm in diameter are formed at intermediate doses, (3) these amorphous regions merge to form a continuous band below the implanted surface, and (4) this band expands to the implanted surface at larger doses. Amorphization is caused by implantation with oxygen, but prior implantation with deuterium sensitizes the lattice by increasing the strain. The crystallization process evolves in three separate stages: (1) small crystallites of about 10 nm in size are formed homogeneously during annealing at 350°C, (2) layer crystallites nucleate heterogeneously and grow from the implanted surface and amorphous/monocrystalline in-

terface at 450°C, and (3) these crystallites grow in size until they merge to form a continuous polycrystalline layer at longer annealing times and/or temperatures. Some epitaxial regrowth of the crystalline region into the amorphous region is also observed. Finally, transition from the unimplanted to implanted structure extends over a distance of about 1  $\mu\text{m}$ , which obviously must be reduced if further miniaturization of bubble memory devices is to be achieved.

The authors wish to thank T. Yoshiie for the electron microscopy studies and D. Saunders for his work on stresses and magnetoelastic anisotropies.

Support of this research by the Air Force Office of Scientific Research under Contract 84-0341 is gratefully acknowledged.

#### References

- [1] Kryder, M.H. and A.B. Bortz, *Phys. Today* (December 1984).
- [2] Saunders, D.A. and M.H. Kryder, *J. Appl. Phys.* 57 (1985) 4061.
- [3] T. Omi, C.L. Bauer and M.H. Kryder, *J. Appl. Phys.* 53 (1982) 2528.
- [4] T. Yoshiie, C.L. Bauer and M.H. Kryder, *IEEE Trans. Magn. MAG-19* (1983) 1823.
- [5] A.M. Guzman, T. Yoshiie, C.L. Bauer and M.H. Kryder, *Mat. Res. Soc. Symp. Proc.* vol. 27 (1985) 139.
- [6] T. Yoshiie, C.L. Bauer and M.H. Kryder, *J. Appl. Phys.* 57 (1985) 2155.
- [7] Y.S. Lin, G.S. Almasi and G.E. Keefe, *J. Appl. Phys.* 48 (1978) 5201.

MEASUREMENT OF IMPLANTATION PROFILES IN GARNET  
BY TRANSMISSION ELECTRON MICROSCOPY

J.-F. Silvain, C. L. Bauer, A. M. Guzman  
and M. H. Kryder  
Carnegie-Mellon University, Pittsburgh, Pennsylvania

Abstract

Thin films of  $(\text{SmYbDm})_{0.5}\text{Ga}_{0.4}\text{Fe}_{0.1}\text{O}_{1.2}$  have been produced by liquid phase epitaxy on (111) substrates of gadolinium-gallium garnet, non-uniformly masked, and implanted with ions of deuterium at 88 keV and doses ranging from  $3.5$  to  $5.5 \times 10^{14} \text{ D}^+_2/\text{cm}^2$  and/or with ions of oxygen at 100 keV and doses ranging from  $0.95$  to  $8.6 \times 10^{14} \text{ O}^+/\text{cm}^2$ . These films are subsequently examined by transmission electron microscopy (TEM), incorporating a special cross-section technique, in order to reveal depth penetration (range) in unmasked regions and lateral diffuseness at mask edges for both  $\text{D}^+_2$  and  $\text{O}^+$ , thus providing a direct quantitative measure of implantation profiles. Shape and evolution of these profiles are determined as a function of implantation dose and compared with predicted stress-induced magnetic anisotropy within the implanted zone.

Introduction

In a previous publication, it was demonstrated that structure and concomitant magnetic properties of  $(\text{SmYbDm})_{0.5}\text{Ga}_{0.4}\text{Fe}_{0.1}\text{O}_{1.2}$  garnet are modified favorably at moderate implantation doses ( $5 \times 10^{12} \text{ D}^+_2/\text{cm}^2$  and/or  $1 \times 10^{14} \text{ O}^+/\text{cm}^2$ ), whereas, at larger doses, isolated amorphous regions nucleate and grow into a continuous layer, thereby degrading desirable magnetic properties significantly.<sup>1</sup> Moreover, depth penetration (range) of both  $\text{D}^+_2$  and  $\text{O}^+$  were clearly delineated by transmission electron microscopy (TEM), incorporating a special cross-section technique. Recently, non-uniformly implanted (masked) specimens have been examined, in which depth penetration (range) in unmasked regions and lateral diffuseness at mask edges are clearly delineated, thus providing a direct quantitative measure of two-dimensional implantation profiles.<sup>2</sup> It is necessary to achieve a greater appreciation and eventual control of factors which affect these profiles in order to increase storage density and improve reliability of implanted magnetic bubble memory devices.

The purpose of this investigation is to determine implantation profiles near mask edges, to quantitatively relate depth penetration and lateral diffuseness to imposed experimental conditions, such as energy, dose, and species of implanted ions, and, finally, to compare measured profiles with predicted magnetic properties of  $(\text{SmYbDm})_{0.5}\text{Ga}_{0.4}\text{Fe}_{0.1}\text{O}_{1.2}$ .

Thin films of  $(\text{SmYbDm})_{0.5}\text{Ga}_{0.4}\text{Fe}_{0.1}\text{O}_{1.2}$ , ranging from 0.60 to 1.45  $\mu\text{m}$  in thickness, were produced by liquid-phase epitaxy (LPE) on (111) gadolinium-gallium-garnet (GGG) substrates, masked with alternating parallel strips of photoresist, and implanted at ambient temperature with ions of deuterium at 88 keV and doses ranging from  $3.5$  to  $5.5 \times 10^{14}$   $\text{D}_2^+/ \text{cm}^2$  and/or with ions of oxygen at 100 keV and doses ranging from  $0.95$  to  $8.6 \times 10^{14}$   $\text{O}^+/ \text{cm}^2$ . Specimens were prepared for examination by TEM by bonding two substrates with implanted surfaces in contact with one another (face-to-face) with an epoxy resin and curing the resultant couple under conditions of moderate temperature and pressure. Thin slices were then cut perpendicular to the implanted surfaces and thinned by mechanical grinding to approximately 50  $\mu\text{m}$  followed by further thinning with a Gatan Model 600 ion miller, utilizing a collimated beam of argon ions accelerated by 6 kV. The thinned regions were subsequently examined in a JEOL 120CX electron microscope. Further details concerning specimen preparation and other experimental techniques are presented elsewhere.<sup>2,3</sup>

#### Experimental Results and Discussion

Typical results for a single implantation of  $5.5 \times 10^{14}$   $\text{D}_2^+/ \text{cm}^2$  are presented in Fig. 1, wherein a bright-field image, perpendicular to the implanted surface and near to a mask edge, and corresponding (inserted) electron diffraction pattern from the implanted zone are pictured. Depth penetration and lateral diffuseness are delineated, respectively, by the horizontal and inclined extremities of the dark (implanted) zone. This zone remains fully crystalline, as demonstrated by the inserted electron diffraction pattern. At present, however, exact position of the mask edge (somewhere above and extending to the right of the inclined region) can not be determined because the mask was removed prior to the cross-sectioning process. The LPE/GGG interface, extending about 1.1  $\mu\text{m}$  below the implanted surface, is also visible. Similar results for a single implantation of  $2.5 \times 10^{14}$   $\text{O}^+/ \text{cm}^2$  are presented in Fig. 2, wherein a bright-field image and corresponding (inserted) electron diffraction pattern from the implanted zone are pictured. Depth penetration and lateral diffuseness are delineated, respectively, by the horizontal and inclined extremities of the dark (implanted) zone. Again, this zone remains fully crystalline, as demonstrated by the inserted electron diffraction pattern, and the LPE/GGG interface, extending about 0.9  $\mu\text{m}$  below the implanted surface, is visible.

Typical results for an implantation of  $4.5 \times 10^{14}$   $\text{D}_2^+/ \text{cm}^2$  followed by  $3.0 \times 10^{14}$   $\text{O}^+/ \text{cm}^2$  are presented in Fig. 3, wherein a bright field image, perpendicular to the implanted surface and near to a mask edge, and



Fig. 1. Bright-field image, perpendicular to the implanted surface and near to a mask edge, and corresponding electron diffraction pattern from a zone implanted with  $5.5 \times 10^{14} \text{ D}_2^+/ \text{cm}^2$  at 88 keV. Depth penetration and lateral diffuseness are delineated, respectively, by the horizontal and inclined extremities of the dark (implanted) zone. The LPE/GGG interface, extending about 1.1  $\mu\text{m}$  below the implanted surface, is also visible.

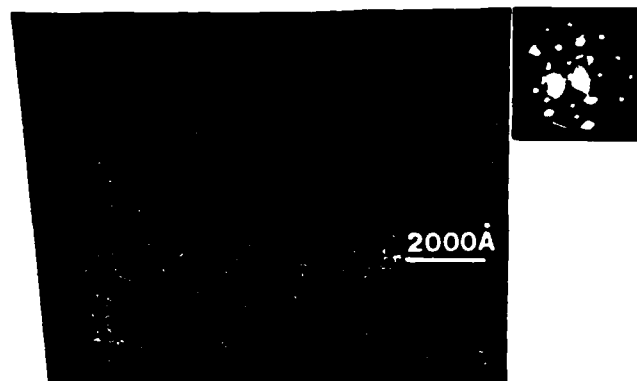


Fig. 2. Bright-field image, perpendicular to the implanted surface and near to a mask edge, and corresponding electron diffraction pattern from a zone implanted with  $2.5 \times 10^{14} \text{ D}^+ / \text{cm}^2$  at 100 keV. Depth penetration and lateral diffuseness are delineated, respectively, by the horizontal and inclined extremities of the dark (implanted) zone. The LPE/GGG interface, extending about 0.9  $\mu\text{m}$  below the implanted surface, is also visible.

corresponding (inserted) electron diffraction patterns from the  $\text{D}^+ + \text{D}_2^+$  and  $\text{D}_2^+$  implanted zones are pictured. Once again, depth penetration and lateral diffuseness are delineated, respectively, by the horizontal and inclined extremities of each implanted zone. Both zones remain fully crystalline, as demonstrated by the inserted electron diffraction patterns, and the LPE/GGG interface, extending about 1.4  $\mu\text{m}$  below the implanted surface, is visible. Extent of depth penetration  $d$  and lateral diffuseness  $w$  are quantitatively defined in Fig. 4 and results for all single and double implantations are presented in Figs. 5 and 6,



Fig. 3. Bright-field image, perpendicular to the implanted surface and near to a mask edge, delineating two zones created by implantation with  $4.5 \times 10^{14} \text{ D}_2^+/ \text{cm}^2$  at 88 keV followed by  $3.0 \times 10^{14} \text{ O}^+ / \text{cm}^2$  at 100 keV and corresponding (inserted) electron diffraction patterns for (a) the  $\text{D}_2^+ + \text{O}^+$  and (b)  $\text{D}_2^+$  implanted zones. Depth penetration and lateral diffuseness of both zones are delineated, respectively, by the horizontal and tapered extremities of the dark (implanted) zones. The LPE/666 interface, extending about 1.4  $\mu\text{m}$  below the implanted surface, is also visible.

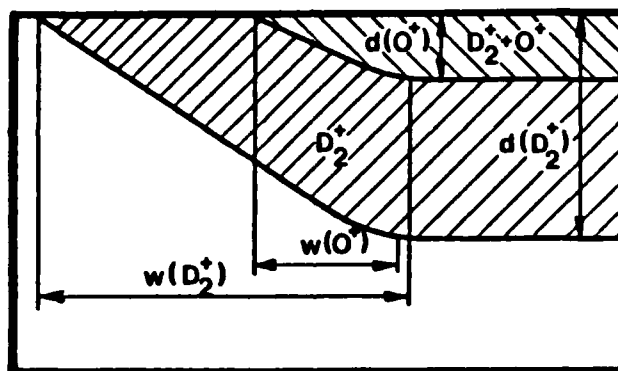


Fig. 4. Schematic illustration of implanted zones and definitions of penetration depth of  $\text{O}^+$ ,  $d(\text{O}^+)$ , and  $\text{D}_2^+$ ,  $d(\text{D}_2^+)$ , and lateral diffuseness of  $\text{O}^+$ ,  $w(\text{O}^+)$ , and  $\text{D}_2^+$ ,  $w(\text{D}_2^+)$ .

respectively. From Fig. 5 it may be ascertained that the penetration depth  $d$  and lateral diffuseness  $w$  increase linearly with dose of  $\text{D}_2^+$ , whereas these quantities first decrease and then increase slightly with dose of  $\text{O}^+$ . Likewise, from Fig. 6, it may be ascertained that  $d$  and  $w$  also decrease and then increase with increasing dose of  $\text{O}^+$  at 100 keV, when preceded by a constant dose of  $4.5 \times 10^{14} \text{ D}_2^+$  at 88 keV, although absolute values are increased somewhat by prior implantation (sensitization) with  $\text{D}_2^+$ . Moreover, corresponding values for  $\text{D}_2^+$  increase slightly with increasing dose of  $\text{O}^+$ . Similar trends are observed for other (constant) doses of  $\text{D}_2^+$  followed by (variable) doses of  $\text{O}^+$  and other (constant) values of implantation energy. Although minima in  $d(\text{O}^+)$  and  $w(\text{O}^+)$  are not

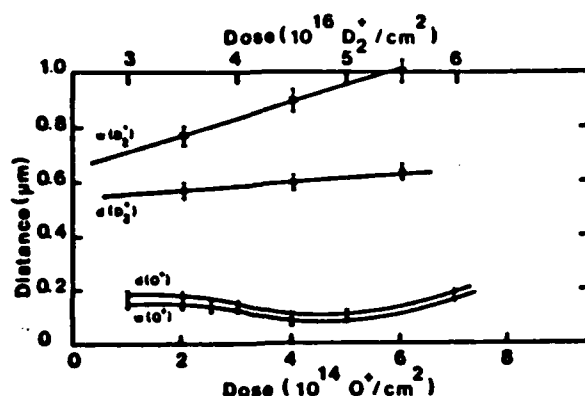


Fig. 5. Variation of penetration depth  $d$  and lateral diffuseness  $w$  as a function of implantation dose for single implantations with  $D_2^+$  at 88 keV or  $O^+$  at 100 keV.

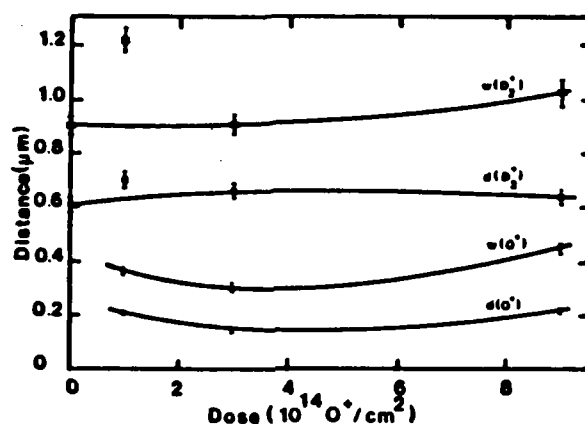


Fig. 6. Variation of penetration depth  $d$  and lateral diffuseness  $w$  as a function of implantation dose for double implantations at a constant dose of  $4.5 \times 10^{14}$   $D_2^+$  at 88 keV followed by a variable dose of  $O^+$  at 100 keV.

easily interpreted, it can be noted that the onset of amorphization occurs at about  $2.0 \times 10^{14}$ . This effect could account for a relaxation of strain and concomitant decrease in  $d(O^+)$  and  $w(O^+)$ .

In general, penetration depth is related to dimensions of magnetic bubbles and strength of charged walls, whereas lateral diffuseness limits spacing of bubble propagation patterns. The former quantity can be controlled with considerable precision by adjustment of implantation parameters, but the latter quantity depends on mask definition, diffuse scattering of ions below the implanted surface, and precise correspondence between distribution of implanted ions and resultant distribution of strain.

In the present research, a pattern of photoresist has been produced with the aid of a mask fabricated by usual photographic processes. A typical profile of this pattern is presented in Fig. 7, wherein a scanning electron micrograph is pictured. Generally, the





Fig. 7. Cross-section of mask used to define the implantation patterns.

inclined portion of the pattern extends over a lateral dimension ( $w$ ) of about  $0.7 \mu\text{m}$ . Therefore, a large fraction of the lateral diffuseness may be due to poor mask definition. Research is in progress to better define mask edges and, therefore, to separate effects of tapered mask edges, diffuse scattering of implanted ions, and correlation of resultant strain field with actual distribution of implanted ions.

Effect of mask definition on concomitant magnetic properties has recently been analyzed by a numerical method.<sup>4</sup> Typical results are presented in Fig. 8, wherein distribution of magnetization as a function of implantation depth  $d$  and lateral diffuseness  $w = d$  near the edge of a tapered mask is pictured. The general profile defined by demarcation between parallel and perpendicular magnetization closely resembles the profiles reported in Figs. 1-3 and supports the argument that lateral diffuseness  $d$  is due to a combination of poor mask delineation, diffuse

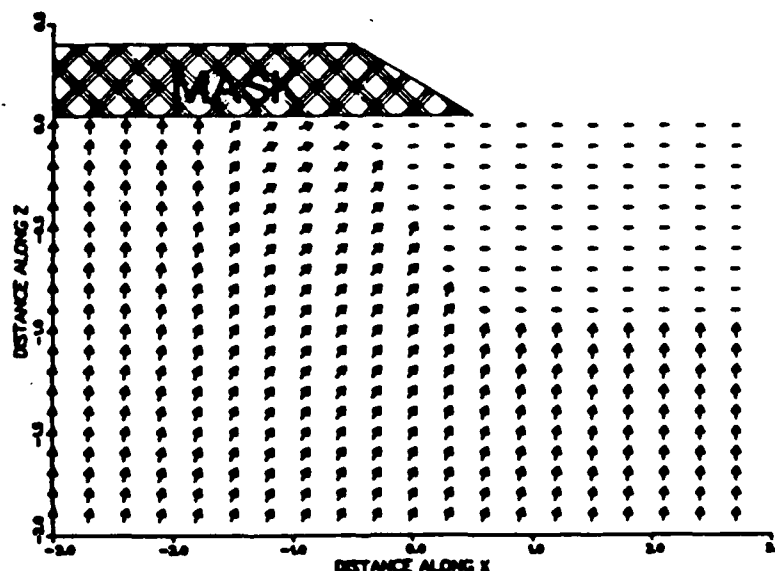


Fig. 8. Distribution of the magnetization at a tapered mask edge in a magnetostrictively isotropic film of garnet.

scattering of implanted ions, and uncertain correspondence between distribution of implanted ions and concomitant strain. This diffuse zone may induce an undesirable weakening of charged domain walls, which ultimately control trajectories of magnetic bubbles in ion-implanted memory devices.

Lastly, it should be emphasized that the origin of the contrast demarcation between implanted and unimplanted zones is unknown. It is suggested that this demarcation is due to the strain gradient between implanted and unimplanted regions, since  $d$  corresponds approximately to the computed penetration depth and varies as expected with implantation energy.<sup>5</sup> Nevertheless, because these lines of demarcation are much sharper than breadth of the expected strain gradient(s), values of  $d$  and  $w$  reported herein must be interpreted as a measure of depth penetration and lateral diffuseness rather than as a precise distance from the implanted surface to a specified value of either strain or concentration of implanted ions. Nevertheless, the fact that the reported profiles tend to vanish when specimen thickness is less than implantation depth ( $d$ ), verifies that these profiles are a result of the induced strain.

#### Summary

Thin films of  $(\text{SmYbTm})_{0.6}\text{Ga}_{0.4}\text{Fe}_{0.4}\text{O}_{1.2}$  have been produced by liquid phase epitaxy on (111) substrates of gadolinium-gallium garnet, non-uniformly masked, and implanted with ions of deuterium at 88 keV and doses ranging from  $3.5$  to  $5.5 \times 10^{14} \text{ D}_2^+/ \text{cm}^2$  and/or with ions of oxygen at 100 keV and doses ranging from  $0.95$  to  $8.6 \times 10^{14} \text{ O}^+ / \text{cm}^2$ . Subsequent examination by TEM, incorporating a special cross-section technique, reveals two-dimensional implantation profiles and allows both penetration depth  $d$  and lateral diffuseness  $w$  to be quantitatively measured for each implanted species. The quantity  $d$  is related to dimensions of magnetic bubbles and strength of charged walls, whereas  $w$  limits spacing of bubble propagation patterns. These parameters increase with increasing dose of  $\text{D}_2^+$  and decrease slightly (at onset of amorphization) and then recover to their original values with increasing dose of  $\text{O}^+$ . Moreover, resultant profiles are in qualitative agreement with predicted stress-induced magnetic anisotropy within the implanted zone. It is necessary to achieve a greater appreciation and eventual control of factors which affect these profiles in order to increase storage density and improve reliability of implanted magnetic bubble memory devices.

#### Acknowledgement

Useful discussions with D. A. Sanders, assistance with ion implantation from J. G. Tabacchi, and support from the Air Force Office of Scientific Research under

Contract B4-0341 are gratefully acknowledged.

8.

References

1. T. Yoshiie, C. L. Bauer and M. H. Kryder, J. Appl. Phys. 57, 2155 (1985).
2. J.-F. Silvain, C. L. Bauer, A. M. Guzman and M. H. Kryder, Proceedings of the Conference on *Implantation Effects in Solids*, 1985 Fall Meeting of AIME.
3. T. Omi, C. L. Bauer and M. H. Kryder, J. Appl. Phys. 53, 2528 (1982).
4. D. A. Sanders and M. H. Kryder, J. Appl. Phys. 57, 4061 (1985).
5. T. Gallagher, private communication.

END

1-87

DTIC